Advanced Photon Source Upgrade Project

Final Design Report

May, 2019

Chapter 2: Accelerator Upgrade

Document Number : APSU-2.01-RPT-003
ICMS Content ID : APSU_2032071

Table of Contents

List of Figures

Acronyms and Abbreviations

2D	two dimensional
3D	three dimensional
3PW	three-pole wiggler
7BA	seven-bend achromat
ABSM	absolute beam size monitor
AC	alternating current
ACIS	APS Access Control and Interlock System
ADC	analog-to-digital converter
AGC	automatic gain control
ALARA	as low as reasonably achievable
APD	avalanche photodiodes
APS	Advanced Photon Source
APS-U	Advanced Photon Source Upgrade
BM	bending magnet
BNL	Brookhaven National Laboratory
BPLD	beam position limit detector
BPM	beam position monitor
BSC	beam stay clear
BSM	beam size monitor
BTS	booster-to-storage ring
BTX	booster extraction test line
CAD	computer-aided design
CDB	component database
CDF	cumulative distribution function
CFD	computational fluid dynamics
CMM	coordinate measuring machine
CUFE	canted undulator front end
CW	continuous wave

DA	dynamic acceptance
DAQ	data acquisition
DC	direct current
DCCT	direct-current current transformer
DLM	doublet-L-bend-multiplet
DMM	Demonstration Modular Multiplet
DOF	degree of freedom
DS	downstream
DSC	double-sector controller
DSP	digital signal processor
EAA	Early Assembly Area
EDM	electrical discharge machining
EPICS	Experimental Physics and Industrial Control System
ERL	Energy Recovery Linac
ESRF	European Synchrotron Radiation Facility
FB	feedback
FBC	feedback controller
FDS	fast data stream
FEA	finite element analysis
FEM	finite element method
FID	fast ionization dynistor
FIR	finite impulse response
FLE	electron-positron fluence
FODO	focusing-drift-defocusing-drift
FOFB	fast orbit feedback
FPBC	feedback controller
FPGA	field programmable gate array
FSE	fractional-strength-error
FWHM	full width half maximum

G-line	Goubau-line
GDX	gigabyte data exchange
GRID	grazing-incidence insertion-device
H7BA	hybrid seven-bend achromat
HGSCU	horizontal-gap superconducting undulator
HHC	higher-harmonic cavity
HHC	high harmonic cavity
HHLFE	high heat load front end
HLRF	high level radio-frequency
HLS	hydrostatic leveling system
HMBA	hybrid multi-bend achromat
HOM	higher order mode
HSCU	helical superconducting undulator
HV	high voltage
I/O	input/output
IBS	intra-beam scattering
ID	insertion device
IOC	input-output controllers
LEA	linac extension area
LFB	longitudinal feedback
LLRF	low level radio-frequency
LMA	local momentum acceptance
LO	local oscillator
MBA	multi-bend achromat
MCI	maximum credible incident
MCR	Main Control Room
MLI	multi-layer insulation
MMS	Mechanical Motion System
MOGA	multi-objective genetic algorithm

MOSFET	metal-oxide semiconductor field-effect transistor
MPS	machine protection system
MRF	MicroResearch Finland
MTBF	mean time between failure
MWS	Micowave Studio
NEG	non-evaporable getter
NMR	nuclear magnetic resonance
NSLS-II	National Synchrotron Light Source II
ODH	oxygen deficiency hazard
PAR	Particle Accumulator Ring
PCG	photoinjector rf gun
PEP	Positron-Electron Project
PLC	programmable logic controller
PSD	power spectral density
PSD	photon-stimulated desorption
PSS	Personnel safety system
PTB	PAR-to-Booster
PV	process variable
QA	quality assurance
QR	quick response
RBSM	relative beam size monitor
rf	radio-frequency
RGA	residual gas analyzer
RM	response-matrix
rms	root mean square
RTFB	real-time fast orbit feedback
SCU	superconducting undulator
SD	defocusing sextupole
SF	focusing sextupole

SiC	silicon carbide
SLM	synchrotron light monitor
SoC	system on chip
SPI	serial peripheral interface
SR	storage ring
SRF	superconducting radio-frequency
ST	low carbon steel
SV	singular value
TBT	turn-by-turn
TCSPC	time-correlated single-photon counting
TDR	Time Domain Reflectometer
TIM	timing module
US	upstream
VLAN	virtual local area network
VP	Vanadium Permendur
XBPM	x-ray beam position monitor

2 Accelerator Upgrades

2-1 Introduction

The Advanced Photon Source (APS) storage ring will be upgraded by using a multibend achromat (MBA) lattice to provide dramatically enhanced hard x-ray brightness and coherent flux to beamline experiments in comparison to the present machine. To accomplish this, a hybrid multi-bend achromat magnetic lattice has been developed. It includes seven bending magnets in each of the 40 sectors, in comparison to the present two per sector, and in addition will use an additional 6 horizontally offset quadrupole magnets as weak reverse bends to further optimize brightness.

This new machine has a number of novel features, including nearly round beams in contrast to the present relatively wide beam. The present suite of insertion device beamlines (including canted lines) and bending magnet (BM) beamlines will be supported. Relatively high single-bunch current operation will be preserved, with 4.2 mA per bunch in a uniformly-spaced 48-bunch fill pattern. New particle- and x-ray beam position monitors and feedback systems will be used to provide ultra-stable operation commensurate with the significantly smaller transverse particle beam dimensions. To accommodate very strong linear and non-linear magnetic focussing elements, a new injection scheme which does not require large horizontal vacuum chamber apertures, has been developed.

2-1.1 Performance Goals

The proposed design parameters shown in Table 2.1 have been chosen to increase x-ray brightness by 2 to 3 orders of magnitude in comparison to the present APS machine, over a broad range of hard x-ray energies. The source size and divergence correspond to insertion device source points. The parameters shown are nominal, and do not include known physics such as intrabeam scattering, impedance, and harmonic cavity effects.

Table 2.1. Beam parameter comparison.

Quantity	**APS Now**	**APS MBA Timing Mode**	**APS MBA Brightness Mode**	**Units**
Beam Energy	7	6	6	GeV
Beam Current	100	200	200	mA
Number of Bunches	24	48	324	
Bunch Duration (rms)	34	104	88	ps
Energy Spread (rms)	0.095	0.156	0.135	%
Bunch Spacing	153	76.7	11.4	ns
Emittance Ratio	0.013	1	0.1	
Horizontal Emittance	3100	31.9	41.7	pm-rad
Horizontal Beam Size (rms)	275	12.9	14.7	μm
Horizontal Divergence (rms)	11	2.5	2.8	μrad
Vertical Emittance	40	31.7	4.2	pm-rad
Vertical Beam Size (rms)	10	8.7	3.2	μm
Vertical Divergence (rms)	3.5	3.6	1.3	μrad

Note that the emittance ratio is variable and can be adjusted to suit x-ray experimental requirements. In particular, a ratio of 0.1 shown in Table 2.1 for the 324-bunch brightness mode was selected to maximize overall brightness. In addition, round beams are also straight forward to produce.

2-1.2 Brightness Goals

Shown in Figure 2.1 is a comparison of the average beam brightness for the present APS storage ring to various possible insertion device sources installed on the APS-U storage ring. Over a wide range of hard x-ray energies extending up to and beyond 100 keV, an improvement by a factor of 100 to 1000 is seen.

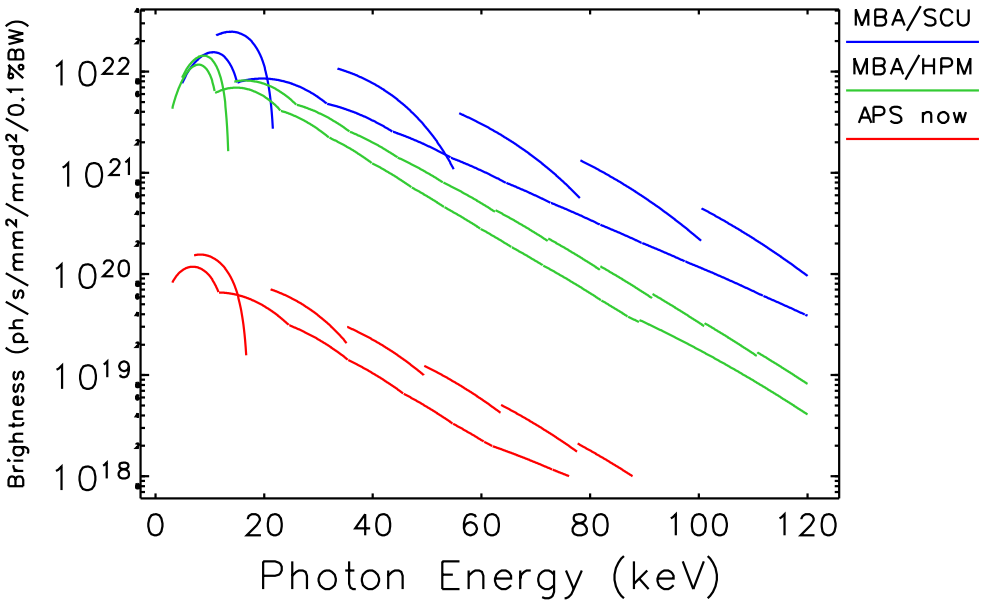

Figure 2.1. Brightness for APS today using several installed insertion devices compared to four possible undulators in APS-U. See Table 2.2 for list of device parameters.

Table 2.2. Undulator parameters for comparison of APS and APS-U

Type	Gap mm	Period mm	Length m
	APS		
HPM	10.75	33	4.8
HPM	10.75	27	4.8
	APS-U		
HPM	8.5	28	4.6
HPM	8.5	25	4.6
SCU	8.0	20.5	3.5
SCU	8.0	15.5	3.5

2-1.3 Choice of Beam Energy

An electron beam energy of 6 GeV vs. the present 7 GeV has been chosen to balance competing effects. Emittance scales quadratically with beam energy, yielding a 36% increase in brightness by lowering the energy. However, lower energy makes the beam more susceptible to wakefield-induced instabilities, intrabeam scattering effects, and Touschek lifetime reduction. Additionally, extremely high magnetic field gradients (>80 T/m) that scale linearly with energy argue for a lower energy to allow feasible magnet designs. Finally, the total energy loss per turn from the electron beam due to emission of synchrotron radiation scales as the fourth power of energy, allowing the possibility of storing a larger total beam current at 6 GeV vs. 7 GeV while relaxing the power and voltage requirements from the radio-frequency (rf) systems.

2-1.4 Choice of Beam Current

For the present design, considerable effort has gone into preserving high single-bunch charge, which is important for many x-ray timing experiments. This involves a tradeoff between the vacuum chamber design, which produces beam-disrupting wakefields, and the accelerator lattice configuration, which includes beam energy. Smaller vacuum chamber apertures are desireable from the standpoint of magnet design to reduce pole tipe fields, but doing this increases wake fields. The accelerator design presented here includes viable chamber and magnet designs commensurate with 6 GeV operation, with as few as 48 uniformly-spaced bunches, each containing 4.2 mA for a total of 200 mA. This is essentially the same bunch current presently used in the APS storage ring in 24-bunch operation at 100 mA.

2-1.5 Beam Stability

A number of challenges and opportunities arise in the consideration of beam stability for the APS-U storage ring. The most significant change is associated with more than an order of magnitude reduction in horizontal beam size, meaning that the horizontal beam stability requirement is reduced correspondingly. For the APS Upgrade, beam stability goals are based on 10% of the rms (root mean square) particle beam's phase space dimensions, implying sub-micron- and sub-microradian-scale stability levels on time scales extending from milliseconds to days. To achieve these goals, an integrated approach is being taken to first design a machine with extremely low levels of noise (e.g., power supplies, vibration suppression), and second to develop a world- leading fast orbit feedback (FOFB) architecture with closed-loop bandwidth exceeding 1 kHz. To meet the aggressive long-term drift requirements, x-ray diagnostics have been incorporated into beamline front ends, including a new high-power hard x-ray beam position monitor. In addition, hydrostatic level sensors will be used to measure and correct for long-term motions of the floor (e.g. earth tides).

2-1.6 Insertion Device Sources

The new storage ring will incorporate new and enhanced insertion devices to generate x-ray beams tailored to x-ray beamline requirements. Recent experience with superconducting undulators at the APS has made this technology very attractive for many applications. In addition to traditional planar hybrid permanent magnet devices, the use of revolvers will expand the flexibility of the source, allowing optimal beam properties at specific x-ray energies where needed. More exotic

devices which take advantage of round beams, such as vertically-polarized undulators requiring small horizontal apertures, will now be possible. To support x-ray experiments at existing bending magnet beamlines, bending magnet radiation from high-field transverse-gradient dipole bending magnets (B:M3) will be available.

2-1.7 Swap-Out Injection

In the late 1990s, the APS pioneered top-up operation, which provides nearly constant stored beam current to x-ray experiments [1]. This has become a standard operation mode for light sources worldwide. Accumulation with existing top-up operation requires that the injected and stored bunches co-propagate around the machine with relatively large but decreasing horizontal separation (many millimeters) over many milliseconds before coalescing.

Due to very strong non-linear focussing fields, the transverse dynamic acceptance of the APS-U storage ring is relatively small, making accumulation very challenging. Including in addition the presence of small horizontal apertures, conventional bunch accumulation will not be possible in the planned machine. Instead, the injected bunch will be injected directly onto the nominal stored-beam trajectory, completely replacing the stored bunch. This "swap-out" mode involves fast kicker magnets to extract and dump the stored bunch while bringing the injected bunch from the injector machines onto the stored-beam axis.

References

[1] L. Emery and M. Borland. "Top-up Operation Experience at the Advanced Photon Source." In: *Proc. of PAC 1999*. 1999, pp. 200–202. URL: http://cern.ch/AccelConf/p99/PAPERS/TUCL4.PDF (cit. on p. 4).

2-2 Beam Physics

This section summarizes the development and evaluation of the beam physics design, which is used as the basis for predicting the expected performance. The beam physics design and analysis has been iterated with the engineering designs for magnets, supports, and vacuum systems to provide assurance of feasibility. State-of-the-art simulation techniques have been used to provide highly detailed, statistical statements about expected performance in terms of emittance, injection efficiency, beam lifetime, and other properties. The development of the design and simulation methods are described in detail in the Preliminary Design Report [1]. Physics analysis for the final design lattice is described in a series of presentations [2, 3, 4, 5, 6, 7, 8] given at the October 2018 DOE/SC CD-2 Review of the Advanced Photon Source Upgrade Project, which will be referenced as appropriate in the summary below.

2-2.1 Lattice Design

After extensive comparison with other options [9], the "hybrid" multi-bend achromat (HMBA) concept proposed by ESRF [10] was adopted. In addition, reverse-direction bending magnets [11, 12] were added, allowing reduction of the natural emittance to 42 pm [13] compared to 67 pm in the design without reverse bends [14]. The lattice functions of the 42 pm reverse-bend lattice are shown in Fig. 2.2. In this concept, the dispersion is deliberately made large between the first and second, as well as between the sixth and seventh, dipoles, and all chromatic sextupoles are clustered in this dispersion bump region. As a result, the sextupoles can be longer (as there is more space) and are naturally weaker due to the larger magnitude of the dispersion. The magnitude of the dispersion is increased using a five-step longitudinal gradient in these dipoles, which also helps to minimize emittance increase. The additional "knobs" provided by the dipole field in the reverse bending magnets help manipulate the dispersion independently of the beta functions, giving larger dispersion and better beta functions at the insertion devices. The betatron phase advance between the two dispersion bumps in each sector is set so as to cancel the leading non-chromatic effects of the sextupoles. Specifically, the phase advance in the horizontal plane is $\Delta\phi_x = 3\pi$, while in the vertical plane it is $\Delta\phi_y = \pi$. All of these factors have been found to be beneficial for the optimization of dynamic acceptance and beam lifetime in an APS-size ring, leading to a workable design with feasible sextupole strengths.

The present APS ring is operated at an energy of 7 GeV. A detailed examination [15] of the brightness performance of a H7BA lattice as a function of beam energy was undertaken, including the effects of intrabeam scattering and realistic insertion device performance. The result was that 6 GeV was chosen as the operating energy for the new ring.

2-2.1.1 Constraints on the Lattice

The new lattice is constrained in a number of ways by the parameters of the existing facility. Due to the effort involved in realigning beamlines, the ID straight sections must not move. Unfortu-

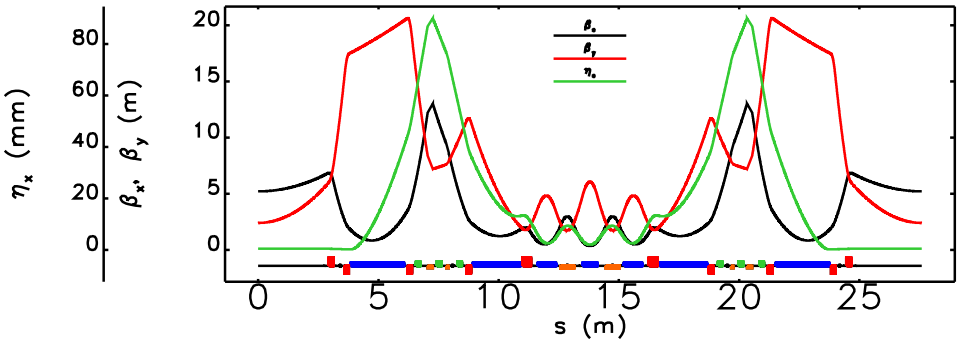

Figure 2.2. Hybrid 7BA lattice with reverse bends for the APS. The natural emittance is 42 pm. Blue blocks represent normal-direction dipoles, orange blocks represent reverse-direction dipoles, red blocks represent quadrupoles, and green blocks represent sextupoles.

nately, this constraint implies transverse offsets of the bending magnet beamlines and a reduction in circumference.

The BM source points are, as now, at an angle of $9\pi/320$ from the upstream ID source point. However, compared to the present situation, the BM source points move upstream by 2.908 m with a transverse inboard offset of 39 mm. Because of the lower beam energy and design constraints on the transverse-gradient dipole magnets, it was not possible to maintain the present critical energy of 19.5 keV. One possible solution for users requiring harder x-rays is to provide space for short wiggler magnets that may deliver photons to BM beamlines. Space was provided for 15-cm-long devices, should they be required. The impact of such devices is described in [16].

The circumference changes to 1103.61 m, compared to an original design circumference for the present ring of 1104 m and a present-day circumference of 1103.986 m (derived from the median rf frequency over one year). Hence, compared to present-day operations, the rf frequency increases by 341 ppm. Hence, the booster will have a separate rf source and the injector timing system will be modified to deliver booster bunches to the desired storage ring bucket in spite of this (see Section 2-3.14.1.3).

2-2.1.2 Optimization of Nonlinear Dynamics

Nonlinear dynamics optimization was performed by using a tracking-based approach [17] that provides direct optimization of dynamic acceptance (DA) and Touschek lifetime (via local momentum acceptance). using a multi-objective genetic algorithm (MOGA) similar to those described in [18, 19]. In this instance, the MOGA algorithm varied two types of quantities, namely, focusing gradients and sextupole strengths. In addition to DA area and Touschek lifetime, the objective functions for MOGA included the smoothness of the DA contour, the extent of the momentum variation of the tunes, and the x-ray brightness at 20 keV [2]. Linear chromaticities were allowed to vary between 4 and 9, with the low end of the range chosen to ensure stability of high-charge bunches in 48-bunch, 200-mA mode.

In the APS-U design, thanks to the use of sophisticated tracking-based optimization and many in-

dependent families of chromatic sextupoles, neither geometric sextupoles nor octupoles are required. The eight-pole correction magnets, of which there are four in each sector, have the potential to be powered as octupoles.

2-2.1.3 Summary of Lattice and Magnet Properties

The lattice functions are shown in Fig. 2.2. Properties of the lattice are listed in Table 2.3.

Magnet data is listed in Tables 2.4 through 2.6. The reverse-bending magnets Q4 and Q5 have relatively weak dipole fields, which might seem ineffective. However, these fields are very effective in adjusting the damping partition, since the dispersion is high at those locations. Further, they allow raising the maximum dispersion without harming the emittance by providing a means of bringing the dispersion back down in the M2 magnets. Without reverse bending in this area, the minimum achievable emittance is 58 pm [20].

As mentioned above and exhibited in Table 2.4, the M1 and M2 longitudinal gradient dipoles were optimized as five nominally independent segments. The tendency is for the first segment of M1, labeled M1.1 in the table, to become very short and strong, which helps to increase the horizontal dispersion function in the sextupoles and also reduce the emittance. This was restrained by requiring a length of at least 10 cm for the M1.1 segment and limiting the ratio of maximum-to-minimum field strength within the M1 to 5:1. Similar constraints were placed on the M2. The M3, Q8, M4 magnets require a combination of a moderately high dipole field with a signficant transverse gradient, which is a challenging combination. The difficulty of obtaining a high dipole field in these magnets motivated the inclusion of an optional three-pole wiggler as a possible source for bending magnet beamlines.

As seen in Table 2.5, there are three quadrupole magnet lengths. The Q7 magnets require significantly greater length than the others in order to reduce the magnitude of the magnetic field gradients.

Table 2.6 shows the parameters and nominal strengths of the sextupole magnets. The solutions were developed with several alternate methods [21] in addition to the one described above (which was judged to give the best overall result). The S2 magnets, which correct the horizontal chromaticity, are significantly stronger largely by virtue of being fewer in number. There is also some variation in the strengths of nominally equivalent sextupoles, which is important for obtaining good Touschek lifetime.

2-2.2 Tolerances and Correction Schemes

Analysis of susceptibility to various errors is an important part of any storage ring design. There are two main types of errors that can affect a storage ring: (1) magnet strength errors, from construction or power supply errors, and (2) magnet alignment errors. These errors can be static, or they can change in time. Power supply and magnet errors can be random, and they can also have a systematic component.

The effect of static random errors in most cases can be measured using beam-based techniques and can be subsequently corrected. Two types of static errors may be distinguished: initial errors and

Table 2.3. Lattice parameters

Tunes and Chromaticities		
ν_x	95.100	
ν_y	36.100	
ν_x/N_s	2.3775	per sector
ν_y/N_s	0.9025	per sector
ξ_x	8.02	
ξ_y	5.48	
Natural ξ_x	-133.50	
Natural ξ_y	-111.50	
Lattice functions		
Maximum β_x	13.01	m
Maximum β_y	20.59	m
Maximum η_x	0.090	m
Average β_x	3.76	m
Average β_y	8.42	m
Average η_x	0.031	m
Radiation-integral-related quantities at 6 GeV		
Natural emittance	41.68	pm
Energy spread	0.135	%
Horizontal damping time	6.85	ms
Vertical damping time	15.40	ms
Longitudinal damping time	20.51	ms
Energy loss per turn	2.87	MeV
ID Straight Sections		
β_x	5.19	m
β_y	2.40	m
η_x	0.39	mm
$\epsilon_{x,eff}$	41.7	pm
Miscellaneous parameters		
Momentum compaction	4.04×10^{-5}	
Circumference	1103.6083	
$\Delta f_{rf}/f_{rf}$	3.42×10^{-4}	
Damping partition J_x	2.25	
Damping partition J_y	1.00	
Damping partition J_δ	0.75	

reproducibility errors. Values for initial errors are chosen so as to provide for reasonably quick commissioning, while reproducibility goals should ensure that the storage ring can be operated without major corrections after being turned off and then back on. Tolerances for individual magnets and other systems are determined from these goals. Several types of static systematic error were examined, including errors in quadrupole magnetic lengths and relative strength errors between all dipoles and all quadrupoles, resulting in requirements for construction and measurement [22].

2-2.2.1 Variable Errors

The most important storage ring parameters that are susceptible to varying errors are beam orbit and betatron tune stability. Table 2.7 gives requirements on allowable limits of orbit and tune variation.

Table 2.4. Bending magnet parameters. Reverse-direction bending magnets have names beginning with "Q," since these originated as quadrupoles in the previous lattice.

Name	Effective Length m	Insertion Length m	Angle deg	B_0 T	B' T/m	E_c keV	$P_{\mathrm{d,integ}}$ W/mrad	P_d $W/mrad^2$	Count
M1 (x80)									
M1.1	0.192	0.192	0.357	-0.650	-0.000	15.6	118.5	913.4	80
M1.2	0.233	0.233	0.267	-0.400	-0.000	9.6	72.9	561.6	80
M1.3	0.493	0.493	0.381	-0.270	-0.000	6.5	49.2	379.4	80
M1.4	0.671	0.671	0.375	-0.195	-0.000	4.7	35.6	274.2	80
M1.5	0.636	0.636	0.257	-0.141	-0.000	3.4	25.8	198.5	80
M2 (x80)									
M2.1	0.292	0.292	0.135	-0.161	-0.000	3.9	29.4	226.6	80
M2.2	0.359	0.359	0.187	-0.182	-0.000	4.4	33.2	255.6	80
M2.3	0.487	0.487	0.297	-0.213	-0.000	5.1	38.8	299.0	80
M2.4	0.308	0.308	0.222	-0.252	-0.000	6.0	45.9	353.6	80
M2.5	0.540	0.540	0.495	-0.320	-0.000	7.7	58.4	450.1	80
M3 (x80)									
M3	0.768	0.794	1.437	-0.653	41.506	15.6	119.1	917.8	80
M4 (x40)									
M4	0.645	0.672	1.125	-0.609	48.290	14.6	111.1	856.3	40
Q4 (x80)									
Q4	0.211	0.260	-0.098	0.162	-80.135	3.9	29.5	227.5	80
Q5 (x80)									
Q5	0.104	0.150	-0.066	0.223	-43.181	5.3	40.6	313.0	80
Q8 (x80)									
Q8	0.576	0.646	-0.307	0.186	-80.058	4.5	33.9	261.6	80

0.01 Hz – 1 kHz Frequency Range

Since most user experiments average over more than one turn of the electron beam (and many experiments require averaging for many turns), the electron beam motion during the averaging time transforms directly into an effective increase of the source size. Orbit stability is mainly affected by electrical noise of the magnet power supplies and by vibration of the magnets. To calculate the tolerances for time-varying errors, one needs a good knowledge of the spectral characteristics of all the processes involved. The overall motion is split into three components: electrical noise in magnets, magnet vibration, and BPM vibration. While BPM vibration does not, of course, affect the beam location directly, it will affect the beam location by causing the orbit correction system to move the beam. Every component of the noise goes through a series of transformations before reaching the user sample. For example, a change in bending angle due to electrical noise in a corrector is first attenuated by the vacuum chamber, then it is amplified by the lattice, and then it is attenuated by the orbit correction, which results in the final orbit motion. The orbit motion is then projected onto the user sample with some transfer function. Specific assumptions about various effects are given in [23].

Some of the assumptions are illustrated in schematic form in Fig. 2.3, where the shape of the noise

Table 2.5. Quadrupole data

Element Name	Effective Length m	Insertion Length m	K_1 $1/m^2$	B' T/m	B'L T	Count
FS1	0.158	0.158	0.0	-0.0	-0.0	80
FS2	0.158	0.158	0.0	-0.0	-0.0	80
Q1	0.205	0.250	3.9	-79.0	-16.2	80
Q2	0.179	0.225	-3.4	67.5	12.1	80
Q3	0.180	0.225	-3.0	59.4	10.7	80
Q6	0.180	0.225	-3.0	59.0	10.6	80
Q7	0.357	0.424	4.3	-86.0	-30.7	80

Table 2.6. Sextupole data

Element Name	Insertion Length m	K_2 $1/m^3$	B'' T/m^2	B''L T/m	Count
S01A:S1	0.230	-158.3	3167.7	727.1	20
S01A:S2	0.260	253.0	-5062.6	-1315.2	20
S01A:S3	0.230	-151.4	3029.5	695.4	20
S01B:S1	0.230	-125.7	2516.2	577.6	20
S01B:S2	0.260	233.7	-4677.9	-1215.3	20
S01B:S3	0.230	-143.5	2871.2	659.1	20
S02A:S1	0.230	-150.1	3005.0	689.8	20
S02A:S2	0.260	128.3	-2567.3	-667.0	20
S02A:S3	0.230	-136.1	2723.9	625.3	20
S02B:S1	0.230	-140.9	2819.1	647.1	20
S02B:S2	0.260	142.9	-2859.8	-743.0	20
S02B:S3	0.230	-148.8	2977.5	683.5	20

spectrum is given as well as the shape of vacuum chamber attenuation, lattice amplification, and orbit correction attenuation. The lattice amplification of magnet vibration takes into account the effect of the ground motion coherence at low frequencies [24, 25]. The resulting PSD of the beam orbit motion is the product of the four functions shown in the schematic.

Since some measurements, such as orbit response measurements, must be performed without orbit correction running, uncorrected orbit motion due to vibrational and electrical noise needs to be below some limit. From present experience, a limit of 1 μm seems to be reasonable. The same approach for calculating orbit motion illustrated in Fig. 2.3 can be used to find the orbit motion during response matrix measurement, only instead of attenuation due to orbit correction, one should use the attenuation due to subtraction of two orbits or due to AC filtering depending on the way the response matrix measurement is carried out [26]. The apportioning of the budget motion for both cases (with and without orbit correction) is given in PDR [1].

The effect of insertion devices on the orbit is expected to be very small because these perturbations are very small. Based on the expected performance of the APS-U orbit correction, the effect of insertion device on the orbit is expected to be 200 times smaller than for the present APS [1].

Table 2.7. Requirements on varying errors

Band	Limit (rms)	Magnets responsible
	Orbit stability	
0.01 Hz – 1 kHz	0.1 σ	Dipole noise Corrector noise Quadrupole vibrations
<0.01 Hz	1 μm	Dipole drift Corrector drift Quadrupole position drift
	Tune stability	
0.01 Hz – 1 kHz	10^{-3}	Dipole noise (through energy) Quadrupole noise Corrector noise Sextupole noise and vibration (through orbit) Orbit noise (through sextupoles)
<0.01 Hz	10^{-3}	Dipole drift Quadrupole drift Corrector drift Sextupole drift (strength and position) Orbit drift

As with static errors, the main sources of tune variation are quadrupole and dipole power supply noise and orbit noise in sextupoles. It is assumed that no tune correction is running in this bandwidth. However, the attenuation effect due to the solid core magnets and vacuum chamber discussed above is still present and is taken into account. Other possible sources of tune variation are sextupole power supply noise and orbit motion in sextupoles [1].

Summary of Tolerances, 0.01 Hz – 1 kHz

Requirements for electrical noise and magnet vibration were considered through their effects on orbit stability (with and without orbit correction) and on betatron tune variation. A summary of the requirements, derived from the above considerations [23], is given in Tables 2.8 and 2.9.

It is important to note that most of the vibration requirements are dictated by the stability requirements of the non-user operation (beam studies), mainly to have quiet orbit during response matrix measurements. If only user operation with orbit correction running is considered in the requirement calculations, some numbers in Table 2.9 could be considerably relaxed. Understanding this, work is ongoing concerning how to relax the requirements, e.g., using AC lock-in response matrix measurements or an equivalent measurement with orbit correction running.

Drift tolerances (variations below 0.01 Hz)

There are several effects that contribute to slow variations of orbit and other parameters in a storage

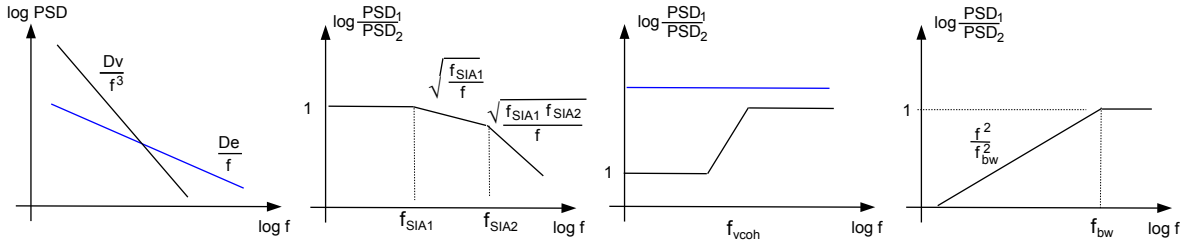

Figure 2.3. From left to right: Power spectral density of electrical (blue) and vibrational noise (black) with power amplitudes D_e and D_v; electrical noise attenuation due to solid iron core and vacuum chamber with bandwidths f_{SIA1} and f_{SIA2}; lattice amplification factors: blue – for electric noise, black – for vibrational noise; beam motion attenuation due to orbit correction with bandwidth f_{bw}.

Table 2.8. Summary of rms electrical noise tolerances for 0.01-1000 Hz bandwidth.

Magnet type	Requirement	Based on
Correctors	$2 \cdot 10^{-4}$	Orbit stability
Dipoles M3-M4	$2 \cdot 10^{-5}$	Orbit stability
Dipoles M1-M2	$2.3 \cdot 10^{-5}$	Tune stability
Quadrupoles	$2.5 \cdot 10^{-5}$	Tune stability
Sextupoles	$2 \cdot 10^{-3}$	Tune stability

ring: power supply drifts lead to slow lattice parameter variation; mechanical motion of BPMs leads to orbit motion and could thus lead to lattice changes as well; changes in ID gaps also result in focusing changes.

Power supply drifts are assumed to be dominated by environmental temperature variation. In this case, all power supplies change simultaneously in one direction, and the overall behavior is oscillatory [27]. The BPM drifts will be dominated by the thermal longitudinal expansion of the vacuum chamber that will lead to some unpredictable transverse deformation and thus BPM motion. Orbit correction will make the beam follow the BPMs and thus change the real orbit, as described in [28]. One more source of drift is the change of ID gaps. A single 4.8-m long U27 ID closed to the minimum gap changes vertical tune by 0.001 and causes rms beta function beating of 0.6%. The effect of many undulators on the tune is additive, which, if left uncorrected, could lead to tunes shifts exceeding 0.01. As described in [29], global tune correction is needed, but beta function correction is not (see Section 2-2.3). Table 2.10 summarizes the requirements based on the drift simulations.

The effects of the AC line ripple, high-frequency ripple from switching power supplies, and glitches of individual power supplies were also considered in a similar fashion [1, 27]. The final requirements for power supply drifts, ripple, and glitches are summarized in Table 2.11.

Table 2.9. Summary of vibrational tolerances. Two bandwidths are given. The numbers in this table are the most demanding requirements based on either stability requirement with or without orbit correction.

	X (rms)	Y (rms)	X (rms)	Y (rms)
	1-100 Hz		0.1-1000 Hz	
Girder vibration	20 nm	20 nm	200 nm	200 nm
Quadrupole vibration	10 nm	10 nm	100 nm	100 nm
Dipole roll vibration	—	0.2 μrad	—	2 μrad

Table 2.10. Summary of drift simulations and corresponding rms requirements

	Tune effect	Beta function effect	Requirement
BPM drift	$1 \cdot 10^{-3}$	0.3%	± 5 μm
PS drift	$1.5 \cdot 10^{-3}$	—	$\pm 1 \cdot 10^{-5}$
ID gaps	$2 \cdot 10^{-3}$	0.5%	Tune feedforward

2-2.2.2 Simulation of Orbit and Lattice Correction

The very small emittance in the MBA lattice is achieved by much stronger focusing than in the present APS ring. Misalignments of the strong quadrupoles generate large orbit errors, which, in the presence of very strong sextupoles, leads to large lattice and coupling errors. Lattice distortions reduce the already small dynamic aperture and lifetime. Add to this smaller vacuum chamber gaps that are required to achieve high gradients in the magnets, and rapid commissioning becomes a significant challenge.

To address this challenge, a start-to-end simulation of machine commissioning was performed [30]. The simulated commissioning procedure closely follows the steps that will be performed during commissioning, using the errors given in Table 2.12. The procedure includes the following major steps:

- Correct trajectory until a multi-turn beam transmission is achieved;
- Correct "quasi-closed" orbit (orbit derived from multi-turn trajectory by averaging multiple turns on each BPM):
  - Adjust tunes after each iteration to keep them away from integer resonances
  - Ramp sextupoles after every few iterations
  - If orbit correction is diverging, perform very "gentle" optics correction with a very small number of SVs and a very small correction fraction.

Table 2.11. Summary of drift and ripple requirements coming from tune stability requirement of 0.001 peak to peak.

24-hour drift peak-to-peak	10^{-5}
AC line ripple peak-to-peak	$2 \cdot 10^{-5}$
High-frequency switching ripple peak-to-peak	$3 \cdot 10^{-3}$
Single glitch	10^{-3}

- Correct initial BPM offset errors;
- Correct orbit with new BPM offsets;
- Perform lattice correction, iterating between beta function correction and coupling minimization, while correcting the orbit between iterations (using one-step simple orbit correction).
- Adjust emittance ratio to a predetermined operational value by exciting the nearest difference resonance using skew quadrupoles.

Table 2.12. Various rms errors used for start-to-end commissioning simulation

Girder misalignment	100 μm
Elements within girder	30 μm
Initial BPM offset errors	500 μm
Dipole fractional strength error	$1 \cdot 10^{-3}$
Quadrupole fractional strength error	$1 \cdot 10^{-3}$
Dipole tilt	$4 \cdot 10^{-4}$ rad
Quadrupole tilt	$4 \cdot 10^{-4}$ rad
Sextupole tilt	$4 \cdot 10^{-4}$ rad

The entire, automated simulation procedure is run for 200 different error sets. The procedure successfully corrects orbit and optics in 95% of cases, with the remaining 5% requiring human intervention. The correction results are statistically analyzed for many parameters, such as orbit and lattice perturbations, corrector strengths, emittances, etc. For example, Fig. 2.4 shows that, assuming separated tunes, the low horizontal emittance of ∼42 pm is in fact achievable and that a 1% emittance ratio is achievable. If a $\epsilon_y \approx \epsilon_x$ is required, the tunes can be moved to the coupling resonance after lattice correction is complete.

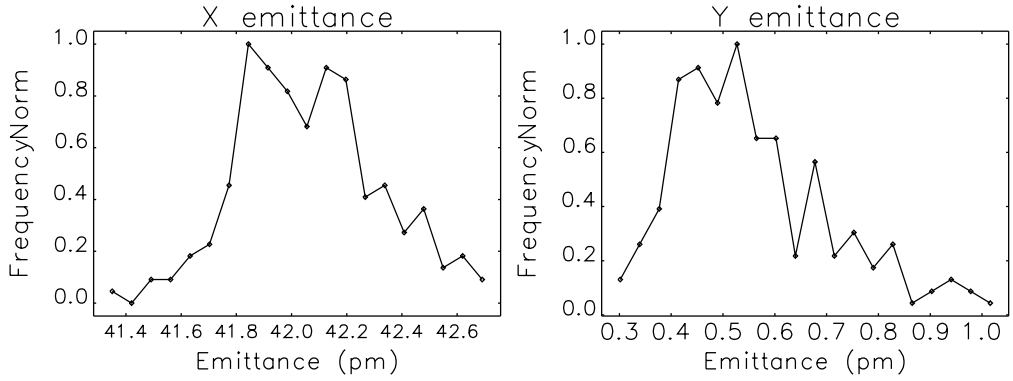

Figure 2.4. Distribution of horizontal (left) and vertical (right) emittance after lattice correction but before adjusting coupling.

2-2.2.3 Simulation of Beam Size Stability

Operation with $\kappa = \epsilon_y/\epsilon_x \approx 1$ is desirable in order to maximize the beam lifetime and reduce the impact of intrabeam scattering. However, the stability of the beam size and divergence when the tunes are moved together is a concern, as it might require a very high level of tune stability. The effect of the tune variation on the beam size has been simulated using the ensembles from the commissioning simulation [1]. It was found that the beam size variations are acceptable even for

the rms tune variation $\sigma_{\Delta\nu} = 5 \times 10^{-3}$ (tune stability specification is 10^{-3}).

2-2.3 Lattice Evaluation

Following lattice optimization, solutions on the Pareto-optimal front are examined in detail to choose those that best balance the desire for large DA, smooth DA, long Touschek lifetime, and a desirable momentum-dependent tune footprint. One or more solutions are then typically subjected to evaluation with a significant number (typically 100) of error ensembles generated by an automated commissioning algorithm [31, 4]. Such analysis provides statistical predictions of the likely performance in terms of emittance, coupling, injection efficiency, Touschek lifetime, and gas scattering lifetime.

In addition to including the results of errors and commissioning, lattice evaluation includes multipole errors in the accelerator magnets and insertion devices (IDs). These have been used to specify requirements on field quality and to understand tuning strategies. One important result is that it is not necessary to correct beta function distortions that result from changing ID gaps: correcting the tunes with global knobs is sufficient.

Details of the evaluation methods are described in the PDR [1], CD2 presentations [5, 7] and elsewhere, as noted below.

- Lattice properties are computed using 6D beam moments including quantum excitation and radiation damping [32, 33]. This provides predictions of the projected emittances and beam sizes at radiation source points.
- Injection efficiency is modeled including errors in the booster and transport line, jitter in pulsed elements, coupling in the transport line, rf system jitter, and other effects [34]. Using uniform particle distributions with gaussian weights, small losses can be modeled without excessive computing effort, providing not only distributions of the fraction lost, but also spatial distributions of the loss intensity. The latter are used in shielding analysis.
- Touschek lifetime is computed by two different methods
  - Tracking with collective effects is used to obtain turn-by-turn samples of the longitudinal distribution as a function of detuning of the higher harmonic cavity (HHC). This is used for slice-based computation of the effects of intrabeam scattering [35, 36] and then for slice-based computation of the Touschek scattering rate [36] using Piwinski's method [37].
  - Direct simulation of Touschek scattering [38, 39] is performed for a small number of cases as a cross check; the number of cases is limited by the compute-intensive nature of the simulations. The results typically agree within a few percent with the previous method, as described in Section 2-2.9.1 and have the benefit of providing spatial loss distributions for use in shielding analysis.
- Gas scattering lifetime is computed using a tracking-based approach [40, 41] that provides the loss rates for elastic and inelastic nuclear scattering, as well as the spatial loss distributions for shielding analysis. The computations make use of species-specific pressure profiles from the vacuum system model.

Table 2.13 shows the predicted summary beam parameters and related quantities. The lifetime results include Touschek scattering as well as gas scattering assuming a dose of 1000 A-h, which

will be achieved after approximately one year of operation at 200 mA. For the default "round-beam" modes ($\kappa = \epsilon_y/\epsilon_x \approx 1$), the 10^{th}-percentile lifetime is 3.7 h or more, while the injection interval is 16 s or more. This provides a large margin compared to the injector cycle time of 1 s. Slight differences are seen in the emittance and energy spread between 48- and 324-bunch modes, a result, respectively, of intrabeam scattering and a moderate microwave instability. A "flat-beam," 324-bunch mode is also shown; the lifetime is shorter in this case, but still easily within the capability of the APS injector.

Simulations also demonstrate that very low injection losses are expected, as shown in Table 2.14. The 90^{th} percentile loss fraction for the nominal booster emittance (ϵ_x = 60nm, ϵ_y = 16nm) is about 1%. Even significantly inflating the booster emittance is still consistent with relatively low injection losses.

Table 2.13. High-level beam and performance parameters, including IBS, impedance, and optimized harmonic cavity. 10^{th}- and 50^{th}-percentile lifetimes include Touschek and gas scattering.

N_b	Charge nC	κ	ϵ_x pm	ϵ_y pm	σ_δ %	$\tau_{10^{th}}$ h	ΔT_{inj} s	$\tau_{50^{th}}$ h	ΔT_{inj} s
48	15.34	0.99	31.9	31.6	0.145	3.7	28.0	4.0	30.3
324	2.27	0.99	29.8	29.5	0.136	15.0	16.7	16.1	17.9
324	2.27	0.13	41.7	5.6	0.138	7.3	8.1	9.1	10.1

Table 2.14. Loss fraction results from injection simulations, assuming 100-ps rms bunch duration, 0.12% rms energy spread, and various emittances from the booster. The nominal emittances are 60 nm by 16 nm.

Booster emittances	10th perc.	Median	90th perc.
60nm x 16nm	0.003	0.005	0.009
75nm x 20nm	0.008	0.013	0.020
90nm x 24nm	0.016	0.024	0.036

The predictions summarized here assume that components, such as magnets, satisfy the specifications. As fabrication and assembly proceed, these modeling techniques will be used to ensure that any deviation of components from specifications do not produce unacceptable degradation of performance.

2-2.4 Impedance and Single-Bunch Stability

In the swap-out method of injection planned for the APS Upgrade, the full bunch charge must be stably injected into an empty bucket. The number of electrons lost depends on a number of factors, including the size of the dynamic aperture relative to the emittance of the injected bunch, treated in Section 2-2.3, errors in the injection system as discussed in Section 2-2.8, and collective effects whose influence increases with the stored bunch current. Collective effects may include electron cloud, ions, and impedance elements in the ring. Experience suggests that electron cloud effects do not cause serious problems in electron storage rings. Ion effects will be addressed in Section 2-2.6.

This section discusses collective effects due to impedances/wakefields, which often limit the single-bunch current. In particular, instabilities driven by transverse wakefields typically limit the single-bunch current in storage rings like the APS, while longitudinal wakefields predominantly lead to bunch lengthening (which usually eases operational requirements) and a typically tolerable increase in energy spread. Longitudinal and transverse impedances will continue to be the dominant drivers of collective effects for the APS Upgrade, so that understanding and calculating the impedance is critical for accurate simulations—and thus accurate predictions—of the ring performance. Based on such simulations, the impedance cost of various vacuum component designs can be assessed, and limits will be imposed on sources of impedance to ensure that the desired parameters, including the single-bunch current, are achieved.

The successful method of computing and using impedances developed and tested for the APS ring [42, 43, 44, 45] was applied to APS-U. The next subsection describes the APS-U impedance model and subsequent predictions of longitudinal bunch lengthening and the onset of the microwave instability. A discussion of transverse stability follows, where simulations predict an impedance margin of approximately two for the 15.3 nC bunches needed in 48-bunch mode.

Next, a more detailed discussion of the longitudinal impedance and rf-heating associated with important wakefield sources, including the BPM-bellows assembly, the injection and extraction kicker, and the in-line photon absorbers, is presented. To complement and cross-check the simulation efforts described above, the planned rf measurement technique is briefly introduced in Section **??**. Finally, this section concludes with an overview of the findings and on-going efforts.

2-2.4.1 Impedance Model

The APS-U impedance model was developed by relying on the experience obtained while developing the impedance model for the present APS, and by carefully studying the methods used elsewhere. Table 2.15 summarizes the various components that contribute to the APS-U impedance model. The resistive wall contribution, which is the largest source of transverse impedance, is calculated by applying analytic formulas appropriate for the round and elliptical chambers listed in Table 2.15. In contrast, the geometric impedance depends on the detailed cross-sectional variation of various components along the vacuum vessel, so that computing it requires numerical simulation tools.

The geometric contribution is built from the individual impedances/wakefields of the components listed in Table 2.15. Each contribution is computed from the Fourier transform of the wakefield for one component. The wakefields in turn are computed using the 3D finite-difference time-domain code `GdfidL` [46], whose behavior is checked when possible against analytic results and calculations from the 2D `ECHO` code [47]. To balance efficiency and accuracy, GdfidL models the (point particle) wakefield with the wake potential generated by a gaussian bunch with a 1-mm rms length, an approximation used successfully for the current APS. Using this "pseudo-Green function" is equivalent to filtering the point-charge impedance by a Gaussian filter whose frequency width is ~ 50 GHz. As a point of reference, the zero-current frequency spectrum of the electron bunch including the higher-harmonic cavity (HHC) is ~ 3.2 GHz. Numerical tests with similar MBA lattices were performed using wake potentials derived from shorter electron bunches, giving the same results in terms of the microwave instability threshold and the single-bunch current limit [48].

The contributions to $\Im(Z_\parallel)/n$ and the loss factor are summarized in Table 2.16. $\Im(Z_\parallel)/n$ roughly

Table 2.15. Elements that contribute to the resistive wall and geometric impedances. Here, the full gap refers to the diameter for circular chambers and the major×minor axes for elliptical chambers, and BPM = beam position monitor.

Resistive wall			**Geometric contributions**			
Metal	**Full gap**	**Length**	**Sector (×40)**		**Ring**	
			Element	**Number**	**Element**	**Number**
Cu	22 mm	224 m	BPM-bellows	14	Injection kicker	4
Al	22 mm	605 m	In-line absorber	17	Extraction kicker	4
SS	22 mm	80 m	Gate valve	4	352 MHz rf-cavity	12
Al	16 × 6 mm	150 m	Flange	47	Rf transitions	3
Al	6 mm	25 m	ID transition	1	4^{th} harmonic cavity	1
Al	140 mm	20 m	Crotch absorber	2	Collimators	5
			Pumping cross	5		

Table 2.16. Characterization of the longitudinal impedance contribution of various impedance elements in terms of the total (ring summed) $\Im(Z_\parallel)/n$ and the loss factor of a 50-ps bunch.

Impedance source	**Number**	$\Im(Z_\parallel)/n$ **(Ω)**	$k_{\text{loss}}(\sigma_t = 50$ **ps)** **(V/pC)**
BPM-bellows	560	0.051	0.090
In-line absorber	640	0.048	0.037
Gate valve	160	0.015	0.002
Flange	1880	0.011	$< 10^{-3}$
ID transition	40	0.004	$< 10^{-3}$
Crotch absorber	80	0.007	0.002
Pumping cross	200	0.002	$< 10^{-3}$
Inj/ext kickers	8	0.02	0.94
352 MHz rf-cavity	12	0.001	4.5
Rf transitions	3	0.018	0.84
Resistive wall	NA	NA	1.13
Total	NA	0.175	7.5

gauges the relative contribution to the microwave instability, while the loss factor quantifies the energy loss to wakefields; the zero-current bunch length of 50 ps was chosen to compute the loss factor because κ_{loss} is typically negligible for the long equilibrium bunches in 48 bunch mode. Table 2.15 indicates that the BPMs and in-line photon absorbers are a dominant source of longitudinal impedance, largely because there are so many in the ring.

The driving terms for transverse instabilities scale as the product of the local dipole impedance with the beta function, which is related to the beta function-weighted transverse impedances shown in Fig. 2.5. The dominant resistive wall impedance in the narrow gap insertion device chambers can be recognized as the large contribution at $f \to 0$ that falls off $\sim |f|^{-1/2}$. The next two largest contributors are the BPM-bellows and in-line photon absorbers, which contribute nearly all the resonance-like peaks seen in Fig. 2.5. Slight variations in individual components will tend to broaden these resonance lines and decrease their amplitudes, which was found to slightly increase the instability threshold in numerical tests.

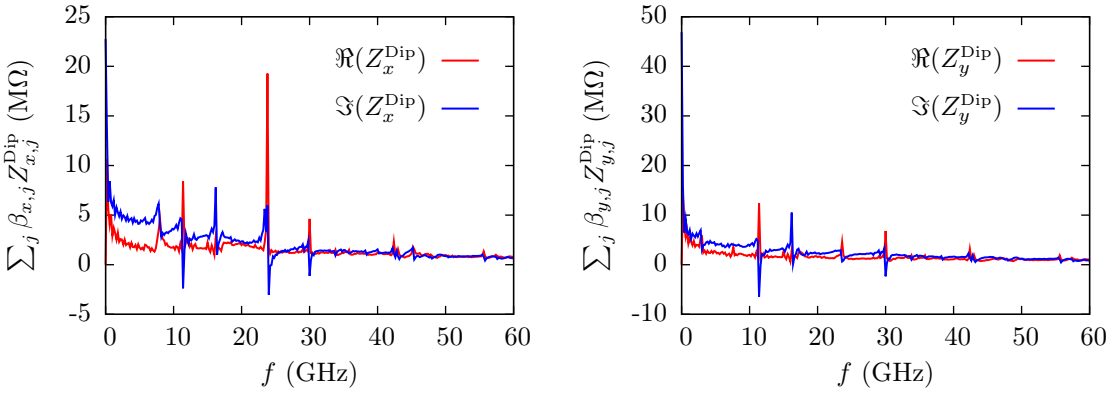

Figure 2.5. Beta function-weighted transverse dipole impedance for the APS-U ring.

2-2.4.2 Predictions of collective beam dynamics from tracking

Once sources of impedance have been identified and modeled, they are used with the tracking code `elegant` [49] to predict collective effects. The simplest such model lumps all sources of impedance into a single "impedance element" that is applied once per turn. In this model, the longitudinal impedance is determined by summing the contribution over all components in the ring, $Z_z^{\rm tot}(\omega) = \sum_j Z_{z,j}(\omega)$ for each component j, while the total transverse impedance of the ring is found by weighting the individual geometric contributions by their respective local beta functions $\beta_{x,j}$ and $\beta_{y,j}$ and summing:

$$Z_x^{\rm tot}(\omega) = \frac{1}{\beta_x} \sum_{\text{elements } j} \beta_{x,j} Z_{x,j}(\omega) \qquad\qquad Z_y^{\rm tot}(\omega) = \frac{1}{\beta_y} \sum_{\text{elements } j} \beta_{y,j} Z_{y,j}(\omega), \tag{2.1}$$

where β_x and β_y are the lattice functions at the location where the "lumped" impedance is applied in `elegant`. Frequently, particle tracking also uses a lumped, single-element model of the entire ring that that includes nonlinearities in the transverse and longitudinal motion, along with a lumped synchrotron radiation model. The main and harmonic rf systems are initially modeled as ideal cavities tuned for a nominally flat potential, which lengthens the bunch without beginning to split it.

Predictions of longitudinal effects are made by tracking 100,000 particles in `elegant` over 30,000 turns for a range of initial currents, and averaging the last 15,000 turns once equilibrium has been reached. Results are summarized in Fig. 2.6(a)-(b). Figure 2.6(a) shows the predicted bunch length as a function of current, while Fig. 2.6(b) shows how the energy spread increases above the microwave instability threshold of about 2.5 mA. This current is almost three times the 0.63 mA/bunch in 324-bunch mode, but well below the 4.2 mA/bunch planned for 48 bunch mode.

The results plotted in panels (a) and (b) of Fig. 2.6 assume that the higher harmonic cavity (HHC) is a prescribed harmonic voltage that exactly flattens the rf potential. However, APS-U plans to employ a passive HHC tuned to maximize lifetime by overstretching the bunch, as described in Sec. 2-2.7. Overstretching results in bunch lengths $\sim$ 100 ps, which increases the microwave instability threshold significantly higher, as seen in Fig. 2.6(c), which shows the energy spread as a function of the number of bunches at 200 mA. In this case the energy spread only modestly increases

in 48 bunch mode, and the beam has relatively small levels of longitudinal phase-space fluctuations, as shown in panel (d).

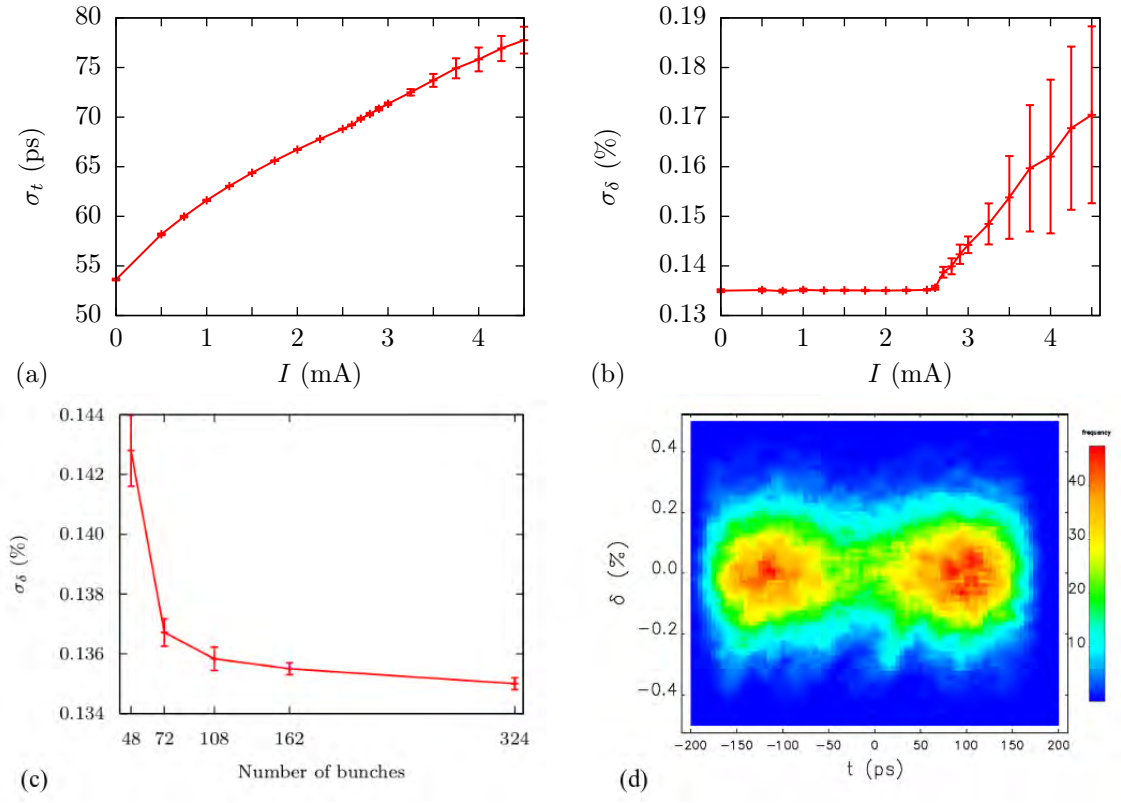

Figure 2.6. Bunch lengthening (a) and energy spread increase (b) as a function of current assuming a prescribed HHC set to flatten the potential. Error bars denote $\pm 2\sigma$ fluctuations. Panel (c) plots the energy spread as a function of bunch number for 200 mA total current and a passive HHC tuned to maximize lifetime. Panel (d) shows the predicted longitudinal phase space in 48 bunch mode with passive HHC.

Additional simulations using lumped-impedance tracking were used to determine the single-bunch instability threshold. These simulations tracked 200,000 macroparticles over 30,000 passes for various initial bunch currents. Once equilibrium was established after 15,000 turns, the beam was perturbed by 100 microns in x and y to initiate any potential instability, and the simulation output was investigated for evidence of undamped transverse oscillations and/or particle loss[1]. Results predict APS-U to be safe from transverse instabilities starting from equilibrium by a margin of 2.6 (i.e., 11 mA/bunch) at the operational chromaticity. While this is encouraging, transient collective instabilities at injection give a more stringent limit on the single bunch current [50, 51].

Because the injection process occurs over a relatively small ($\lesssim 500$) number of turns and involves distributions of particles that are far from equilibrium, it appears that a full accounting of physics within a single turn is important. For this reason, injection simulations employ element-by-element tracking—both with and without errors—including synchrotron radiation, the full array of physical

[1]These simulations are insensitive to the initial perturbation, with displacements of 50 and 200 microns giving nearly identical predictions.

apertures, and an impedance that is distributed over the ring. The distributed impedance model is composed of 15 impedance elements per sector, with one located at the midpoint of every ID straight section, and the other 14 placed next to each BPM. Each impedance element is repeated 40 times around the ring for the tracking, and includes both resistive wall and geometric contributions that are weighted by the relative β-function in a manner analogous to Eq. (2.1).

Simulations of injection using this distributed impedance model involved tracking 200,000 particles element-by-element through the ring, assuming that the initial 15.3-nC booster bunch has $\sigma_t = 100$ ps, $\sigma_\delta = 0.12$ %, $\varepsilon_x = 60$ nm, and $\varepsilon_y = 16$ nm. Fourteen post-commissioning error ensembles were used, with five having the smallest dynamic acceptance (DA) and the other nine chosen to span the DA in 10% increments. While several previous 42-pm lattices showed fairly strong instabilities at injection [51], the final lattice showed no such instability and $\lesssim 1$ % particle loss provided the injected bunch is within 200 microns of the design orbit. It was found that resiliance to these transient instabilities results from a large tune-shift with amplitude in the final lattice that provides stabilizing Landau damping. Indeed, simulations show that the injection process is stable even if the transverse impedance is doubled, while a feedback system capable of a 0.5 microradian maximum kick increases this margin to almost a factor of 3. Finally, it was found that injection instabilities observed in earlier lattices can be stabilized by using octupoles to increase the tune-shift with amplitude. Since the eight-pole correctors can provide an octupole field, they provide an additional tool to tame instabilities at injection.

2-2.4.3 Rf Heating and the impedance test stand

In addition to instabilities, longitudinal wakefields lead to rf heating of vacuum chamber components, which can be a serious issue if components are not properly designed. Components must be safe in normal operation with sufficient margin such that they are not damaged if the bunch-lengthening system were to be turned off (detuned). It was found that the BPM-bellows assembly and the stripline kickers are the most critical components, largely because they are difficult to efficiently cool and are sensitive to relatively small amounts of heating. Nevertheless, simulations indicate [52] that rf heating should be manageable. Both of these components are planned to be tested with beam, either in the present APS or NSLS-II.

An experimental effort is also underway to perform impedance-related measurements on various vacuum components as a way to complement, validate, and cross-check electromagnetic simulations. The first experiments used the traditional coaxial wire technique to assess the impedance associated with the non-evaporative getter (NEG) coating planned for the copper FODO section. Measurements showed that the NEG coating contributed a neglibly small impedance for frequencies below 20 GHz, as predicted by simulations [53]; to be more precise, the measured difference between the pure copper and the NEG-coated copper at low frequencies (~ 5 GHz) was 0.15 dB or less, which was comparable to the $\lesssim 0.1$ dB difference in S_{21} found when the same chamber was measured on two separate days. Around 20-30 GHz, the measured difference between coated and uncoated chambers were $\lesssim 1$ dB, while measurements of the same chambers that were separated by several weeks were repeatable to within ± 0.5 dB. Hence, the measurement is consistent with the NEG coating having little to no impedance cost up to 30 GHz, and that it at most increases the high-frequency impedance by $\sim 50\%$. We expect similar results for the NEG coated multiplet section. Since the FODO and multiplet sections combine to contribute only $\sim 7\%$ of the resistive wall's beta-function weighted dipolar impedance $\beta_y Z_y^{\mathrm{rw}}$, the contribution of the NEG should be very

small.

Further experiments are designed to measure the geometric impedance of a variety of APS-U vacuum components, including the BPM-bellows assembly, the gate valve, rf-liner options for flanges, and potentially other components, such as the injection/extraction kicker. A Gobau-line-based [54, 55] impedance stand was designed and manufactured to perform these experiments. The G-line has been benchmarked with test cavities, and been used to verify small impedance with no resonances below 10 GHz for the pumping cross, gate valve, and BPM-bellows assembly [53, 56]. Recently, the G-line has been also used to refine the design for rf-gaskets of the QCF flanges.

2-2.5 Multi-bunch Stability

Each circulating bunch leaves behind a wakefield or ions (from the residual gas) that will affect the motion of bunches behind it. If there is a resonance between the long-range wakefields and the beam frequencies, positive feedback may occur and produce an instability. The main concern is not a beam loss, but creating some sustained bunch oscillation in any plane, which would effectively increase the emittance or energy spread of the electron beam.

The long-range wakefields from the present 352 MHz accelerating rf cavities are the strongest in the ring. The rest of this section will summarize the work done to estimate the instability driving terms from these wakefields under several operating conditions and how their effect can be mitigated by damping and by tuning the cavities. Ion effects will be presented in Section 2-2.6. The other effect is the long-range resistive wall wake, which has been explored in multi-particle tracking and found to be controllable with weak feedback [50]. (The short-range resistive wall impedance is significant for single bunch stability, and is covered in Section 2-2.4.)

Stability depends on whether the various natural and applied damping effects—described quantitatively in Table 2.17 [1]—can suppress the aforementioned driving effects. In the transverse planes, strong damping effects come from the chromaticity, while a moderately strong damping effect in the longitudinal plane comes from the Landau damping due to the higher-harmonic cavity (HHC). Bunch-by-bunch feedback systems can be designed to damp multi-bunch instabilities that have reasonable growth rates. In an approximation, one can treat the damping and driving terms separately and determine from the total effect whether the beam will be stable or not. In the more complicated conditions of the APS-U ring (i.e., in the presence of the HHC and high bunch charge) one cannot treat the damping and driving terms separately, and tracking must be done to verify stability.

2-2.5.1 Cavity Impedance

The strongest wakefield source for multi-bunch instability is expected to be the higher-order modes (HOMs) of the rf cavities. Twelve of the sixteen 352-MHz copper rf cavities will be retained in the new ring, thus making the HOM impedance effect roughly similar to that of the existing ring. The formula for growth rates for symmetric bunch patterns and a single HOM gives the general dependence on ring parameters; when a HOM is exactly resonant with the multi-bunch beam mode, the growth rate of the worst multi-bunch mode is

$$G_s = \frac{\alpha_c I_{\text{total}}}{2(E/e)\nu_s}(R_s f_{\text{HOM}}) \exp(-\omega_{\text{HOM}}^2 \sigma_t^2) \tag{2.2}$$

Table 2.17. Summary of damping rates from various mechanisms

Mechanisms	**Horizontal (s^{-1})**	**Vertical (s^{-1})**	**Longitudinal (s^{-1})**
Synchrotron radiation	146	65	49
Coherent[b]	6800	6800	N/A
Active feedback	3600	10000	690[c]
HHC damping rate	N/A	N/A	188
Expected minimum passive damping rate	6800	6800	238
Expected minimum active damping rate	10000	17000	740

[a] Chromaticity setting of 5.0
[b] This is a specification from tracking simulations described in [1, section 4-2.9.5].

for the longitudinal plane and

$$G_{x,y} = \frac{f_0 I_{\text{total}}}{2(E/e)}(\beta_{x,y} R_t)\exp(-\omega_{\text{HOM}}^2 \sigma_t^2) \tag{2.3}$$

for the transverse planes, with α_c the momentum compaction, I_{total} the total stored current, E/e the beam energy in eV, ν_s the synchrotron frequency, R_s the shunt impedance (circuit model) of the monopole HOM, f_{HOM} the frequency of the HOM resonator, $\omega_{\text{HOM}} = 2\pi f_{\text{HOM}}$, σ_t the bunch length, f_0 the revolution frequency, $\beta_{x,y}$ the betatron function at the rf cavities, and R_t the transverse shunt impedance (circuit model) of the dipole modes. The exponential factor is a bunch form factor, which is close to unity for the HOM frequencies of interest in the 352-MHz cavities. Off-resonance, the growth rates from HOMs are less and follow a Lorentzian with FWHM of f_{HOM}/Q. Changes in ring parameters compared to the present-day APS make the beam dynamics relatively less favorable for stability in general.

To give an idea of the problem at hand, Fig. 2.7 shows the monopole HOMs for the 352-MHz cavity compared with Eq. (2.2) using a growth rate limit equal to the synchrotron radiation damping rate. There are five modes above threshold in each cavity. If one or more of these HOMs are resonant with a multi-bunch beam mode, an instability occur. The HOM at 540 MHz is shown as damped by factor of 8 with a HOM damper already installed in sector 38 in APS. Later it is shown that the undamped 540 MHz HOM would be safe when tuned away from a beam resonance. (The HOMs of the bunch lengthening cavity are ignored because they will be heavily damped, with the Q's in the 1000's and the shunt impedance about 1000 Ω, which is 1000× smaller than the worst HOM of the regualr APS cavities. Similar considerations apply to the longitudinal feedback kicker cavities.)

Reference [1] shows that in the transverse plane the strong coherent damping in the transverse plane plus a similar amount of damping from the transverse feedback systems suppresses any possible driving terms from dipole HOMs. Thus the APS-U beam is stable in the transverse plane up to 200 mA.

In the longitudinal plane, the damping is weak and the possibility of instability is real if an HOM frequency coincides with a harmonic of the revolution frequency. This may happen due to the initial shape of the cavity after assembly plus additional dimension changes through fundamental tuner position adjustment and temperature variation from cooling water and cavity wall power. Measurements show that 0.5 °C or 1 kW is enough to move any HOM in and out of resonance. Thus

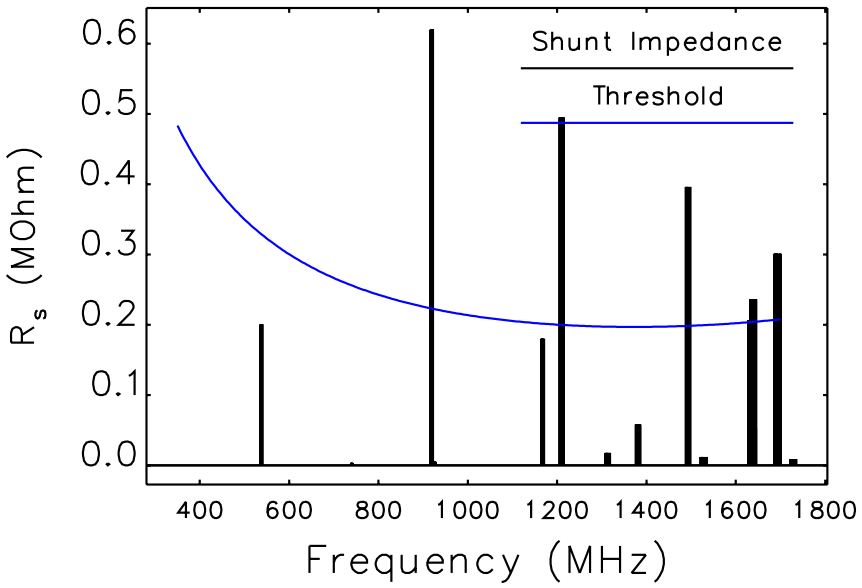

Figure 2.7. Monopole shunt impedances of damped 352-MHz cavity. Ensembles of HOM families with stepped frequencies appear as thick lines. Threshold is calculated using bunch form factor for $\sigma_z = 2.5$ cm. The mode at 540 MHz as shown is damped by 8x by HOM dampers.

the frequency of the HOMs are considered uncertain until measured under APS-U operating (i.e. powered) conditions. Hence, a Monte Carlo calculation of growth rates using normal mode analysis with possible HOM frequencies must be conducted to determine the probability of instability and to specify mitigating strategies.

2-2.5.2 Monte Carlo Calculation of Growth Rates

References [57, 58] report on calculations of the probability of longitudinal instability using the frequency of the monopole HOMs as a random variable [59, 60], and cavity temperature as a tuning variable. The calculation of beam mode growth rates described therein is limited to the single rf condition (i.e. when HHC is off) because of the normal mode analysis [61, 62, 63] adopted, although it is expected from recent theoretical work [64] that qualitatively similar behavior will be seen when the non-harmonic potential of HHC is included.

Comparisons of outcomes for different design decisions can be made with the above Monte Carlo method, which can in principle be verified by full multi-particle, multi-bunch tracking with the HHC on or off with a subset of the seeds. One such design decision is whether to build HOM dampers for the twelve cavities identical to those in the sector 38 cavities. Another is whether individually-controlled cooling water stations should be acquired for the twelve cavities in place of the present system which gangs groups of four cavities. The latter would supposedly reduce the potential of temperature tuning.

The simulations show that leaving the cavities undamped actually makes the temperature tuning easier, i.e. the resonance peaks are sharper and more responsive to temperature. Having three temperature stations for twelve cavities turns out not to be significantly detrimental.

The references also compare two algorithms for temperature tuning, one using simple temperature steps in each cavity until conditions improve, and a "precision" method using HOM frequency temperature-dependence information for each cavity. Given the ability to detect the HOM resonant peak frequencies precisely enough ($\sim$ 10 kHz) using "excite-damp" measurements [65, 66] it is assumed that the precision algorithm would be used in practice.

Figure 2.8 (from [58]) shows the precision tuning cumulative distribution function (CDFs) of all four combinations of cases of twelve and three temperature controls and with and without HOM dampers for three bunch patterns.

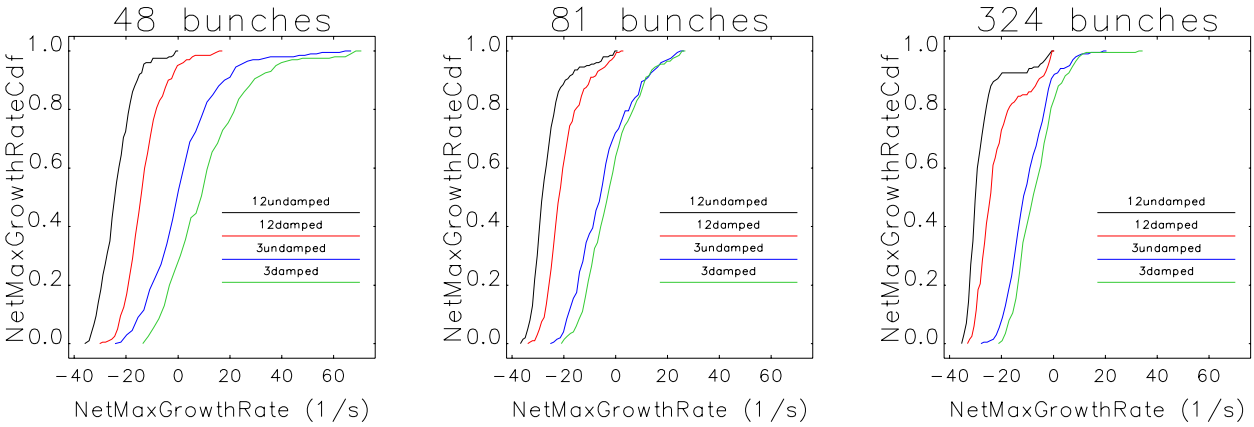

Figure 2.8. Cumulative distributions of net longitudinal instability growth rates (less synchrotron radiation damping) for precision temperature tuning. Individualized temperature cavity controls give better results.

Table 2.17 summarizes the present Monte Carlo analysis of the stability condition for multi-bunch modes in the three planes excluding feedback. The transverse planes are clearly stable because of coherent damping from chromaticity.

Table 2.18. Summary of stability conditions with HHC off using normal-mode calculations

	Growth Rate[a] **(s^{-1})**	**Damping Rate**[b] **(s^{-1})**	**Stability**
Horizontal	485	6800	Yes
Vertical	255	6800	Yes
Longitudinal with tuning	110	49	No, need feedback

[a] Worst 98th percentile, without synchrotron radiation.
[b] Expected damping rates from Table 2.17 excluding feedback.

For the three bunch patterns and single rf frequency, the maximum net growth rate is 60 s^{-1}, which is low enough for the planned longitudinal feedback (LFB) system. However, this must be verified with tracking, especially if the HHC is turned on. Figure 2.9 shows results of 48-bunch, full-impedance model tracking using `Pelegant`[67] for an eleven cases of randomized HOM frequency

data. The simulations include the short-range impedance, beam-loaded main cavity with feedback, and sychrotron radiation. The cases were chosen to cover the full range of growth rates from the normal-mode calculations [68]. Three tuning conditions are shown: "nominal", before any tuning, "step" for simple stepping of temperatures, and "precision" for precision tuning. The growth rates for "nominal" HOM frequencies come out a little higher than the corresponding normal mode calculation of Table 2.18. On the other hand, the beam is stabler with "precision" tuning for all eleven cases.

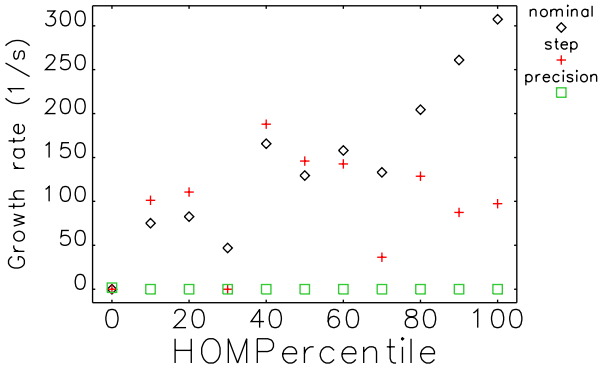

Figure 2.9. Growth rates from tracking for eleven samples taken from the Monte Carlo calculation of HOM frequency with HHC off. Nominal is the condition before attempting any temperature tuning. "Step" and "precision" refer to the two different temperature tuning algorithms.

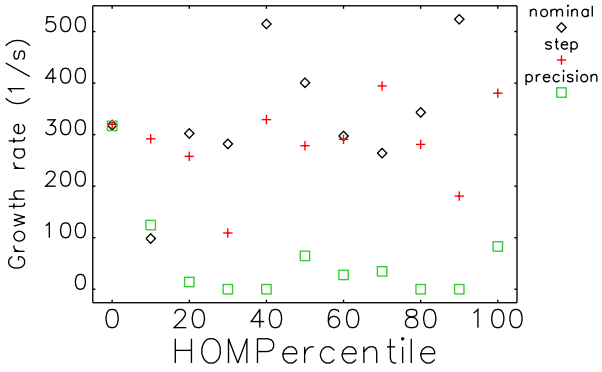

Figure 2.10. Growth rates from tracking for eleven samples taken from the Monte Carlo calculation of HOM frequency with HHC on. Nominal is the condition before attempting any temperature tuning. "Step" and "Precision" refer to the two different temperature tuning algorithms.

Figure 2.10 shows the tracking results with the HHC included. Indeed, the growth rates are larger in general for the three tuning conditions. This two-to-three-fold increase in growth rates is explained by the by the decrease in the synchrotron frequency, which overwhelms the beneficial effect of Landau damping. With precision tuning the highest growth rate is 300 s^{-1}, higher than expected but low enough for the planned longitudinal feedback system.

Tracking studies showed [69] that feedback must use the energy error signal from the bunches rather that the traditional phase offset measurement, since the synchrotron frequency is very low while the growth rates are high. A possible front-end concept was developed by Dimtel, Inc. for energy error detection. Simulations with longitudinal feedback were done[70] with various kicker strength limits, resulting in a specification of 4 kV. These simulations were performed by looking at instability following sudden loss of a single bunch in a 48-bunch fill, which introduces strong transients that can lead of loss of other bunches.

In conclusion, transverse coherent damping is expected to be strong in the nominal MBA lattice, and thus, the lower synchrotron radiation damping rate won't be an issue for the transverse plane. In the longitudinal plane, a temperature tuning procedure for the individual cavities and a feedback system was found to be necessary. The precision tuning method can be adopted for optimum HOM frequency placement. Cavity HOM dampers are unnecessary, and may even be a hindrance to temperature tuning. Individual temperature tuning of the cavities doesn't seem to be critical, as keeping the present three independent water stations seems sufficient. Tracking studies show that

a longitudinal feedback system with a kick strength of up to 4 kV appears sufficient to stabilize the beam, provided an energy-sensing mode is used.

2-2.6 Ion Trapping and Instabilities

Ions are produced in an accelerator when the beam ionizes residual gas in the vacuum chamber. If the beam is negatively charged, ions can become trapped in the beam's potential, potentially leading to a transverse instability. The strength of the instability is generally proportional to the average beam current, and inversely proportional to the beam size [71]. Because the APS-U storage ring is planned to run with high charge, low emittance electron bunches, trapped ions could cause instability. However, if the beam density is sufficiently high, the ions can receive a very strong kick from a single bunch, and escape before the next bunch arrives. Ion trapping can be characterized by a local trapping parameter, which depends on the bunch charge, bunch spacing, and beam size [72]. Analytic calculaitons show that ions will only be trapped in 324 bunch mode, with $\epsilon_y \approx \epsilon_x$ [73]. The trapping will be localized in the multiplet sections, where the beam size is relatively large.

Since the ion trapping is localized, it is important to know how the gas pressure will vary around the ring, which is provided using calculations described in Section **??**. Ion simulation results are presented below for 200 mA after a dose of 1000 A-hr (corresponding to roughly one year operation at full current) and 100 A-hr (corresponding to early operation at full current).

The initial APS-U vacuum design [74] incorporated NEG coating only in the FODO sections. Vacuum simulations showed a pressure bump in the multiplet sections, where the ions are trapped. More recently, it was decided to coat the doublet and multiplet sections. This leads to a dramatic reduction in the pressure of the coated sections, which is very helpful for ion instability.

To evaluate the possibility of ion instability in the APS-U, we used an ion simulation code developed at SLAC [75], which models the interaction between the beam and ions at multiple points ($\sim$ 1400) around the ring. This code was previously used to study an ion-induced tune shift in the PAR [76]. In this code the ions are modeled using macroparticles, but the beam is rigid (with only centroid motion allowed). The simulations incorporate the realistic vacuum pressure profiles just described.

Simulations without train gaps (see below) show a very fast-growing vertical instability, which starts to saturate when the beam motion reaches about 10% of the vertical beam size. Even this small amount of beam motion is enough to shake out some of the ions, leading to a reduction in the ion density. Thus the instability is to some extent self-limiting, though unfortunately not to the extent that it stops growing altogether. The reduction in pressure due to the increased NEG coverage lowers the peak ion density at 1000 A-hrs by a factor of 3. This has a strong effect on the ion instability—the beam amplitude after 1000 turns is reduced from $\sim 2\sigma_y$ to $\sim 0.5\sigma_y$. The initial instability growth rate (before saturation) is reduced from $\sim$31/msec to $\sim$15/msec. This can be compared with the three sources of vertical damping in the APS-U: synchrotron radiation (0.062/msec), coherent damping ($\sim$6.80/msec, though note this is not exponential damping) [77, 78], and a transverse feedback system [79] ($\sim$5-10/msec). Unfortunately, none of these will be fast enough to damp the ion instability, even with the increased NEG coating.

One common technique for mitigating ion instability is to use gaps between bunch trains, to allow the ions to clear out [80]. A downside of this technique is that the missing bunches can cause transients

in the RF system, leading to variations in the bunch length, phase, and lifetime along the train [81, 82, 83]. To minimize these impacts, the "missing charge" is distributed to the bunches adjacent to the gaps, which are referred to as "guard bunches". Simulations show that this arrangement should have little impact on the longitudinal parameters and Touschek lifetime of the bunches (other than the double-charge guard bunches having half the lifetime) [1]. In addition, the high charge guard bunches before the gaps will provide a stronger kick to the ions, helping with the clearing process.

The ion simulation code described above has been modified to allow for the modeling of compensated gaps. Fig. 2.11 shows the instability amplitude vs time for different numbers of train gaps, with 1000 A-hr beam conditioning. There are two empty buckets in each gap, with the missing charge distributed to the guard bunches before and after the gap. Two train gaps is enough to nearly eliminate the instability– the initial growth rate is reduced by almost two orders of magnitude, from ∼15/ms to to ∼0.2/ms. With 12 or more gaps there is no observable instability. Since the expected vertical damping rate at the APS-U is ∼6-10/ms, two gaps should be more than sufficient. Increasing the number of buckets in the gap was not found to have an appreciable effect on the simulated instability growth rate.

Fig. 2.12 shows the train gap comparison for 100 A-hr beam conditioning. The average pressure at 100 A-hr is significantly higher (3.54 nTorr, compared to 0.93 nTorr for 1000 A-hr), leading to an even faster initial instability growth. In this case, using two train gaps reduces the initial growth rate from ∼33/ms to ∼0.9/ms, still well below the expected vertical damping rate. Using more gaps further reduces the growth rate, down to ∼0.1/ms for 18 trains. In general, if two gaps proves to be insufficient (e.g. if the vacuum pressure is higher than expected), additional gaps can be used to further suppress the instability.

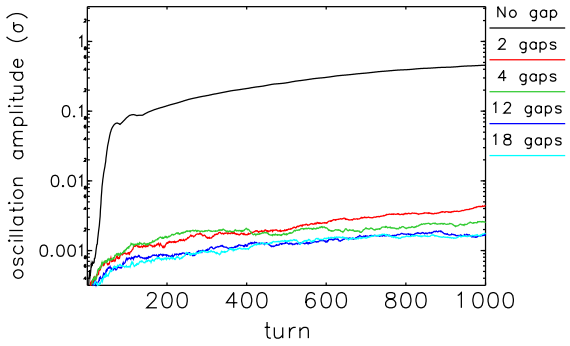

Figure 2.11. Ion instability amplitude (in units of vertical beam size) for 200 mA, 1000 A-hrs, and 2-bucket gaps.

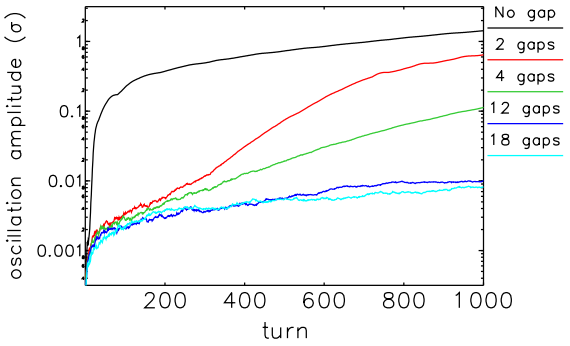

Figure 2.12. Ion instability amplitude (in units of vertical beam size) for 200 mA, 100 A-hrs, and 2-bucket gaps.

2-2.7 Beam Lifetime

There are two primary contributions to the beam lifetime: Touschek scattering and gas scattering. The quantum lifetime is extremely long since the rms beam sizes are more than an order of magnitude smaller than the dynamic acceptance. Similarly, the rms energy spread is more than an order of magnitude smaller than the minimum local momentum aperture. Hence, the quantum lifetime

contribution can be safely ignored. The total lifetime is reported in section 2-2.3, Table 2.13.

2-2.7.1 Touschek Lifetime including Harmonic Cavity

Lengthening the bunch is an important means of increasing the Touschek lifetime and also serves to limit the emittance-diluting effects of IBS. Further, it helps reduce rf heating of the beam position monitors, bellows, and other vacuum perturbations. An effective way to lengthen the bunch is using an passive higher-harmonic cavity, which flattens out the rf potential created by the main rf cavities.

Although approximate calculations are easily performed, tracking studies provide important detail. They include the exact time-dependence of the rf fields, self-consistent interaction of the beam with the cavity mode, longitudinal and transverse impedances, and higher-order beam transport effects. Beyond this, tracking studies permit exploration of issues such as bunch population variation, missing bunches from a train of equi-spaced bunches, the transient effect of a lost bunch, and other details. Many of these effects are described in detail in the PDR[1] and CD2 presentations[5, 6]. Table 2.19 shows parameters of the cavities, as used in the simulations.

Table 2.19. Assumed cavity parameters

System	Revolution Harmonic	R/Q (ohm)	Loaded Q	Number of cavities
Main	1296	208	9100	12
Harmonic	$4 * 1296$	109	variable	1

The HHC is passive, so that the voltage that lengthens each bunch is induced by the stored beam. The HHC detuning from the exact harmonic condition is a free parameter, within some limits, and is varied in order to maximize the Touschek lifetime. As the cavity is tuned closer to resonance, the bunch lengthens and eventually starts to show a double-humped time distribution when the HHC voltage exceeds the ideal "flat-potential" condition. With such a distribution, using a gaussian bunch length in computing the Touschek lifetime is not reliable. Hence, a slice-based approach was developed that uses turn-by-turn samples of the longitudinal distribution from tracking simulations. These are used for slice-based computation of the effects of intrabeam scattering [35, 36] and then for slice-based computation of the Touschek scattering rate [36] using Piwinski's method [37].

The maximum Touschek lifetime is obtained for "overstretched" bunches, but will begin to decrease if the bunches are stretched too far. This is particularly evident in the results for 324-bunch, 200-mA mode, as shown in Fig. 2.13, where the maximum lifetime is achieved for $\Delta f_h = 11$ kHz. For 48-bunch, 200-mA mode, the optimum is near $\Delta f_h = 9$ kHz, as seen in Fig. 2.14, below which the beam is quasi-stable. In addition to maximizing the Touschek lifetime, over-stretching the bunch helps to suppress the microwave instability and intrabeam scattering in 48-bunch mode.

These results are for a fixed main rf voltage of 4.6 MV, which provides a bucket height of about $\pm 4.6\%$. Since this slightly exceeds the maximum local momentum acceptance, slightly longer Touschek lifetimes can be obtained by reducing the main rf voltage to match the momentum acceptance from nonlinear dynamics. This provides improvements of $\sim$10\$.

The results shown above are for uniform, symmetric fills. In 324-bunch mode, we will require ion-clearing gaps, as discussed in section 2-2.6. Traditionally, this was done by removing charge from

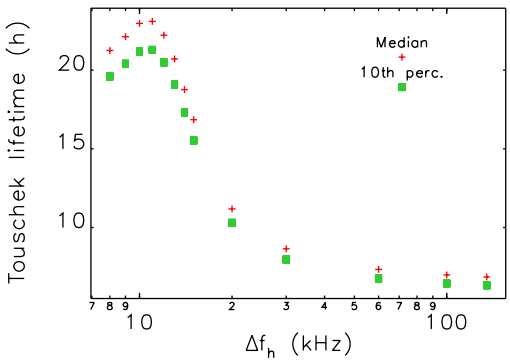

Figure 2.13. Median and 10^{th}-percentile Touschek lifetime for 324-bunch, 200-mA mode as a function of the detuning of the HHC.

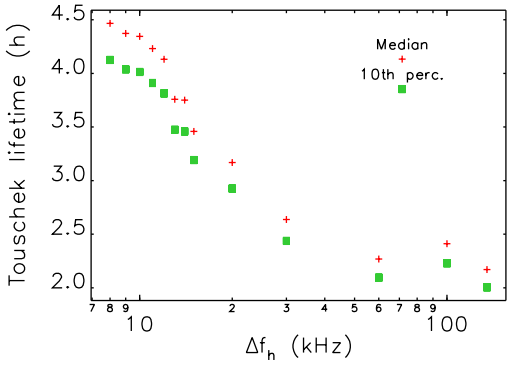

Figure 2.14. Median and 10^{th}-percentile Touschek lifetime for 48-bunch, 200-mA mode as a function of the detuning of the HHC.

several buckets and uniformly distributing that charge to the remaining bunches. Even if done symmetrically, this produces rf transients that will interfere with the ideal functioning of the HHC. To reduce this effect, the "guard bunch" scheme [84] was introduced. In this scheme, the ion-clearing gaps are bracketed by a series higher-charge bunches that contain the charge removed from the gap. This greatly reduces the rf transients and ensures that the lifetime of the bulk of the bunches is unchanged [1], as seen in Figs. 2.15 and 2.16.

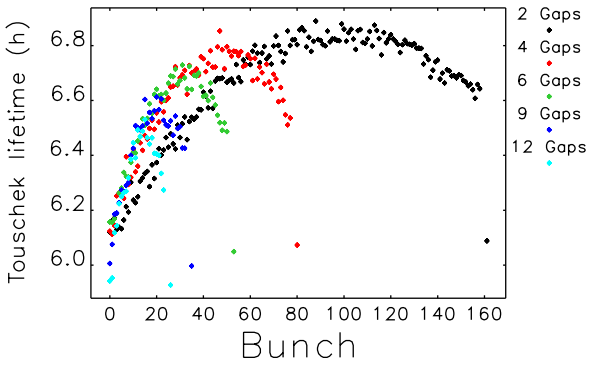

Figure 2.15. Touschek lifetime for unique bunches when various numbers of simple two-bunch gaps are used in the nominally 324-bunch fill.

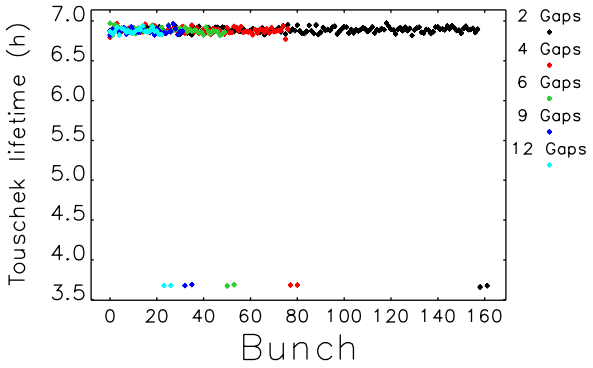

Figure 2.16. Touschek lifetime for unique bunches when various numbers of compensated two-bunch gaps are used in the nominally 324-bunch fill.

2-2.7.2 Gas Scattering Lifetime Based on Species-Specific Pressure Profiles

The gas scattering lifetime includes contributions from elastic gas scattering and inelastic gas bremsstrahlung [85]. The elastic gas scattering lifetime is affected by the local angular acceptance, while the gas bremsstrahlung lifetime is affected by the local momentum acceptance (LMA). Tracking-based methods [40, 41] were used to predict not only the gas scattering lifetimes, but

also the distribution of lost particles around the ring. In addition, the gas scattering calculations made use of the species- and position-dependent gas pressure profiles, described in section **??**. Since the gas pressure depends on the amount of vacuum system conditioning and the stored beam current, computations were performed for several dose levels, from 5 A-h to 1000 A-h and several corresponding stored beam currents.

Table 2.20 lists the 10^{th}-percentile elastic and bremsstrahlung-scattering lifetimes, τ_e and τ_b respectively, along with the total gas-scattering lifetime τ_g, for each condition. Note that these results are for the lattice operated on the difference resonance, giving $\epsilon_y/\epsilon_x \approx 1$. For operation with $\epsilon_y/\epsilon_x \approx 0.1$, the DA and LMA are slightly reduced, giving slightly lower gas scattering lifetime. The values for 1000 A-h and 200 mA are used for computation of the total beam lifetimes displayed in Table 2.13.

Table 2.20. 10th-percentile gas-scattering lifetimes for three dose points and stored beam currents.

Dose A*h	Current mA	$\tau_{e,10}$ h	$\tau_{b,10}$ h	$\tau_{g,10}$ h
5	25	32.7	32.9	16.5
100	200	25.5	25.9	13.0
1000	200	97.9	99.7	49.9

2-2.8 Swap-out Injection Design and Performance

An on-axis vertical injection scheme was adopted for the MBA lattice design. It utilizes fast stripline kicker technology, which works together with a direct current (DC) Lambertson septum, and performs single-bunch "swap-out" injection [86, 87]. In this implementation of swap-out injection, the stored bunch with the least bunch current is extracted and dumped in the swap-out dump located inside the A:M1 magnets in sector 39 and a fresh bunch is injected immediately into the same bucket in the ID straight of sector 39. A conceptual layout of the extraction/injection region is shown in Fig. 2.17.

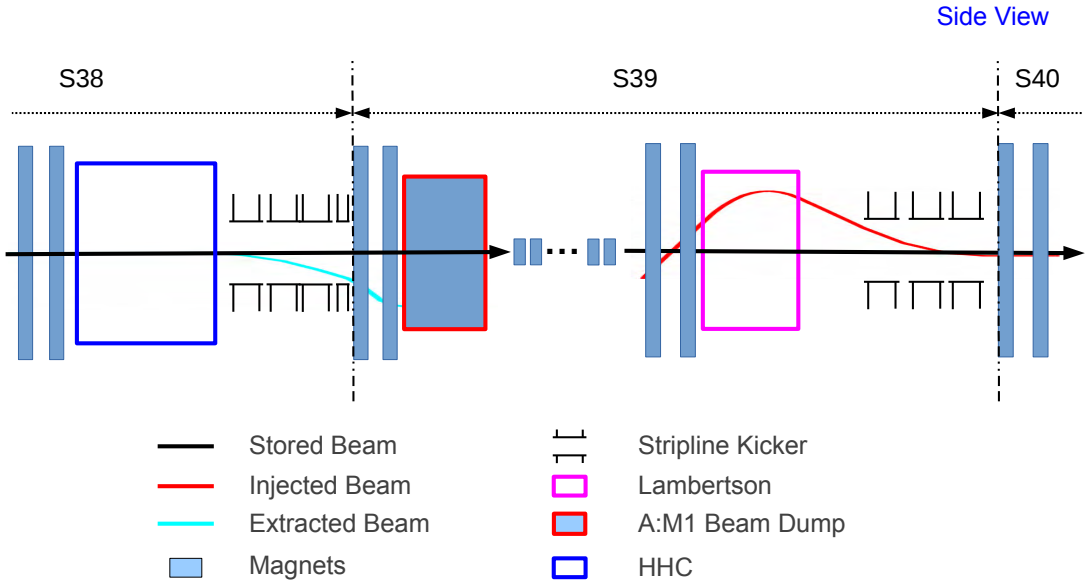

Figure 2.17. Schematic layout of extraction-injection region. Red line shows the current BTS line configuration. Blue box shows the section requiring modification for APSU.

2-2.8.1 Injection Line Design

Injection section of SR

A schematic of the injection section together with the projected injected beam orbit is shown in Fig. 2.18. The Lambertson magnet is slightly tilted about the z axis to provide a gentle vertical bend that brings the injected beam trajectory close to $y = 0$ when it passes through magnets Q1 and Q2; The main design parameters are optimized and determined by considering difficulty, risk, and availability of suitable technology on the Lambertson septum and fast stripline kicker system [88]. These parameters are listed in Table 2.21. The beam stay clear is carefully checked for this region [89].

Matching of BTS line

As shown in Fig. 2.18, the injected beam trajectory needs to be matched in both the horizontal and the vertical direction. This is realized by two slightly tilted dipoles in the BTS, which act together

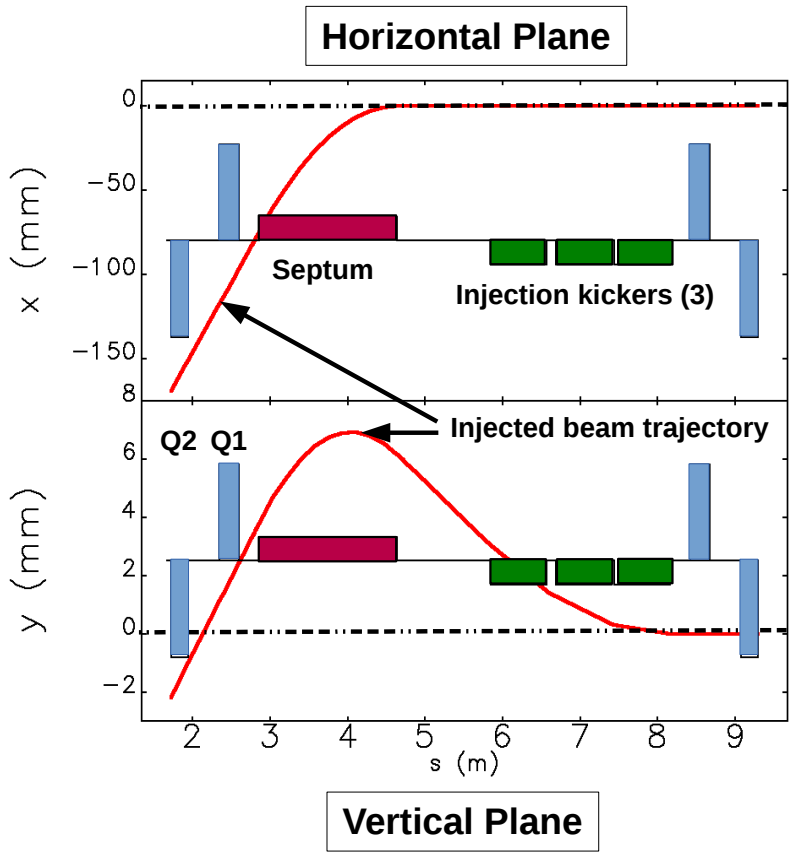

Figure 2.18. Layout of the on-axis injection section and the projected injected beam orbit.

with the tilted septum magnet and stripline kickers to bring the injected beam on axis. Since the new BTS line must also fit into the existing tunnel, only the SR side of BTS line is modified for matching the geometry; the Booster side of APS BTS line layout is unchanged, see Fig. 2.19. As the injected beam has to pass through S39B:Q[12], thus the stray fields of S39B:Q1 is included in the design. Stray field from S39B:Q2 is much smaller due to the large injected beam orbit offset here, and is assumed to be shielded.

The BTS line optical functions are matched to the SR at the injection point using the 132-nm Booster lattice as input, see Fig. 2.20[90]. The main parameters of the BTS magnets are listed in Table 2.22

2-2.8.2 Swap-out Extraction Section

The swap-out extraction kickers are located at the end of sector 38, sharing the same ID straight section with the bunch lengthening high harmonic cavity (HHC), as shown in Fig. 2.17. As a result, the entire swap-out injection process is largely transparent to the rf systems, so there are no significant beam loading changes when the swap-out is successfully performed. (See **??** for a discussion of transients that occur when swap-out fails.) This section includes one shorter length

Table 2.21. Main parameters of injection elements

Title	Description	Value	Unit
Stripline	Blade Length	0.72	m
	Body Length	0.75	m
	Gap	9	mm
	Pulser Voltage	±18	kV
	Kick Angle	0.864	mrad
Lambertson	Effective Length	1.78	m
	Wall Thickness	2	mm
	Effective Field	0.95	T
	Bending Angle	84.55	mrad
	Tilt Angle	93	mrad
	Stored Beam Half Aperture (x×y)	4×3	mm

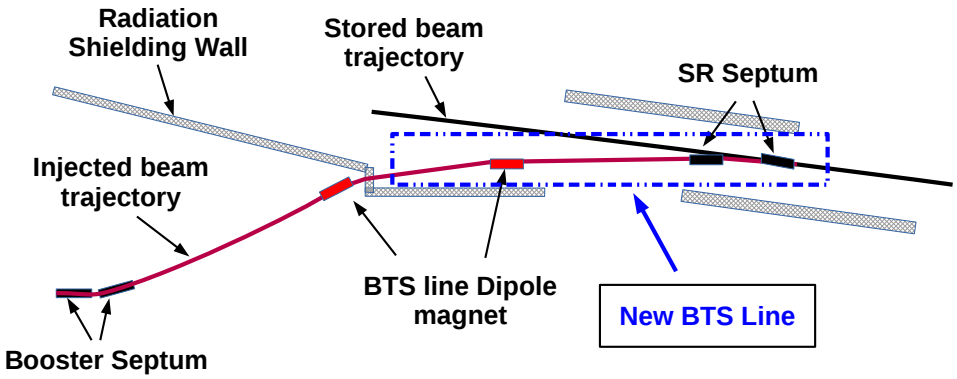

Figure 2.19. Schematic layout of APS injection region.

pre-kicker, as discussed below, to reduce the energy density of the dumped bunch (see 2-2.9.2 for discussion of the necessity of this), and three normal length stripline kickers to dump the diluted bunch, ∼250 turns after the pre-kicker fires, to the swap-out dump in the S39A:M1 magnet. If any one extraction kicker out of the three does not pulse, the bunch is still dumped at the intended location [91]. The worst case is when the first extraction kicker misses the pulse; this moves the dump location to the downstream end of the swap-out dump. The layout of the extraction section, including vacuum chamber size variation, the first turn of pre-kicked beam trajectory, beam orbit and dump location for normal operation, and the worst case of misfiring of the first stripline kicker, is shown in Fig. 2.21.

As described in 2-2.9.2, because of the high energy density in the bunch, it is inadvisable to extract a bunch into the swap-out dump without taking steps to inflate the bunch volume. One way to do this is using a spoiler, but there is no material that can be used for this purpose that will not be destroyed. However, decoherence following a small vertical kick has been found adequate for this purpose. In this scheme, the bunch to be extracted is pre-kicked some time prior to when it needs to be extracted. Simulations were performed that showed that a kick of 0.10 mrad several hundred turns prior to extraction was sufficient to cause a ∼100-fold reduction of the particle density without

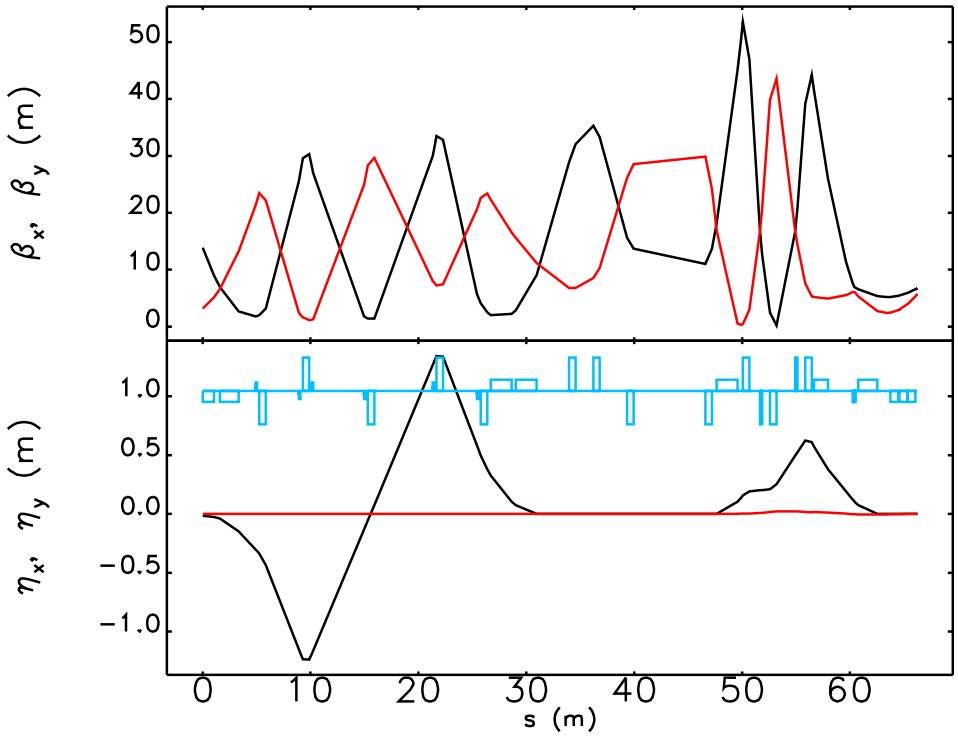

Figure 2.20. Optical functions of the BTS transfer line.

any beam loss, even for 15.3 nC/bunch [2]. At this point, the bunch can be safely extracted into copper, aluminum, or other materials.

2-2.8.3 Injection Performance

Injection performance was modeled [34, 92] in the presence of errors in the booster, the booster-to-storage-ring (BTS) transport line, and the storage ring, as well as errors in the storage ring via the commissioning ensembles. For each commissioning ensemble, 30 injection "shots" were simulated. Table 2.23 summarizes the errors used in the simulations. In addition to such errors, the modeling included the transverse variation of the deflection of the stripline kickers as well as the measured time-dependence of the kicker waveforms (convolved with the stripline length).

To assess the effect of the booster emittance, several runs were performed with inflated emittances. Even with the inflated emittance, the predicted injection losses are low, with a high probability of losses below the few percent level, as seen in Fig. 2.22. Even for the most extreme situation (50% increase in both emittances), the losses are below 4% in 90% of cases. Further, since the various cases represent the end result of the automated commissioning algorithm, it is expected that improvements will be possible with targeted effort.

Figure 2.23 shows the locations of the lost particles for the nominal beam parameters. The highest localized losses are seen in the straight section containing the SCAPE device, which has a round beam pipe with an inside diameter of only 6 mm. Other high loss points are the five horizontal

Table 2.22. BTS line main magnet parameters

Name	Length m	Angle deg	$K1$ m^{-2}	New Magnet	New Location
BTS:AQ1	0.6	—	-0.590	No	No
BTS:AQ2	0.6	—	0.596	No	No
BTS:AQ3	0.6	—	-0.441	No	No
BTS:AQ4	0.6	—	0.563	No	No
BTS:AQ5	0.6	—	-0.330	No	No
BTS:AB1	1.938	4.437	—	No	No
BTS:AB2	1.938	4.437	—	No	No
BTS:BQ1	0.6	—	0.191	No	No
BTS:BQ2	0.6	—	0.256	No	Yes
BTS:BQ3	0.6	—	-0.244	No	Yes
BTS:BQ4	0.6	—	-0.591	No	Yes
BTS:BB1	1.938	6.190	—	No	Yes
BTS:CB1	1.3	4.076	—	Yes	Yes
BTS:CQ1	0.6	—	0.918	No	Yes
BTS:CQ2	0.6	—	-0.964	No	Yes
BTS:CQ3	0.6	—	0.849	No	Yes
BTS:CSQ1	0.2	—	-0.208	Yes	Yes
BTS:CSQ2	0.2	—	0.067	Yes	Yes

collimators. Attempts to reduce the losses at the SCAPE and other insertion devices were made by introducing more vertical collimators with reduced aperture; however, the primary effect was to increase the overall loss rate without significant decreases in the loss rate at the SCAPE device.

2-2.8.4 Perturbations to Stored Beam

So far, the analysis has only looked at the variation in injection efficiency. However, the stored beam may also be perturbed by a residual kick that originates from a prolonged kicker waveform tail, an after-pulse from the kicker power supply, or a reflection from the stripline kicker structure. A detailed simulation study[93] including machine errors, collective effects, and feedback systems shows that the minimum tolerable spurious kick strength is ∼0.175-mrad for 48-bunch mode, corresponding to $A_y \leq 73$nm. For 324-bunch mode, due to much weaker collective effects, the tolerable spurious kick strength is ∼0.4-mrad, corresponding to $A_y \leq 383$nm. This implies a requirement of about 6% of the injection kick for the spurious kicks in 48-bunch mode, and 14% in 324-bunch mode (where bunches are closer together). These requirements can be apportioned between static errors (due, for example, to differences between the injection and extraction waveforms) and random errors (due, for example, to timing jitter) as described in Section 4-2.10.4 of [1].

2-2.9 Beam Dumps and Collimation

The beam dump and collimation system serves several purposes, including:

1. Radiation safety — particle loss should be localized as much as possible so that radiation levels in occupied areas can be minimized with the use of local shielding.

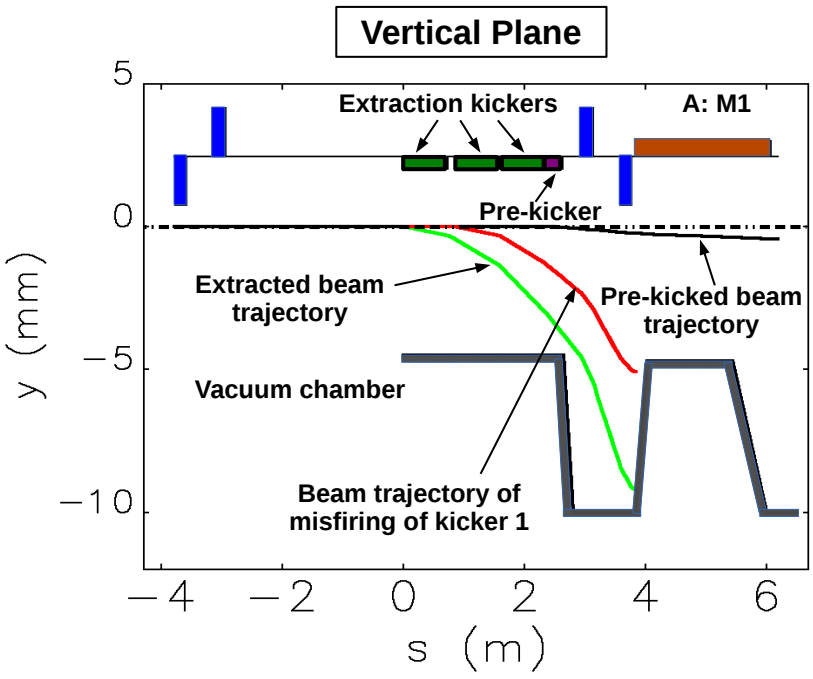

Figure 2.21. Layout of swap-out extraction section and dumping beam trajectory at different scenario.

2. Machine protection — sudden loss of beam, e.g., from a swap-out extraction or from a whole beam dump, must be managed in such a way that machine components are not damaged. This is a particular concern given the energy density in the electron beam.
3. Insertion device (ID) protection — particle loss at the location of permanent-magnet IDs in particular should be kept as low as possible to reduce demagnetization.

The dump and collimation system is designed with consideration of the existing APS tunnel shielding structure, which has a thicker continuous shielding wall in Zone F (see section 2-3.13.4), extending from sector 37 to sector 1. These are preferred sectors for collimators and beam dumps. In sector 1, any such objects should ideally be in the upstream, "A," part of the sector, since the shield wall becomes thinner around the location of the S02A:M2 dipole.

Both horizontal and vertical collimators are used in this system. Their physical apertures were introduced in **??**, where they are included in simulations of single-particle dynamics. What follows is a more detailed description

1. Whole-beam dump/Horizontal collimators: This is for machine protection. When an error is detected, e.g., mis-steering of an x-ray beam from an undulator that could result in damage to a vacuum chamber, it is necessary to dump the entire beam. This will be performed by tripping both rf systems. Simulation shows that the dumped beam power density is so high that it will carve a groove in any kind of material. To prevent damage to other components, such losses are localized to a set of horizontal dumps located on upstream side of the A:Q4

Table 2.23. Errors used in simulations of injection efficiency. All errors are gaussian with 2-σ cutoff. Rf phase errors and stripline timing jitter are modeled as timing shifts relative to a common clock.

Quantity	Value	Units
Booster orbit	100	μm
Booster orbit	$100/\beta$	μrad
Booster energy	0.1	%
Booster phase	50	ps
Booster septum amplitude	0.01	%
BTS quadrupole strength	0.55	%
SR Lambertson septum amplitude	0.01	%
Stripline kicker amplitude	0.2	%
Stripline kicker timing	100	ps
SR phase	50	ps

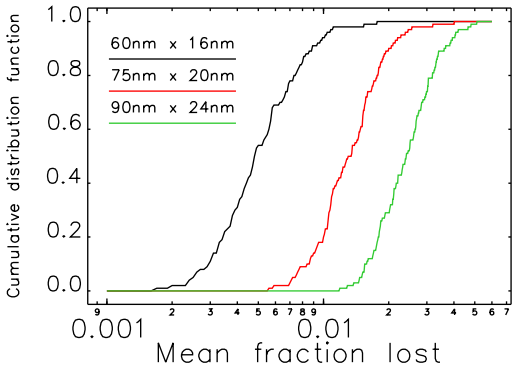

Figure 2.22. Cumulative distribution of fraction of injected particles that are lost, for various assumptions of horizontal and vertical emittance of the injected beam.

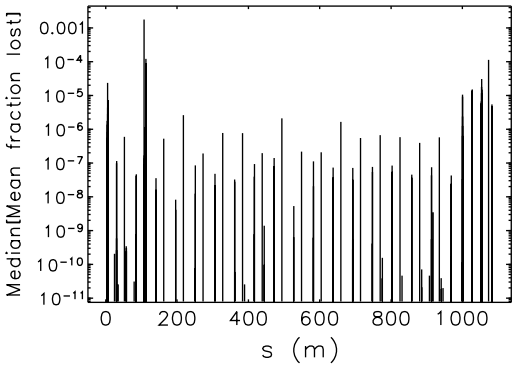

Figure 2.23. Locations of injection losses for the nominal 60nm by 16nm injected beam emittances.

magnets in sectors 37, 38, 39, 40, and 1. These dumps, which have a nominally ±4.8-mm horizontal aperture, are near the point of maximum horizontal beta and dispersion function. Multiple dumps are used, thus covering a spread in betatron phase angles, to make sure that beams can be always dumped to at least one of these specially-designed components even when including other machine errors. Another feature of these horizontal collimators is that the collimating surface should be vertically movable to provide a fresh surface after a dump. The nominal aperture of the dumps/collimators was chosen to avoid reducing the maximum-achievable Touschek lifetime while still intercepting most Touschek-scattered particles. The beam stay clear (BSC) aperture, defined by a free betatron oscillation, is limited by the smallest ID aperture in sector 4 (HSCU). Installation of beam collimators in the BTS line is under consideration.

2. Swap-out beam dump/Vertical collimators: Bunches that are extracted as part of swap out are directed to this dump. As described in 2-2.8.2, the swap-out bunch is kicked first by a

weak stripline kicker (pre-kicker), after which there is a delay of about 250 turns to allow decoherence, which reduces the energy density by two orders of magnitude. Following this, another three stripline kickers are fired to dump the bunch vertically and without damage to the dump itself. Physically, the swap-out beam dump is a ±4.58-mm vertical collimator located inside the A:M1 magnet in sector 39. This location not only has large vertical beta function, but also benefits from extra shielding provided by the magnet. A vertical collimator of the same design is installed in sector 1. This one is intended to localize the incoming injected beam loss which could come from either a larger-than-normal injected beam trajectory jitter or a misfiring of injection kicker. The BSC aperture in vertical plane is limited by this swap-out beam dump and vertical collimator aperture size.

The BSC aperture over one sector is shown in Fig. 2.24.

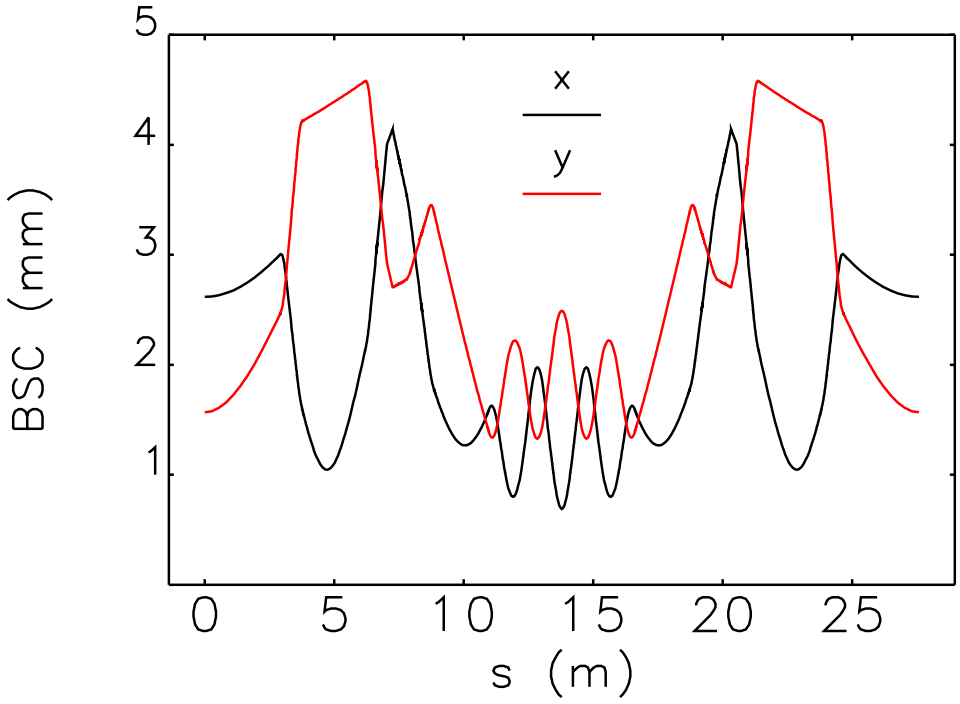

Figure 2.24. The BSC aperture over a sector. The horizontal aperture is limited by the smallest ID aperture; The vertical aperture is limited by the vertical collimator aperture.

2-2.9.1 Collimation of Touschek Losses

As described above, collimators are also used to catch the lost particles from injection, Touschek scattering, and gas scattering. Simulations of injection were described in 2-2.8.3; the corresponding loss distribution is shown in Fig. 2.23.

The Touschek beam loss distribution was also simulated, using a Monte Carlo approach that directly models the scattering [39, 94]. Using the apertures described just above (and in **??**), the loss

distribution was obtained for several cases of errors (also described in **??**).

In particular, the Touschek beam loss simulation was performed using five optical errors from one hundred optical error ensembles. These reflect the minimum, next-to-minimum, average, next-to-average, and maximum calculated Touschek beam lifetime. The beam parameters used for simulation are: $\varepsilon_{x,y}$ = 34-pm, σ_t = 100-ps, σ_δ = 0.16%, approximately representing a 48-bunch fill with HHC, IBS, and an emittance ratio of $\sim$ 1 (see Table **??**). Beam lifetime from Monte Carlo simulation is compared with the one calculated directly from Piwinski's formula, results are shown in Table 2.24. One can see that except for the case of average lifetime (the difference is $\sim$20%), all other cases have a very good agreement. The Piwinski's formula only gives beam lifetime, while the Monte Carlo simulation can provide beam loss distribution information for the radiation shielding study. Table 2.25 summarizes the loss distribution results.

The ID losses are mostly confined to the gap ID in sector 4 (SCAPE), which is a superconducting ID and is less sensitive to radiation damage than permanent magnet IDs. The total average power loss at ID4 is 0.01W, which is very small. The results for the minimum, average, and maximum-lifetime case are shown in Fig. 2.25.

Table 2.24. Comparision of simulated Touschek beam lifetime

Case	Lifetime from Piwinski's formula h	Lifetime from Monte Carlo simulation h
Minimum lifetime	3.38	3.33
Next-to-minimum lifetime	3.52	3.72
Average lifetime	4.11	5.01
Next-to-average lifetime	4.07	4.55
Maximum lifetime	5.82	5.98

Table 2.25. Summary of Touschek beam loss distribution

Case	ID loss % of total	Septum loss % of total	Collimator loss % of total	Other locations % of total
Minimum lifetime	4.3	1.3	83.0	11.4
Next-to-minimum lifetime	2.2	1.6	87.7	8.5
Average lifetime	6.7	1.3	79.8	12.2
Next-to-average lifetime	2.9	1.1	84.9	11.1
Maximum lifetime	2.7	0.7	81.9	14.7

These results and those from injection modeling show that the collimation scheme works as expected for localizing the Touschek beam loss but is less effective for the injected beam loss. This is owing to the fact that the injected beam losses mostly result from larger betatron oscillation, rather than energy oscillation. Combined with the presence of small aperture ID4, this makes collimation of the injected losses difficult. Further studies are planned of the Touschek collimation scheme, including the optimimum collimator aperture.

Gas scattering was also simulated, including elastic and inelastic scattering. These simulations [40,

41] give the lifetime as well as the loss distributions, and are described in Section 2-2.7.2.

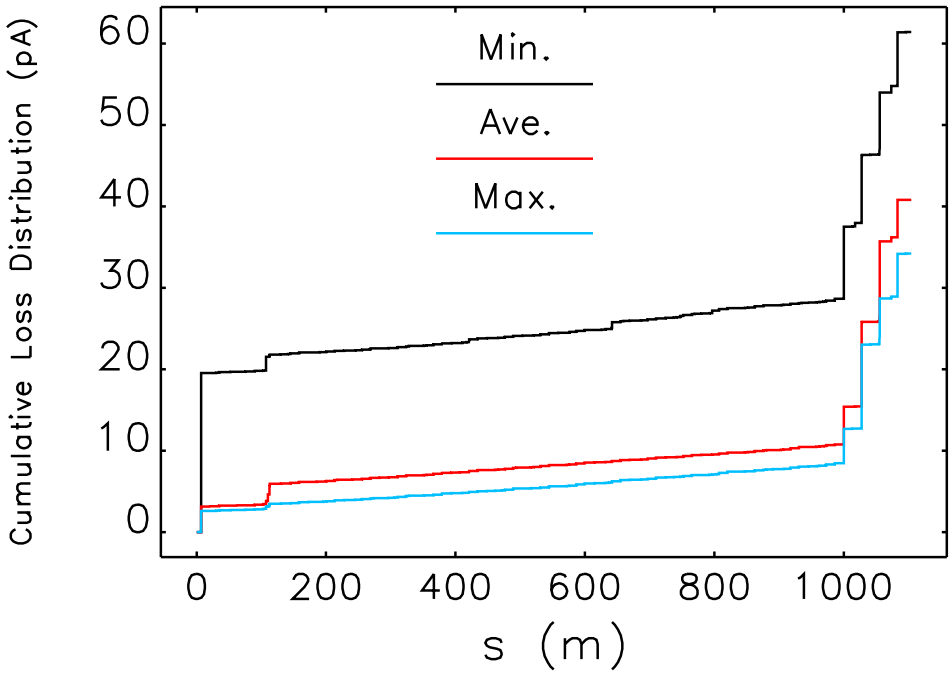

Figure 2.25. Cumulative loss distributions for the minimum, average, and maximum-lifetime simulated cases.

2-2.9.2 Energy Deposition Simulations

At 7 GeV and 100 mA, the present APS SR beam is capable of damaging materials it intercepts, in spite of having $\sigma_x = 280$ μm and $\sigma_y = 10$ μm. This was seen experimentally for both copper and tungsten [95]. For APS-U, `elegant` simulations predict much smaller rms beam footprint sizes on the swap-out and whole-beam dumps. Hence, it is important to carefully consider both the material and strategy for the beam dumps for the APS-U, in order to prevent damage to the vacuum chamber. Energy deposition was examined using `elegant` to simulate the particle distribution on the dump and using MARS [96, 97, 98] to simulate matter-particle interaction.

The MARS simulations provide the dose D, in Gy or J/kg, imparted to the material. A naive estimate of peak temperature excursion can be determined as,

$$\Delta \mathrm{T} = \frac{D A_w}{C_m}, \tag{2.4}$$

where A_w the atomic weight and C_m the molar specific heat. Peak dose and temperature rise for operational swap-out beam dumps without transverse beam size modification is listed in Table 2.26. In reality, C_m varies with temperature [99]; also for large dose, enthalpy associated with phase changes must be included. MARS includes the effect of temperature-dependent specific heat [100];

however, the temperature excursion must be below the melting point. For ΔT above phase transition temperatures, energy deposition output from MARS are used as input to separate analyses.

Also ignored in this equation is the effect of thermal diffusion [101, 102], which can reduce the

Table 2.26. Peak dose in candidate collimator material for a single, unmodified swapped-out bunch out of 48

Material	Dose (MGy)	C_m (Jmole^{-1}K^{-1})	A_w (g mole^{-1})	ΔT (K)	Melting Temp. (K)
Graphite	2.115	8.52	12.01	2980	3915*
Aluminum	2.001	24.2	26.98	2230	933
Titanium alloy	1.881	25.06	47.87†	3510	1900-1950
Copper	1.901	24.44	63.55	4940	1358
Tungsten	2.338	24.27	183.84	1.77×10^4	3695

*sublimation
†Ti only

temperature rise in the whole-beam dump over the $\sim 10\mu$s required for the beam to be lost.

Regardless of these reservations, empirically it is found that when Eq. 2.4 predicts ΔT to exceed the melting temperature for a given material, that material will suffer damage. Examples in the present APS SR of materials damaged by beam dumps include copper and tungsten; however, aluminum components exposed to the beam have never shown beam-induced failure. In the former case, the melting temperatures were exceeded according to Eq. 2.4; whereas, in the latter it was not. Because of the very high energy densities of the APS-U beam, the collisional (local heating) component [103] is appears sufficient to damage essentially any commonly-used metal.

2-2.9.3 Swap-out Beam Dump

`elegant` simulations predict rms beam sizes at the swap-out dump to be $\sigma_x = 6$ μm and $\sigma_y = 25$ μm. This implies very high power densities within the electron beam. The transverse distribution is read into MARS from output of the `elegant` simulations. Simulations typically employed 10^6 trajectories to model the initial electron distribution. The maximum dose is obtained for several candidate materials including graphite, aluminum, and titanium alloy TiAl6V4 (TiA) containing by weight 6 percent Al and 4 percent V.

As described in 2-2.8.2, if the swap-out bunch is kicked first by a weak stripline kicker (pre-kicker), then only dumped after a delay of about 250 turns to allow decoherence, there is a significant reduction in the energy density, which allows the bunch to be removed without damaging the dump. MARS predicts peak ΔT values of 16.8K,11.9K, 19.4K, 44.8K, and 269K in graphite, aluminum, TiA, copper, and tungsten, respectively. The peak temperature excursions after decoherence show a large reduction compared with those prior to decoherence listed in Table 2.26.

2-2.9.4 Whole-beam dump

As the name suggests, the whole-beam dump is intended as the location where the entire beam can be aborted at once. In APS-U, the horizontal Touschek collimators will be used as whole-beam dumps, due to the beneficial lattice functions at those locations. This will happen, for example,

when the rf systems are tripped under the command of the machine protection system or personnel protection system.

Based on the above analysis, there is good reason to expect that the whole-beam dump might be damaged by the beam. To assess this possibility, beam abort simulations were performed for 48-bunch mode with $\Delta f_h = 9$kHz, using 10,000 particles per bunch. The collimation configuration was slighlty different from the more recent concept described above, in terms of the exact position and aperture of the dump. Tracking was performed for 10,000 turns to find the equilibrium using a lumped-element model, including lumped-element impedances, main and harmonic rf, and feedback systems. After turn 10,000, the simulation switched to an element-by-element model [104] including element-by-element synchrotron radiation, transverse and longitudinal impedance, main and harmonic rf systems, and physical apertures. Shortly after this, the generator for the main rf cavities was muted and the cavities began to ring down. The transverse and longitudinal feedback systems were simultaneously switched off so they do not fight the decay of the beam energy.

Figures 2.26 and 2.27 show properties of bunch 0 starting just after the switch to element-by-element tracking. The decay of the momentum centroid begins at pass 2 when the rf drive is muted. The beam sizes do not change much until the beam actually begins to be lost. This implies high particle density on any surface struck by the beam.

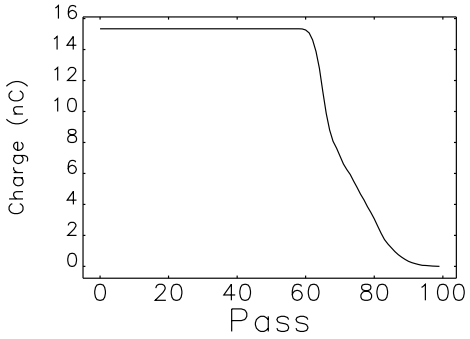

Figure 2.26. Charge in bunch 0 vs. pass, where the rf is muted at pass 2.

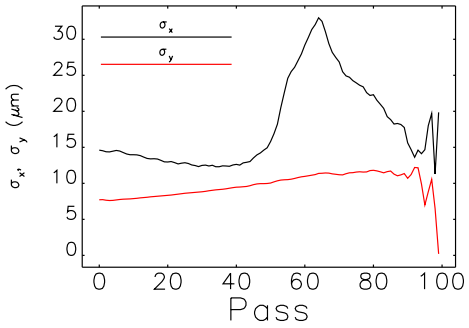

Figure 2.27. Horizontal and vertical beam size of bunch 0 at the end of sector 40 vs. pass, where the rf is muted at pass 2. Note that the beam sizes at the dump are different due to different lattice functions.

The collimation in the beam tracking simulations is idealized and does not include out-scatter or shower generation. However, it accurately reflects the distribution of the beam when it first impacts the dump. All of the lost electrons first strike this dump, making this a worst-case scenario. Inspection of Fig. 2.26 shows that 50% of the beam is dumped within 10 turns.

As was the case for the swap-out dump, the loss distribution from these tracking simulations is used as input for MARS simulations. An anamorphic x-z view of the MARS beam dump geometry at beam elevation is presented in Fig. 2.28. The vacuum beam pipe is composed of aluminum with an ID of 22 mm and an OD of 24.54 mm. Within the beam pipe, the collimator is modeled as the section of a cylinder with a 0.865-m radius. The chord length of the cylinder is 20 cm at beam elevation. A 1-cm thick disk of iron at the downstream end of the geometry represents the AQ4

magnet. A normal perspective x-y view of the beam dump geometry at the collimator apex is given in Fig. 2.29. During a beam dump, the electron beam strikes the collimator on the inboard side.

Based on experience in the present APS SR, we expect a whole beam loss event in the APS-U ring (for which there is no decoherence) will lead to localized mechanical damage of the dump in the form of a groove carved by the beam. The energy density in the APS-U beam is much higher than for the present SR, indicating the collimator will experience localized melting or vaporization, particularly if materials of higher density and atomic number are used. A trade-off exists between the desire to stop the dumped beam quickly and the amount of damage that the dump will sustain. MARS simulations strongly suggest that aluminum is the best material for the beam dump for several reasons that are discussed below. Highly anamorphic views of the electron/positron fluence

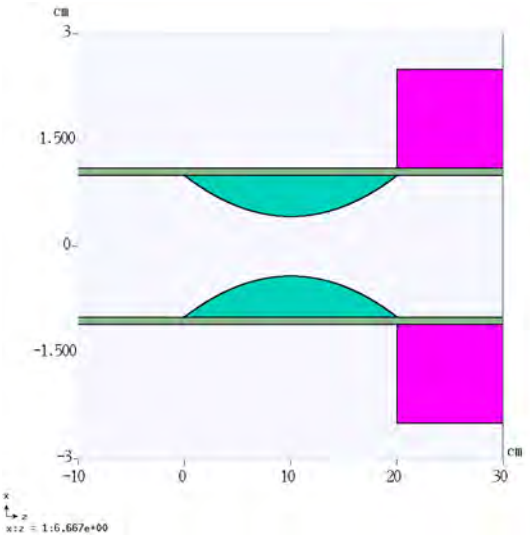

Figure 2.28. Anamorphic X-Z view of the beam dump geometry at beam elevation.

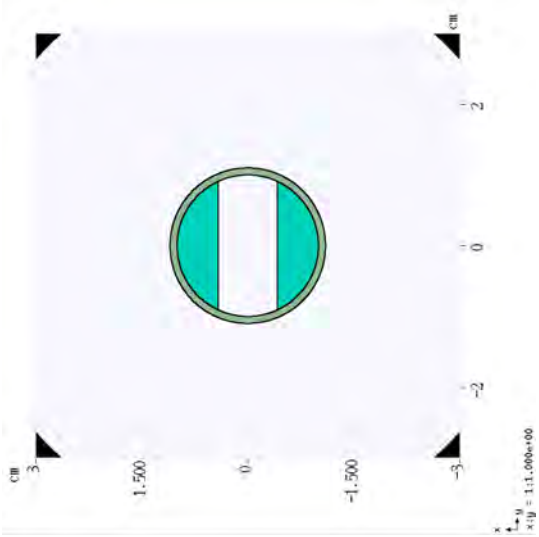

Figure 2.29. Normal X-Y view of the beam dump geometry at the H-collimator apex.

(cm^2), as well as total dose (Gy) are shown in Figs. 2.30 and 2.31 for aluminum.

Based on APS experience, doses causing estimated temperature excursions in excess of the melting temperature can lead to localized mechanical damage. In aluminum, a dose of 1 MGy leads to a temperature excursion of approximately 1000K according to Eq. 2.4, well in excess of the melting point of 933K. Thus, regions where dose exceeds 1 MGy are expected to exhibit mechanical damage in aluminum. In the present APS ring, modeling beam dumps on aluminum vacuum chamber components yield temperature excursions just below the melting point [105]. Beam-strike damage has not been observed on any aluminum vacuum surface in the present ring. A 1-MGy rule-of-thumb is roughly an order of magnitude less than the hydrodynamic regime threshold of 15 MGy [106, 107]. All materials modeled (including graphite) exhibit a peak dose of approximately 20 MGy.

Simulations also show that most of the energy in the beam exits the dump. In particular, of the 4600 J in the beam, only 23 J are predicted to be deposited in an Al dump; for Cu and W dumps, the numbers are 260 J and 410 J, respectively. However, the fluence results, Figs. 2.30 and **??**, show that the beam is significantly broadened in the transverse plane. Hence, the dump acts more like a spoiler, particularly in the case of Al.

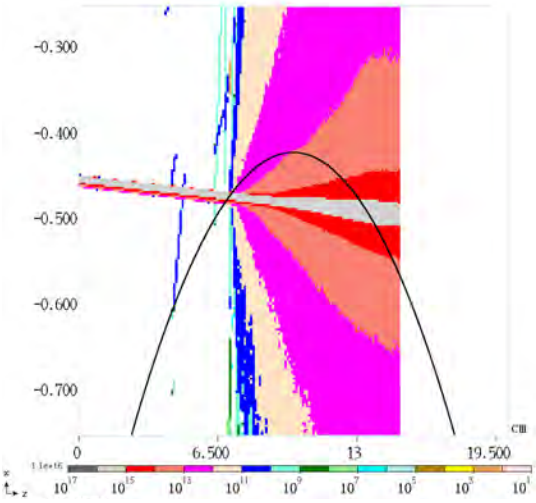

Figure 2.30. Electron-positron fluence from a whole beam dump in Al ($10^{15}cm^{-2}$).

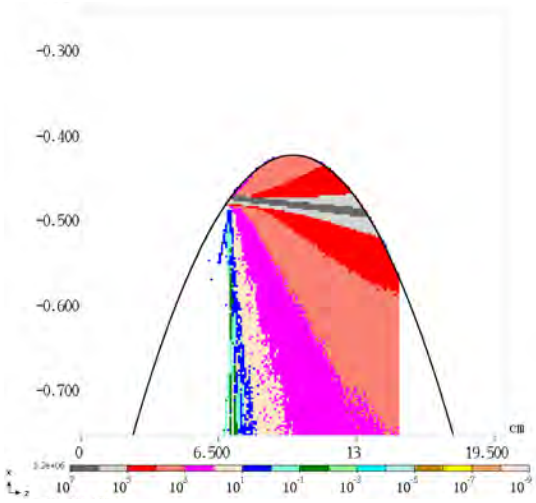

Figure 2.31. Total dose distribution in Al integrated over y.

While copper, titanium, and tungsten all absorb more energy locally, based on the downstream shower and dose patterns, aluminum appears to be the best choice for the beam dump. The radiation length in aluminum (X_o/ρ) is 8.9 cm, making the axial extent 1.0 X_o. The dump length is sufficient to scatter the beam while minimizing the absorbed energy and thus damage to the wall. Maximum dose in the magnet iron and the adjacent beam pipe are presented in Table 2.27; ΔT calculated from Eq 2.4 are also given. As seen in the table, the temperature excursions are relatively small. Because vaporized material from the dump is likely to settle on nearby vacuum chamber walls, it makes the most sense for these materials to be the same.

Table 2.27. Whole-beam peak dose in magnet iron and adjacent beam pipe.

Dump Material	Wall Dose (kGy)	Fe Dose (kGy)	ΔT Wall (K)	ΔT Fe (K)
Al	0.7	0.65	0.78	1.4
TiA	2.0	2.0	2.2	4.4
Cu	1.7	2.2	1.9	4.9
W	1.4	1.5	1.6	3.3

With an aluminum dump, the downstream profiles indicate the FWHM extent of the shower is 1.1 mm in x and 0.9 mm in y. The cross sectional area of the shower is now roughly equivalent to that of the decohered swap-out bunch. As mentioned, further simulations will be needed to assess possible damage to materials elsewhere in the ring. Another advantage of an Al dump is the reduction the neutron dose. At the dump, local maximum neutron fluence levels drop from 6.6×10^{12}cm^{-2} with W to 2.3×10^{11}cm^{-2} for Al.

As discussed above, simulations indicate the beam dump will be damaged after every whole-beam loss event; therefore, the present plan is to have the dump move after each event to expose an undamaged surface at the probable strike location. The motion will most likely be translational in the vertical direction.

An important point to keep in mind is that the MARS model is static; however, if material in the beam dump is heated sufficiently, the material may enter a hydrodynamic regime and move over the course of the dump. Such motion may lead to a change in the dump mechanical configuration and downstream dose distributions. For example, losses may then be spread over several of the dumps (a total of five are presently included).

2-2.10 Ray Tracing Guidelines

Ray tracing is used to identify direct line-of-sight from dipole radiation source points to accelerator components such as photon absorbers, vacuum chamber walls, flanges, bellow liners, and gate valves. Accelerator components must be designed to tolerate the heating from intercepted radiation. To be conservative, a hard-edge model is assumed for the dipole field; this overestimates the intercepted power for the inboard edge of the ray. Standard ray tracing typically only concerns the horizontal plane and horizontal orbit errors; that is, only the in-plane synchrotron radiation produced in the dipole fields is traced. Given the strong dipole fields and small vacuum chamber apertures in the upgrade machine, the out-of-plane radiation is also potentially an important source of heating, especially for non-ideal orbits. For the APS Upgrade, 2D (x,s) ray tracing and 3D (x,y,s) photon tracking have been carried out for a beam orbit centered in the magnets (see section **??**, Figure **??**). The next step is to include realistic orbit errors.

The most probable source of a large orbit perturbation is a single-source orbit distortion caused by a single dipole kick at one location in the ring. This could be caused by a magnet power supply trip, mistakenly changed magnet setting, or a poorly-compensated local steering bump elsewhere in the machine. Misdirected insertion device beams are limited by using interlocked beam position monitors located at opposite ends of each insertion device straight section, the so-called beam position limit detectors (BPLDs). Selected BPMs in the arcs between insertion devices will also be interlocked to control dipole sources. These devices, distributed around the ring, also serve as an interlock on the global orbit distortion. When the global orbit becomes large enough, the beam will be lost on an aperture limitation (it could be a real aperture limit or a BPLD interlock limit). The physical aperture limitations are obviously larger than BPLD interlock limits, therefore the physical aperture limitations are considered first.

All possible orbits that can exist within the APS-U aperture were generated and phase space diagrams covering all possible orbits were plotted at the exit of all bending magnets [108]. Betatron ellipse constants $\mathcal{A} = \gamma x^2 + 2\alpha x x' + \beta x'^2$ for ellipses that encompass all possible trajectories at the bending magnet exists are calculated in [108] and can be used for ray tracing. The maximum orbit can be limited to much smaller values by the BPLDs, so that the orbit phase space at the relevant amplitudes is close to undistorted betatron ellipses. Since insertion device (ID) BPLDs are located all around the ring and at the same beta function, one can write for the limiting ellipse:

$$\mathcal{A} = \frac{x_{\mathrm{BPLD}}^2}{\beta_{\mathrm{BPLD}}}, \tag{2.5}$$

where x_{BPLD} and β_{BPLD} are the BPLD trip limit and the beta function at the BPLD location, respectively. For example, if the BPLD trip limit is 1 mm and the beta function is 6 m, the ellipse constant is $\mathcal{A} = 0.17\mu$m. In this way, ID BPLDs can provide protection against orbit distortion elsewhere.

It is important to emphasize that the consideration above only refers to a single-source orbit distortion. Deliberate steering inside a dipole magnet can generate larger orbits, which can be protected against by BPLDs near these magnets. It is planned to allow all BPMs to be incorporated into the BPLD system.

References

[1] Thomas E. Fornek et al. *Preliminary Design Report for the APS Upgrade Project*. Tech. rep. APSU-2.01-RPT-002. APS, 2017 (cit. on pp. 5, 10–12, 14, 15, 22, 23, 28–30, 36).

[2] Michael Borland, Argonne National Laboratory, unpublished information, 2018 (cit. on pp. 5, 6, 35).

[3] Yipeng Sun, Michael Borland, and Ryan Lindberg, Argonne National Laboratory, unpublished information, 2018 (cit. on p. 5).

[4] Vadim Sajaev et al., Argonne National Laboratory, unpublished information, 2018 (cit. on pp. 5, 15).

[5] Michael Borland et al., Argonne National Laboratory, unpublished information, 2018 (cit. on pp. 5, 15, 29).

[6] Ryan Lindberg, Argonne National Laboratory, unpublished information, 2018 (cit. on pp. 5, 29).

[7] Aimin Xiao and Michael Borland, Argonne National Laboratory, unpublished information, 2018 (cit. on pp. 5, 15).

[8] Jeffrey Dooling and Michael Borland, Argonne National Laboratory, unpublished information, 2018 (cit. on p. 5).

[9] Y.-P. Sun and M. Borland. "Alternate Lattice Design for Advanced Photon Source Multi-Bend Achromat Upgrade." In: *Proc. IPAC15*. TUPJE071 (cit. on p. 5).

[10] L. Farvacque et al. "A Low-emittance Lattice for the ESRF." In: *Proc. of 2013 PAC*. 2013, p. 79 (cit. on p. 5).

[11] J. Delahaye and J. P. Potier. "Reverse bending magnets in a combined-function lattice for the CLIC damping ring." In: *Proc. PAC89*. 1990, pp. 1611–1613 (cit. on p. 5).

[12] A. Streun. "The anti-bend cell for ultralow emittance storage ring lattices." In: *NIM A* 737 (2014), pp. 148–154 (cit. on p. 5).

[13] M. Borland et al. "Lower Emittance Lattice for the Advanced Photon Source Upgrade Using Reverse Bending Magnets." In: *these proceedings*. WEPOB01 (cit. on p. 5).

[14] M. Borland et al. "Hybrid Seven-Bend-Achromat Lattice for the Advanced Photon Source Upgrade." In: *Proc. IPAC15*. 2015, pp. 1776–1779 (cit. on p. 5).

[15] M. Borland et al. "Hybrid Seven-Bend-Achromat Lattice for the Advanced Photon Source Upgrade." In: *Proc. IPAC15*. 2015, pp. 1776–1779 (cit. on p. 5).

[16] M. Borland., Argonne National Laboratory, unpublished information, 2018 (cit. on p. 6).

[17] M. Borland et al. *Multi-objective Direct Optimization of Dynamic Acceptance and Lifetime for Potential Upgrades of the Advanced Photon Source*. Tech. rep. ANL/APS/LS-319. APS, 2010 (cit. on p. 6).

[18] K. Deb et al. In: *IEEE TEC* 6 (2002), p. 182 (cit. on p. 6).

[19] I. Bazarov and C. Sinclair. "Multivariate optimization of a high brightness dc gun photoinjector." In: *Phys. Rev. ST Accel. Beams* 8 (2005), p. 034202 (cit. on p. 6).

[20] Yipeng Sun and Michael Borland, Argonne National Laboratory, unpublished information, 2017 (cit. on p. 7).

[21] C. Yao X. Sun. "Simulation Studies of a Prototype Stripline Kicker for the Aps-Mba Upgrade." In: *NAPAC16*. WEPOB14. 2016 (cit. on p. 7).

[22] V. Sajaev, Argonne National Laboratory, unpublished information, 2014 (cit. on p. 8).

[23] V. Sajaev, Argonne National Laboratory, unpublished information, 2017 (cit. on pp. 9, 11).

[24] V. Sajaev et al. "Determination of the ground motion orbit amplification factors dependence on the frequency for the APS Upgrade storage ring." In: *Proc. IPAC18*. 2018, pp. 1272–1274 (cit. on p. 10).

[25] V. Sajaev, Argonne National Laboratory, unpublished information, 2015 (cit. on p. 10).

[26] Louis Emery, Argonne National Laboratory, unpublished information, 2017 (cit. on p. 10).

[27] V. Sajaev, Argonne National Laboratory, unpublished information, 2016 (cit. on p. 12).

[28] V. Sajaev, Argonne National Laboratory, unpublished information, 2017 (cit. on p. 12).

[29] Vadim Sajaev, Argonne National Laboratory, unpublished information, 2017 (cit. on p 12).

[30] V. Sajaev. "Commissioning simulations for the Argonne Advanced Photon Source upgrade lattice." In: *Phys. Rev. Accel. Beams* 22 (2019), p. 040102 (cit. on p. 13).

[31] V. Sajaev and M. Borland. "Commissioning Simulations for the APS Upgrade Lattice." In: *Proceedings of IPAC15*. 2015, p. 553 (cit. on p. 15).

[32] Kazuhito Ohmi, Kohji Hirata, and Katsunobu Oide. "From the beam-envelope matrix to synchrotron-radiation integrals." In: *Phys. Rev. E* 49 (1 Jan. 1994), pp. 751–765. DOI: 10.1103/PhysRevE.49.751. URL: https://link.aps.org/doi/10.1103/PhysRevE.49.751 (cit. on p. 15).

[33] M. Borland, Argonne National Laboratory, unpublished information, 2008 (cit. on p. 15).

[34] M. Borland, Argonne National Laboratory, unpublished information, 2017 (cit. on pp. 15, 35).

[35] A. Xiao and M. Borland. "Intrabeam scattering effect calculated for a non-gaussian-distributed linac beam." In: *Proc. of PAC 2009*. 2009, pp. 3281–3283 (cit. on pp. 15, 29).

[36] A. Xiao and M. Borland. "Intra-beam and Touschek scattering computations for beam with non-gaussian longitudinal distributions." In: *Proc. of IPAC 2015*. 2015, pp. 559–561 (cit. on pp. 15, 29).

[37] A. Irwinski. *The Touschek Effect in Strong Focusing Storage Rings*. DESY 98-179. DESY, 1998 (cit. on pp. 15, 29).

[38] S. Khan. "Simulation of the Touschek effect for BESSY II: A Monte Carlo Approach." In: *Proc. of EPAC 1994*. 1994, pp. 1102–1104 (cit. on p. 15).

[39] A. Xiao and M. Borland. "Monte Carlo simulation of Touschek effect." In: *Phys. Rev. ST Accel. Beams* 13 (2010), p. 074201 (cit. on pp. 15, 39).

[40] M. Borland, Argonne National Laboratory, unpublished information, 2017 (cit. on pp. 15, 30, 40).

[41] M. Borland, Argonne National Laboratory, unpublished information, 2017 (cit. on pp. 15, 30, 41).

[42] Y. Chae. "Impedance Database and Its Application to the APS Storage Ring." In: *Proc.of PAC 2003*. 2003, pp. 3017–3019 (cit. on p. 17).

[43] Y. Chae and Y. Wang. "Impedance Database II for the Advanced Photon Source Storage Ring." In: *Proc. of PAC 2007*. 2007, pp. 4336–4338 (cit. on p. 17).

[44] Y. Chae. "The Impedance Database Computation and Prediction of Single Bunch Instabilities." In: *Proc.of PAC 2007*. Invited Talk. 2007 (cit. on p. 17).

[45] R.R. Lindberg and A. Blednykh. "Instability thresholds for the Advanced Photon Source multi-bend achromat upgrade." In: *Proc. of IPAC 2015*. 1822, p. 1882 (cit. on p. 17).

[46] W. Bruns. *The GdfidL Electromagnetic Field simulator*. URL: http://www.gdfidl.de (cit. on p. 17).

[47] I. A. Zagorodnov and T. Weiland. "Field Solver for Particle Beam Simulations without Numerical Cherenkov Radiation." In: *Phys. Rev. ST Accel. Beams* 8 (2005), p. 042001 (cit. on p. 17).

[48] R. Lindberg. *Accurate impedance modeling*. talk at the 2018 Workshop on Diffraction Limited Storage Rings. https://sites.google.com/lbl.gov/als-dlsr2018-workshop/home (cit. on p. 17).

[49] M. Borland. *elegant: A Flexible SDDS-Compliant Code for Accelerator Simulation*. Tech. rep. ANL/APS LS-287. Advanced Photon Source, Sept. 2000. URL: http://www.aps.anl.gov/Science/Publications/lsnotes/ls287.pdf (cit. on p. 19).

[50] M. Borland et al. "Simultaneous Simulation of Multi-Particle and Multi-Bunch Collective Effects for the APS Ultra-Low Emittance Upgrade." In: *Proceedings of the 2015 International Computational Accelertor Physics Conference*. 2015, pp. 61–65 (cit. on pp. 20, 22).

[51] R. R. Lindberg, M. Borland, and A. Blednykh. "Collective Effects at Injection for the APS-U MBA Lattice." In: *Proc.of N-PAC 2016*. 2016 (cit. on pp. 20, 21).

[52] R. Lindberg and A. Blednykh., Argonne National Laboratory, unpublished information, 2019 (cit. on p. 21).

[53] M. Sangroula et al. "Measuring the coupling impedance of vacuum components for the APS Upgrade using a Goubau line." In: *Proceedings of the 2017 International Particle Accelerator Conference*. 2017, p. 3583 (cit. on pp. 21, 22).

[54] G. Goubau. "Surface Waves and their Application to Transmission Lines." In: *J. Appl. Phys.* 21 (1950), p. 1119 (cit. on p. 22).

[55] J. Musson and S. Rubin K. Cole and. "Application of Goubau Surface Wave Transmission Line for Improved Bench Testing of Diagnostic Beamline Elements." In: *Proc.of PAC 2009*. 2009, p. 4060 (cit. on p. 22).

[56] M. Sangroula et al. "Measuring the coupling impedance of vacuum components for the APS Upgrade using a Goubau line." In: *Proceedings of the 2018 International Particle Accelerator Conference*. 2018, p. 3211 (cit. on p. 22).

[57] Louis Emery, Argonne National Laboratory, unpublished information, 2018 (cit. on p. 24).

[58] Louis Emery, Argonne National Laboratory, unpublished information, 2018 (cit. on pp. 24, 25).

[59] R. Siemann. "Instability Growth Rate Calculations for High Energy Storage Rings." In: *IEEE Transactions on Nuclear Science*. Vol. NS-28. 3. Proceedings of the 1981 PAC. June 1981, pp. 2437–2439. URL: http://cern.ch/AccelConf/p81/PDF/PAC1981_2437.PDF (cit. on p. 24).

[60] J. Hagel and B. Zotter. "PC-BBI, a Program to compute Bunched Beam Instabilites on a PC." In: *Proc. of EPAC 1990*. 1990, p. 1717. URL: http://accelconf.web.cern.ch/AccelConf/e90/PDF/EPAC1990_1717.PDF (cit. on p. 24).

[61] K. Thompson and R. D. Ruth. "Transverse coupled bunch instabilities in damping rings of high-energy linear colliders." In: *Phys. Rev.* D43 (1991), pp. 3049–3062. DOI: 10.1103/PhysRevD.43.3049 (cit. on p. 24).

[62] L. Emery. *User's Guide to Program clinchor*. http://www.aps.anl.gov/Accelerator_Systems_Division/Operations_Analysis/manuals/clinchor_V1.0/clinchor.html (cit. on p. 24).

[63] L. Emery. "Required Cavity HOM DeQing Calculated from Probability Estimates of Coupled Bunch Instabilities in the APS Ring." In: *Proc. of PAC'93*. Washington DC, May 1993, p. 3360. URL: http://accelconf.web.cern.ch/AccelConf/p93/PDF/PAC1993_3360.PDF (cit. on p. 24).

[64] Ryan R. Lindberg. "Theory of coupled-bunch longitudinal instabilities in a storage ring for arbitrary rf potentials." In: *Phys. Rev. Accel. Beams* 21 (12 Dec. 2018), p. 124402. DOI: 10.1103/PhysRevAccelBeams.21.124402. URL: https://link.aps.org/doi/10.1103/PhysRevAccelBeams.21.124402 (cit. on p. 24).

[65] D. Teytelman and J.M. Byrd. *APS-U Longitudinal Feedback Design Study*. Tech. rep. San Jose, California: Dimtel, Inc., Mar. 2017 (cit. on p. 25).

[66] https://www.dimtel.com/products/igp12 (cit. on p. 25).

[67] Y. Wang and M. Borland. "Pelegant: A Parallel Accelerator Simulation Code for Electron Generation and Tracking." In: *AIP Conf. Proc.* 877 (2006), p. 241 (cit. on p. 25).

[68] Michael Borland and Louis Emery, Argonne National Laboratory, unpublished information, 2018.

[69] L. Emery et al. "Multi-bunch stability analysis of the Advanced Photon Source upgrade including the higher-harmonic cavity." In: 2015, pp. 1784–1786 (cit. on p. 26).

[70] Michael Borland, Argonne National Laboratory, unpublished information, 2017 (cit. on p. 26).

[71] H.G. Hereward. *Coherent Instability due to Electrons in a Coasting Proton Beam*. Tech. rep. CERN-71-15. July 1971 (cit. on p. 27).

[72] Y. Baconnier and G. Brianti. *The Stability of Ions in Bunched Beam Machines*. Tech. rep. CERN/SPS/80-2. Mar. 1980 (cit. on p. 27).

[73] J. Calvey, Argonne National Laboratory, unpublished information, 2019 (cit. on p. 27).

[74] J.A. Carter. "Benchmarking and Calibration of Monte Carlo Vacuum Simulations with SynRad and MolFlow+." In: *Proc. of International Particle Accelerator Conference (IPAC'16), Busan, Korea, May 8-13, 2016*. (Busan, Korea). International Particle Accelerator Conference
7. doi:10.18429/JACoW-IPAC2016-THPMY018. Geneva, Switzerland: JACoW, June 2016, pp. 3695–3697. ISBN: 978-3-95450-147-2. DOI: doi:10.18429/JACoW-IPAC2016-THPMY018. URL: http://jacow.org/ipac2016/papers/thpmy018.pdf (cit. on p. 27).

[75] L. Wang et al. "Suppression of beam-ion instability in electron rings with multibunch train beam fillings." In: *Phys. Rev. ST Accel. Beams* 14 (8 Aug. 2011), p. 084401. DOI: 10.1103/PhysRevSTAB.14.084401. URL: http://link.aps.org/doi/10.1103/PhysRevSTAB.14.084401 (cit. on p. 27).

[76] J. Calvey, K. Harkay, and C.-Y. Yao. "Ion Effects in the APS Particle Accumulator Ring." In: *NAPAC16*. THPOA14. 2016 (cit. on p. 27).

[77] G.V. Stupakov and A.W. Chao. "Study of Beam Decoherence in the Presence of Head-Tail Instability Using a Two-Particle Model." In: *Proc. of PAC 1995*. 1995, pp. 3288–3290 (cit. on p. 27).

[78] M.G. Minty, A.W. Chao, and W.L. Spence. "Emittance Growth Due to Decoherence and Wakefields." In: *Proc. of PAC 1995*. 1995, pp. 3037–3039 (cit. on p. 27).

[79] C. Yao et al. "AN FPGA-BASED BUNCH-TO-BUNCH FEEDBACK SYSTEM AT THE ADVANCED PHOTON SOURCE." In: *Proc. of PAC 2007*. http://accelconf.web.cern.ch/AccelConf/p07/PAPERS/MOPAN116.PDF. 2007, p. 440 (cit. on p. 27).

[80] D. Villevald and S. Heifets. *Ion Trapping in the SLAC B-factory High Energy Ring*. Tech. rep. SLAC-TN-06-032. June 1993 (cit. on p. 27).

[81] K. L. F. Bane, K. Kubo, and P. B. Wilson. "Compensating the Unequal Bunch Spacings in the NLC Damping Rings." In: *Proc. EPAC 1996*. 1996, pp. 1111–1113 (cit. on p. 28).

[82] J. M. Byrd et al. "Transient beam loading effects in harmonic rf systems for light sources." In: *Phys. Rev. ST Accel. Beams* 5 (9 Sept. 2002), p. 092001. DOI: 10.1103/PhysRevSTAB.5.092001. URL: https://link.aps.org/doi/10.1103/PhysRevSTAB.5.092001 (cit. on p. 28).

[83] H. Wang et al. "Transient Beam Loading due to the Bunch Train Gap and its Compensation Experiments at BEPC-II and ALS." In: *Proc. IPAC 2018*. 2018, pp. 390–393 (cit. on p. 28).

[84] J. Calvey and M. Borland, Argonne National Laboratory, unpublished information, 2018 (cit. on p. 30).

[85] F. C. Porter. "Luminosity lifetime at an asymmetric e^+e^- collider." In: *NM A* 302 (1992), pp. 209–216 (cit. on p. 30).

[86] R. Abela et al. "Design Considerations for a Swiss Light Source (SLS)." In: *Proc. EPAC 1992*. 1992, p. 486 (cit. on p. 32).

[87] L. Emery and M. Borland. "Upgrade Opportunities at the Advanced Photon Source Made Possible by Top-up Operations." In: *Proc. of EPAC 2002*. 2002, pp. 218–220 (cit. on p. 32).

[88] A. Xiao, Argonne National Laboratory, unpublished information, 2017 (cit. on p. 32).

[89] A. Xiao, Argonne National Laboratory, unpublished information, 2018 (cit. on p. 32).

[90] A. Xiao, Argonne National Laboratory, unpublished information, 2018 (cit. on p. 33).

[91] A. Xiao, Argonne National Laboratory, unpublished information, 2018 (cit. on p. 34).

[92] M. Borland, Argonne National Laboratory, unpublished information, 2017 (cit. on p. 35).

[93] M. Borland, Argonne National Laboratory, unpublished information, 2019 (cit. on p. 36).

[94] A. Xiao and M. Borland. "Beam loss simulation and collimator system configurations for the Advanced Photon Source upgrade." In: *NAPAC16*. WEPOB22. 2016 (cit. on p. 39).

[95] J.C. Dooling and M. Borland, Argonne National Laboratory, unpublished information, 2011 (cit. on p. 41).

[96] N.V. Mokhov. *The Mars Code System User's Guide*. Tech. rep. Fermilab-FN-628. Fermilab, 1995. URL: https://mars.fnal.gov (cit. on p. 41).

[97] S.I. Striganov N.V. Mokhov. *MARS15 Overview*. Tech. rep. Fermilab-Conf-07/008-AD. Fermilab, 2007 (cit. on p. 41).

[98] N.V. Mokhov et al. "MARS15 code developments driven by the intensity frontier needs." In: *Prog. Nucl. Sci. Technol.* 4 (2014), pp. 496–501 (cit. on p. 41).

[99] A.-M. Zahra et al. "Heat capacities of aluminium alloys." In: *Journal of Materials Science* 30 (1995), pp. 426–436 (cit. on p. 41).

[100] N. Mokhov. *Private Communication*. Oct. 2014 (cit. on p. 41).

[101] J. Dooling R. Lindberg., Argonne National Laboratory, unpublished information, 2012 (cit. on p. 42).

[102] M. Borland, Argonne National Laboratory, unpublished information, 2019 (cit. on p. 42).

[103] *ESTAR: Stopping Powers and Ranges for Electrons*. http://physics.nist.gov/PhysRefData/Star/Text/ESTAR.html (cit. on p. 42).

[104] R. Lindberg, M. Borland, and A. Bednykh. "Collective Effects at Injection for the APS-U MBA Lattice." In: *NAPAC16*. WEPOB08. 2016 (cit. on p. 43).

[105] Jie Liu et al. "Mechanical Design and Analysis of an Electron BeamAdvanced Photon Source." In: *Proceedings of the MEDSI 2014 Conference, Melbourne, Australia-Oct 2014*. 2014, pp. 1–6 (cit. on p. 44).

[106] Nikolai V. Mokhov. "Beam-Materials Interactions." In: *Reviews of Accelerator Science and Technology* 6 (2013), pp. 275–290 (cit. on p. 44).

[107] N.V. Mokhov and F. Cerutti. "Beam-Material Interactions." In: *Proc. of the Joint International Accelerator School: Beam Loss and Accelerator Protection Newport Beach, US, 5-14 Nov 2014*. 2016, pp. 83–110 (cit. on p. 44).

[108] V. Sajaev, Argonne National Laboratory, unpublished information, 2017 (cit. on p. 46).

2-3 Implementation

2-3.1 Introduction

The APS-U storage ring has 40 sectors, each consisting of five major arc modules in addition to the insertion devices. Magnets are mounted upon three large concrete plinth / support plate assemblies (DLM-A, FODO, DLM-B) in addition to two bridge assemblies (QMQ modules) straddling between plinths. A total of thirty three arc magnets are included in each sector, including quadrupoles, sextupoles, longitudinal- and transverse-gradient dipoles, reverse bends, and eight-pole correctors (see Figure 2.32). Bending-magnet x-ray beamlines are supported with radiation from the B:M3 transverse-gradient dipole located in the FODO section.

All together, each sector contains 7 dipoles, 10 standard quadrupoles, 6 reverse bends, six sextupoles, and four fast steering correctors totalling 33 lattice magnets / sector, or 1,321 magnets for the entire 40 sectors (one extra corrector is employed near the injection point). This is in addition to insertion device sources tailored to beamline requirements.

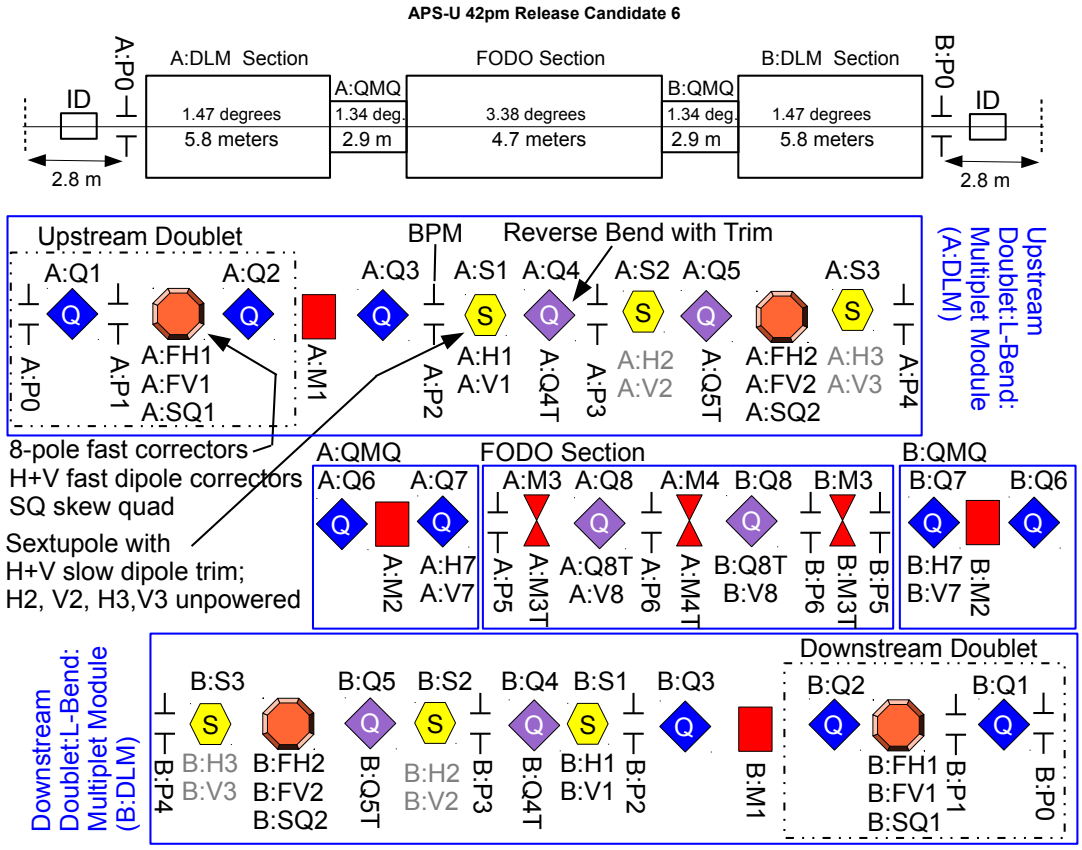

Figure 2.32. Block diagram showing major components and practical implementation for one sector of the APS-U storage ring lattice.

In addition to 35 standard MBA insertion-device straight sections, three straight sections are reserved for 12 existing rf cavities. One straight section contains fast swap-out extraction kickers and a superconducting bunch-lengthening harmonic cavity, and one contains a DC Lambertson injection

septum and three fast injection kickers.

The vacuum system is closely integrated with the magnet assemblies and generally uses non-evaporable getter (NEG)-coated cylindrical chambers with 11-mm inner radius and 1-mm wall thickness designed to satisfy impedance requirements. The minimum magnet pole tip radius is 13 mm. Uncoated aluminum antechamber-style chambers are used within the M1 and M2 longitudinal-gradient dipoles. Round inconel chambers are used in the bore of the four fast eight-pole correctors in each sector to improve response time. Beam position monitor assemblies each with four pickup electrodes and integral bellow assemblies and flanges facilitate chamber assembly. Water cooling and strategically placed discrete photon absorbers are used to handle heating from synchrotron radiation.

For fast orbit feedback (FOFB), four fast combined-function dipole correctors in each sector are used to stabilize the insertion device and bending magnet source points. Each fast corrector has windings for horizontal dipole, vertical dipole, and skew quadrupole field components. Slow dipole trim windings are included on all sextupole magnets and the FODO section quadrupoles. In addition, 14 RF electron beam position monitors (BPMs) per sector and, in sectors with beamlines, four x-ray beam position monitors are used for orbit alignment and feedback.

Power supplies are located on top of the storage ring enclosure, using existing s-shaped conduit penetrations for cabling. The majority of main magnet as well as trim and corrector windings, are powered by individual power supplies. Two families of dipoles (M1 and M2) are powered in series. Sextupoles and quadrupoles will be powered by ultrastable unipolar power supplies while correctors and trim windings will use smaller bipolar supplies. Power supplies will be monitored with a unified fast data acquisition system, integrated with the fast orbit feedback data network and accelerator timing systems.

A high-resolution absolute beam size monitor will be used to quantify the emittance. In addition, a relative beam size monitor will be used in conjunction with skew-quad windings located on the fast corrector magnets to control horizontal/vertical coupling. Additional diagnostics to monitor total beam current, bunch current, x-ray beam position and intensity are provided. Longitudinal and transverse bunch-by-bunch feedback systems will be used to control coupled-bunch instabilities. Beam position limit detector (BPLD) interlocks using BPMs to control mis-steered beams will be deployed.

An enhanced control system based on the Experimental Physics and Industrial Controls System (EPICS) will be provided, and will include high-speed data acquisition, channel- and service-oriented application programming interfaces, and instrument-embedded input-output controllers (IOCs).

To preserve beam lifetime, a superconducting harmonic cavity bunch-lengthening system will be used, which will be closely integrated with the existing rf, controls, and timing systems.

2-3.2 Magnets

Each sector has four longitudinal gradient dipoles, three transverse gradient dipoles, six reverse bend gradient dipoles, ten quadrupoles, and six sextupoles - a total of 29 main magnets. In addition, each sector has four fast multi-function corrector magnets. The layout of these magnets within a sector is shown in Figure 2.32, and a summary of the different main magnet types is given in Table 2.28. The lengths of the magnets are unchanged relative to the preliminary design report with the exception of Q4 which was lengthened from 0.244 to 0.260 meters. The magnet functions and correction windings are unchanged. The strengths have had modest adjustments, documented in the individual magnet engineeering specification documents.

Table 2.28. Summary of MBA magnet types

Magnet type	**Q1**	**Q2,Q3,Q6**	**Q4**	**Q5**	**Q7**	**Q8**
Qty/Sector	2	2	2	2	2	2
Qty total	80	240	80	80	80	80
Insertion length (m)	0.250	0.225	0.260	0.150	0.424	0.646
Pole tip material	VP	ST	VP	ST	VP	VP
Trim winding?	No	No	H	H	H+V	H+V
Magnet type	**S1,S3**	**S2**	**M1**	**M2**	**M3**	**M4**
Qty/Sector	2	2	2	2	2	1
Qty total	160	80	160	160	80	40
Insertion length (m)	0.230	0.260	2.225	1.986	0.820	0.700
Pole tip material	ST	VP	ST	ST	VP	VP
Trim winding?	H[a]+V[a]	H[a]+V[a]	No	No	H	H

[a] S2, S3 trim windings unpowered.

ST = low carbon steel
VP = vanadium permendur

There are three types of dipole bending magnets: longitudinal-gradient dipoles (L-bends), transverse-gradient dipoles (Q-bends), and reverse-bend dipoles (R-bends). The M1 and M2 L-bends have different field strength profiles along their length. The field strength profiles of A: M1 and B: M1 mirror each other longitudinally, as do A: M2 and B: M2. The Q-bend transverse gradient dipoles (M3 and M4) and R-bends (Q4, Q5, Q8) resemble quadrupole magnets where the beam axis is offset from the geometrical center of the magnet to create both dipole and quadrupole field components. The three Q-bends, located in the FODO section of Figure 2.32, come in two varieties: the two M3 magnets are identical, while the single M4 at the center of the sector is unique, with its own length and field strength. There are three varieties of R-bends: two Q4 magnets, two Q5 magnets, and two Q8 magnets per sector. Magnet and power supply designations for the APS-U storage ring are documented in the APS-U Functional Requirements Document[**AccelFReD**].

The 10 quadrupole magnets in each sector come in four sizes: Q1, Q2, Q3/Q6, and Q7. Magnets Q3 and Q6 are identical and have a slot opening for a photon beam chamber. The Q2 magnet does not have an opening for a photon beam chamber, but is the same length as Q3/Q6. Q2, Q3, and Q6 use the same coils and are located in the doublet and multiplet sections shown in Figure 2.32, and have solid steel cores. Quadrupoles Q1 and Q7 use vanadium permendur pole tips to achieve a high field strength. The Q7 magnet is a multi-function magnet capable of producing a quadrupole field, vertical dipole field, and a horizontal dipole field.

All sextupole magnets have the same cross section. All sextupoles are solid steel core multi-function magnets capable of producing a sextupole field, vertical dipole field, and a horizontal dipole field. The S2 sextupole will have trim coils but will not be supplied with trim power supplies. S1 and S3 use steel pole tips, while S2 has vanadium permendur pole tips to meet the high magnet strength requirements.

All magnets except the eight-pole correctors are water cooled. In addition all magnets except M1 and M2 are powered individually. The M1 magnets are connected in series by a single large power supply, as are the M2s.

The eight-pole laminated fast corrector magnets produce vertical and horizontal dipole fields as well as a skew quadrupole field. The corrector magnet is 158 mm long and capable of bending the stored beam by 300 micro radians. The maximum required integrated skew quadrupole field is 0.25T. There are four fast corrector magnets in each sector.

2-3.2.1 Magnetic Measurements

All magnets will be measured to ensure that they meet the field quality requirements. These measurements will also provide data on field strengths in various magnets needed for operation of the accelerator. Multipole content will be measured with rotating wire / coil arrangements optimized for each magnet type.

All magnets other than M1 and M2 will be fiducialized indiviually using a wire-based system and then accurately placed on assemblies using survey and / or precision-machined surfaces on the support structure. It is expected that an alignment of better than 0.030 mm rms will be achieved without the need to shim individual magnets, but any magnet found to be unacceptably misaligned (offset of more than $\sim$0.06 mm, say) will be shimmed to improve the overall alignment. Another reason to use shims would be to correct magnetic roll angles in magnets that do not meet the $\pm$0.4 mrad magnetic roll specification

The L-Bend dipoles M1 and M2 will be mapped with a Hall probe scanning system. The end shields will be adjusted if needed keep the strengths of all magnets within a tight tolerance band, which is necessary since M1 and M2 are powered in series.

All magnetic measurement data will be stored in the component database along with other magnet data such as design documents, electronic traveler and inspection data.

2-3.2.2 Magnet Documentation

The ICMS document numbers for engineering specifications, interface control documents, and final design review reports are shown in Figure 2.33.

Item	Engineering Specification Document (ESD)	Interface Control Document (ICD)	Final Design Review (FDR), Reports
Q1	aps_1702778	apsu_1708377	apsu_1699218
Q2	aps_1702783	apsu_1708378	apsu_1699218
Q3	apsu_1709174	apsu_2011631	apsu_2014649
Q4	apsu_2011633	apsu_2011632	apsu_2014649
Q5	apsu_2011634	apsu_2011635	apsu_2014649
Q6	aps_1702783	apsu_1708378	apsu_2014649
Q7	apsu_2011638	apsu_2011636	July 2019
Q8	apsu_2011643	apsu_2011645	July 2019
S1	apsu_1710779	apsu_1710780	apsu_2019378
S2	apsu_2011637	apsu_2011639	apsu_2019378
S3	apsu_1710779	apsu_1710780	apsu_2019378
M1	apsu_2011648	apsu_2011647	apsu_2026499
M2	apsu_2011649	apsu_2011650	July 2019
M3	apsu_2011644	apsu_2011642	apsu_2026499
M4	apsu_2011641	apsu_2011640	July 2019
Fast Corrector	apsu_2011564	apsu_1709189	apsu_2010542

Figure 2.33. Document set for magnets.

2-3.3 Vacuum System

2-3.3.1 Vacuum System Overview

The accelerator vacuum system is a hybrid system utilizing chamber geometries, materials, coatings, and pumping strategy to best fit the space, thermal load, and gas loads expected. Strong bending magnets are at the center of the arc creating large thermal and outgassing loads. In this area NEG-coated water-cooled copper chambers are utilized mitigate the loads. The four large longitudinal-gradient dipole magnet are C-shaped allowing for traditional aluminum chambers extruded with an ante-chamber. The ante-chamber allows space for NEG strip pumping. The four fast corrector magnets require a non-magnetic low-resistivity chamber material. In these areas NEG-coated inconel chambers are utilized. Most of the remaining chambers are NEG-coated aluminum round chambers to minimize the Photon Stimulated Desorption (PSD) gas load. Accelerator vacuum system requirements are documented in the APS-U Functional Requirements Document[**AccelFReD**]. A list of vacuum components on the electron beam path are shown in Figure 2.34 and maintained in document apsu_1709946.

Since the Preliminary Design Report was written, further vacuum system optimization has take place. Gate valves in the FODO section were shown to be not needed and have been removed. To further mitigate the gas loads and pressure in the quad double and multiplet regions, NEG coatings have been added to the round chambers. A simulation plot for the expected vacuum pressure before and after these changes is shown in Figure 2.35. The changes provide additional margin in meeting the vacuum pressure requirements.

Simulations have been performed to show the vacuum pressure during vacuum conditioning with beam and is shown in Figure 2.36. The additional NEG-coated chambers helps to improve the vacuum conditioning. The simulations agree with experiences at other facilities.

The Vacuum Final Design documentation status is shown in Figure 2.37 and is maintained in document apsu_2032278.

	Comp. Name	Component Type	Module	Passes Through Magnet(s)	Chamber Material	Chamber Length (mm)	Upstream S-coord. (meters)	Downstream S-coord. (meters)
1	A:P0	BPM	-	-	316L SST	77.0	2.714	2.791
2	A:GV1	Gate valve	DLM-A	-	316L SST	72.0	2.803	2.874
3	A:VC1	Round chamber	DLM-A	A:Q1	Al-6063	303.4	2.874	3.178
4	A:P1	BPM	DLM-A	-	316L SST	70.0	3.178	3.248
5	A:VC2	Round chamber	DLM-A	A:FC1/A:Q2	Inconel 625	565.2	3.248	3.813
6	A:VC3	L-bend chamber	DLM-A	A:M1	Al-6063	2274.8	3.813	6.088
7	A:EA1	Photon absorber	DLM-A	A:M1	OFE Cu	-	-	-
8	A:VC4	Keyhole chamber	DLM-A	A:Q3	316LN SST	350.5	6.088	6.439
9	A:P2	BPM w/ keyhole	DLM-A	-	316L SST	70.0	6.439	6.509
10	A:VC5	Keyhole chamber	DLM-A	A:S1	316LN SST	307.1	6.509	6.816
11	A:VC6	Cross	DLM-A	-	Al-6063	155.0	6.816	6.971
12	A:CA1	Photon absorber	DLM-A	-	OFE Cu	-	-	-
13	A:VC7	Round chamber	DLM-A	A:Q4	Al-6063	330.2	6.971	7.301
14	A:P3	BPM	DLM-A	-	316L SST	70.0	7.301	7.371
15	A:VC8	Integrated cross	DLM-A	A:S2/A:Q5	Al-6063	599.5	7.371	7.970
16	A:VC9	Round chamber	DLM-A	A:FC2	Inconel 625	271.0	7.970	8.241
17	A:VC10	Round chamber	DLM-A	A:S3	Al-6063	293.6	8.241	8.535
18	A:P4	BPM	-	-	316L SST	70.0	8.535	8.605
19	A:VC11	Round chamber	QMQ-A	A:Q6	Al-6063	289.1	8.605	8.894
20	A:VC12	L-bend chamber	QMQ-A	A:M2	Al-6063	2034.6	8.894	10.929
21	A:EA2	Photon absorber	QMQ-A	A:M2	OFE Cu	-	-	-
22	A:VC13	Round chamber	QMQ-A	A:Q7	OFE Cu	511.5	10.929	11.440
23	A:P5	BPM	-	-	316L SST	70.0	11.440	11.510
24	A:VC14	Round chamber	FODO	A:M3/A:Q8	OFE Cu	1764.5	11.510	13.275
25	A:VC15	Cross	FODO	-	316L SST	70.0	13.275	13.345
26	A:P6	BPM	FODO	-	316L SST	46.1	13.345	13.391
27	A:VC16	Round chamber	FODO	A:M4/B:Q8	OFE Cu	1693.3	13.391	15.084
28	B:P6	BPM	FODO	-	316L SST	70.0	15.084	15.154
29	B:VC11	Keyhole chamber	FODO	B:M3	OFE Cu	925.5	15.154	16.080
30	B:P5	BPM w/ keyhole	-	-	316L SST	70.0	16.080	16.150
31	B:VC10	Keyhole chamber	QMQ-B	B:Q7	OFE Cu	511.7	16.150	16.662
32	B:VC9	L-bend chamber	QMQ-B	B:M2	Al-6063	2034.6	16.662	18.696
33	B:CA1	Photon absorber	QMQ-B	B:M2	OFE Cu	-	-	-
34	B:VC8	Round chamber	QMQ-B	B:Q6	OFE Cu	289.1	18.696	18.985
35	B:P4	BPM	-	-	316L SST	70.0	18.985	19.055
36	B:VC7	Round chamber	DLM-B	B:S3/B:FC2	Inconel 625	565.2	19.055	19.620
37	B:VC6	Integrated cross	DLM-B	B:Q5/B:S2	Al-6063	598.8	19.620	20.219
38	B:P3	BPM	DLM-B	-	316L SST	70.0	20.219	20.289
39	B:VC5	Integrated cross	DLM-B	B:Q4/B:S1	Al-6063	792.2	20.289	21.082
40	B:P2	BPM	DLM-B	-	316L SST	70.0	21.082	21.152
41	B:VC4	Round chamber	DLM-B	B:Q3	Al-6063	350.5	21.152	21.502
42	B:VC3	L-bend chamber	DLM-B	B:M1	Al-6063	2274.8	21.502	23.777
43	B:EA1	Photon absorber	DLM-B	B:M1	OFE Cu	-	-	-
44	B:VC2	Round chamber	DLM-B	B:Q2/B:FC1	Inconel 625	505.2	23.777	24.282
45	B:FA1	Photon absorber	DLM-B	-	OFE Cu	60.0	24.282	24.342
46	B:P1	BPM	DLM-B	-	316L SST	70.0	24.342	24.412
47	B:VC1	Round chamber	DLM-B	B:Q1	OFE Cu	301.1	24.412	24.713
48	B:GV1	Gate valve	DLM-B	-	316L SST	72.0	24.713	24.785
49	B:P0	BPM	-	-	316L SST	77.0	24.824	24.901

Figure 2.34. Vacuum system component list.

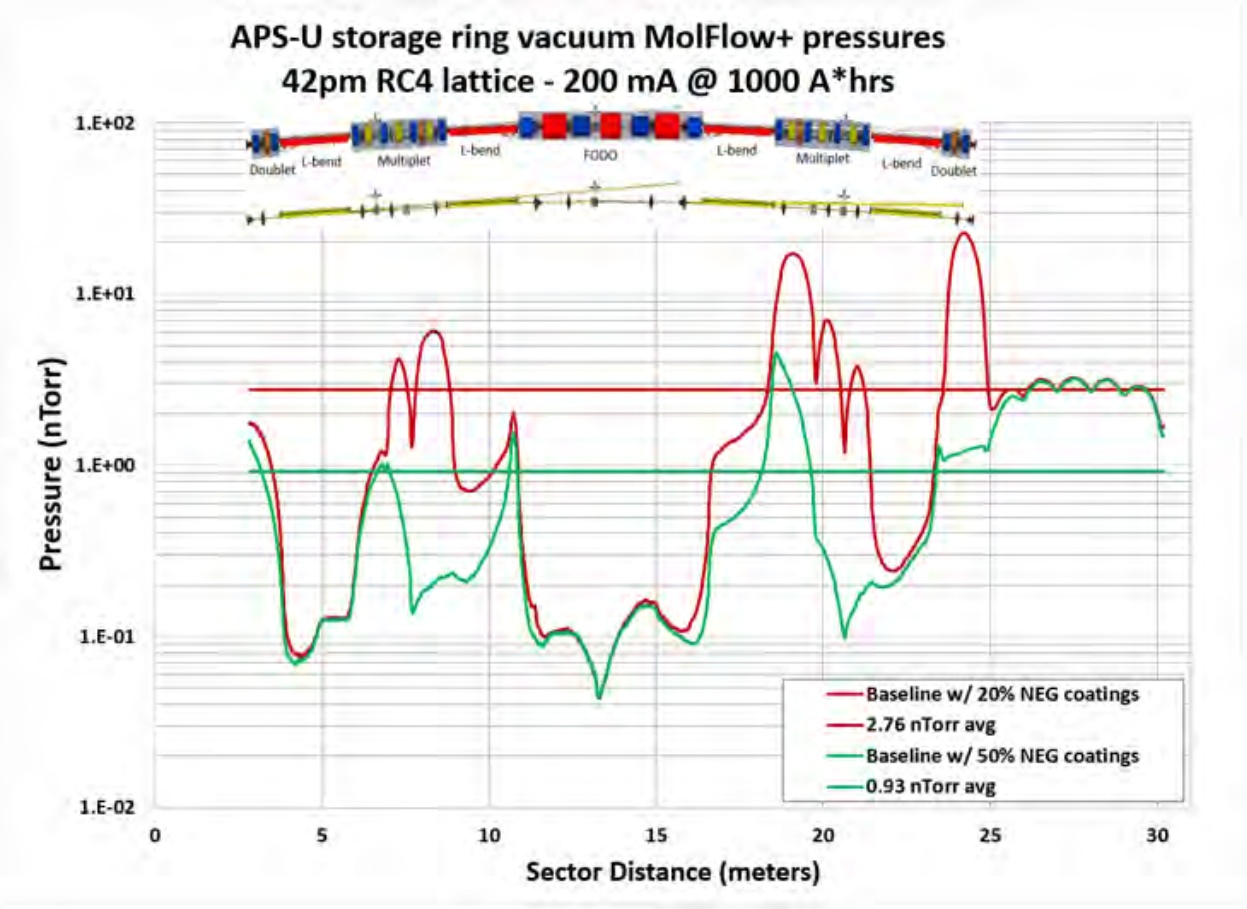

Figure 2.35. Sector arc vacuum pressure profile.

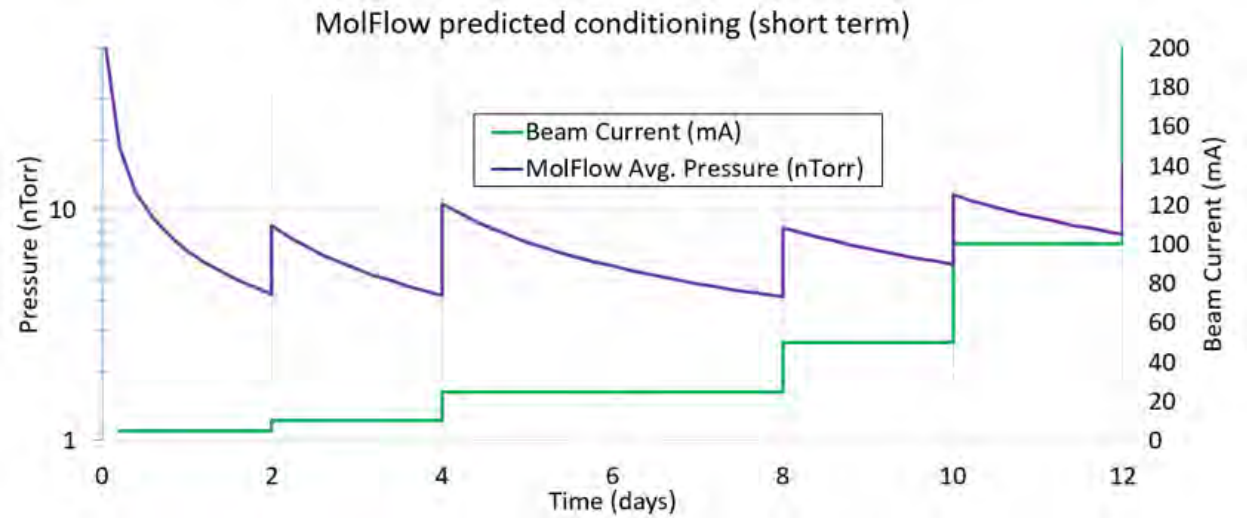

Figure 2.36. Vacuum pressure conditioning simulation.

Item Type	Engineering Specification Document (ESD)	Interface Control Document (ICD)	Final Design Review (FDR) Reports
NEG, L-Bend, End Plates	apsu_1709945	apsu_1709946	apsu_2019168 apsu_2025415
Chamber Supports, NEG Strips	apsu_1709945	apsu_1709946	apsu_2019168 apsu_2025447
Fast Corrector Chambers	apsu_1709945	apsu_1709946	apsu_2019168 apsu_2021926
Key Shaped	apsu_1709945	apsu_1709946	apsu_2019168 apsu_2031321
Beam Position Monitors	apsu_1709945	apsu_1709946	apsu_2019168 apsu_2032698

Figure 2.37. Vacuum system Final Design Documentation summary.

2-3.4 Magnet Support and Alignment System

The new magnet lattice requires the magnet support structures to be mechanically and thermally stable in order to satisfy the stringent physics requirements. The magnet alignment requirements are shown in Table 2.12. The vibration and stability requirements are shown in Table 2.9. In addition, the key design drivers outline a short installation window, dictating that ease of installation and alignment is a significant consideration in the magnet support structure design. These constraints inform all aspects of the design process. From simulation, to testing, each step is used to evaluate the preliminary design against the requirements.

Each storage ring sector consists of three large modules with two support plates supporting three magnets each (QMQ) bridging between them. Figure 2.38 shows one of the 40 sectors of the proposed storage ring lattice. The upstream Doublet L-bend Multiplet (DLM) module A supports a quadrupole doublet, an L-bend, and a multiplet array of magnets. In the center of the sector is the curved Focusing Defocusing (FODO) module which supports five large bending / focusing magnets. The downstream DLM module B is a mirror image of the upstream DLM module A. Each module contains a concrete plinth grouted to the floor, upon which is an alignable support girder, which in turn supports the individual magnet strings, vacuum system, and auxiliary hardware. Each of these modules will be delivered to one of the five "super doors" that are located on the inner circumference of the storage ring. From the super door, each module will be transported via the storage ring aisle to the final installation location.

Figure 2.38. Plan and elevation views of the APS Upgrade lattice. The different magnet groups include two DLM modules, a FODO module, and two quadrupole / L-bend dipole / quadrupole (QMQ) bridges. The DLM and FODO structures are supported from concrete plinths grouted to the floor, with QMQ modules supported by the ends of the plinths.

2-3.4.1 Support Concept

Each of the magnet modules consists of a plinth grouted to the floor and a three-point, semi-kinematic mount for the magnet support structures. The groups of individual magnets are mounted on top of a rigid magnet support structure. Figure 2.39 shows the details of the FODO module. Each plinth is rigidly bonded to the storage ring floor using epoxy grout. Plinths are fabricated using a welded steel frame filled with reinforced concrete. Each support girder is made of ductile cast iron. In addition to supporting the magnets, all vacuum system components are mounted to the girder. The support girder geometries are optimized to minimize weight while providing a very stiff structure that maximizes the first vibrational mode frequency and minimizes static deflection. The casting process allows economic fabrication of the optimized support girder geometries.

The FODO module, the upstream DLM module A and the downstream DLM module B are all of

Figure 2.39. Preliminary FODO module assembly consists of (bottom to top) epoxy grout, concrete/steel plinth, cast iron support girder, individual magnets and vacuum system.

similar design with standardized support and alignment system components. The M2 L-bend dipole magnets are not part of either the FODO or DLM modules, but span between them on the QMQ modules. Shown in Figure 2.40 is the DLM-A assembly, and in Figure 2.41 is QMQ-A. The DLM-B and QMQ-B modules are essentially mirror images of DLM-A and QMQ-A respectively.

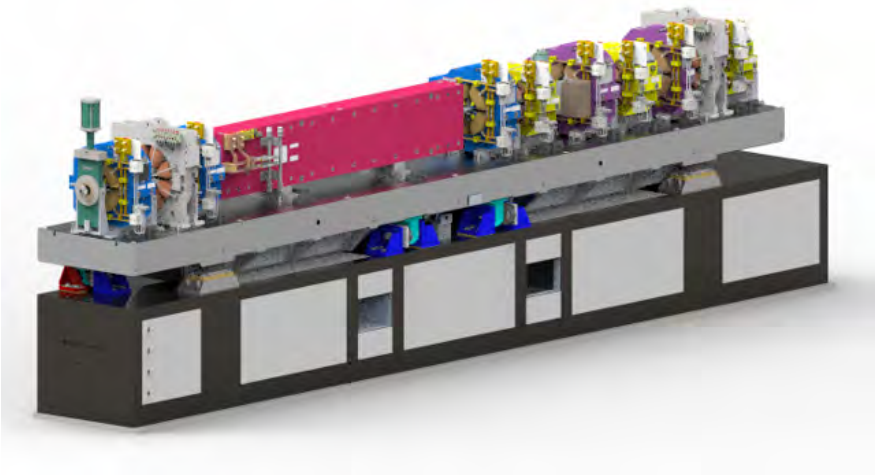

Figure 2.40. Doublet L-Bend Multiplet A (DLM-A) assembly.

2-3.4.2 Magnet and Plinth Transport and Assembly

The large combined weight of each module requires that extra consideration be given to rigging and transport. The 6.3 m long FODO module has a mass of approximately 27,000 kg. The DLM modules will have slightly less mass than the FODO module but their length will be close to 6.5 m. To meet the installation schedule, the magnet modules will be fully assembled during pre-installation and will later be transported to the storage ring as complete assemblies.

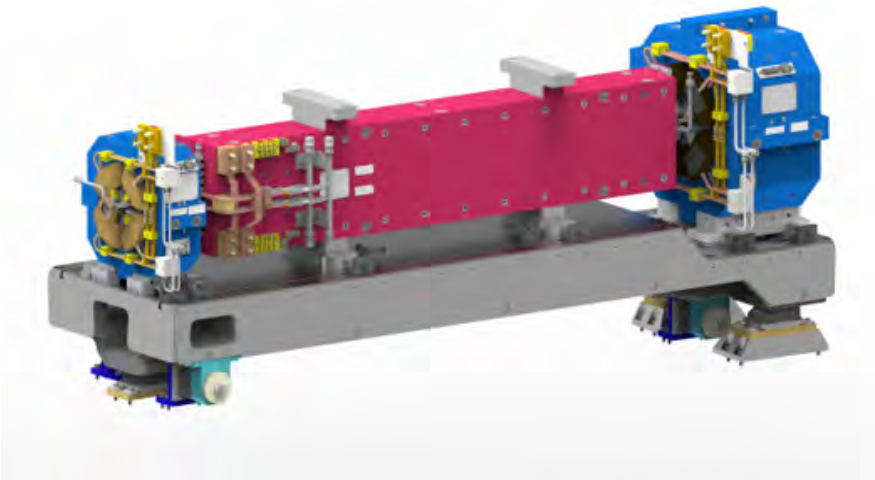

Figure 2.41. Quadrupole Dipole (M2) Quadrupole (QMQ) bridge assembly.

The FODO prototype has shown that strict machining tolerances used to position magnets can still be maintained on a longer, more massive girder. Flatness of the FODO prototype girder, supported on three points with dummy magnets installed, measured 10 microns, well within positioning tolerances.

A plinth transporter system has been demonstrated during the R&D phase to be able to safely transport the heavy plinth assemblies.

2-3.4.3 Mechanical Supports Documents

The ICMS document numbers for engineering specifications, interface control documents, and final design review reports are shown in Figure 2.42.

Item	Engineering Specification Document (ESD)	Interface Control Document (ICD)	Final Design Review (FDR) and Review Report
DLM-A	apsu_2011164	apsu_2011147	apsu_2031655
DLM-B	apsu_2011165	apsu_2011148	apsu_2031655
QMQ	apsu_2011177	apsu_2011107	apsu_2031655
FODO	apsu_2011166	apsu_2011149	apsu_2031655

Figure 2.42. APS-U Mechanical Supports Documentation.

2-3.5 Power Supply System

2-3.5.1 Overview

The general approach to powering the MBA magnets is much the same as for the existing APS. All the multipole magnets, Q-bend dipoles, trim, and corrector windings are powered by individual DC-to-DC power converters. Two stand-alone power supplies provide power to the M1 and M2 families of longitudinal-gradient dipoles, which are each powered in series. A total of 1002 unipolar, 921 slow-bipolar and 322 fast-bipolar power supplies are required. Magnet power supply requirements are listed in the respective engineering specification documents found at the end of this section.

A generic block diagram of a magnet power converter is shown in Figure 2.43. Unipolar or bipolar DC-DC converters will be supplied with unregulated DC power from common transformer/rectifier units (four per sector). Magnet currents are monitored by precision DC current transducers (DCCTs) that are external to the power supplies and stay with the magnet "slots" when converters are replaced. Since the external DCCTs are outside of the current regulation loop, they provide independent readback verification of magnet currents. Keeping the DCCT and its electronics with the magnet slot allows a new converter to be calibrated to provide exactly the same output current as the converter being replaced. These DCCTs will also be the essential components of the overall calibration scheme. The diagram assumes that the current regulation is internal to the DC-DC converter.

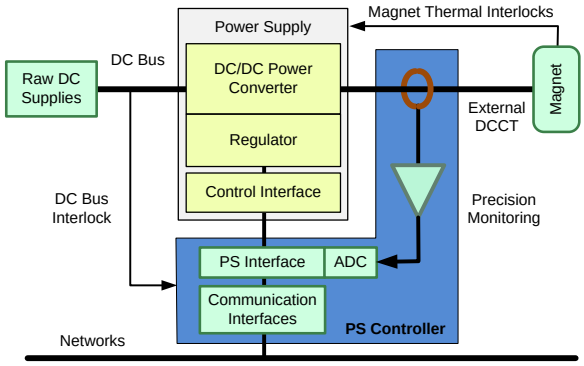

Figure 2.43. Magnet power supply generic block diagram

The power supply controller provides the communication interfaces between the power supplies and multiple networks, including the EPICS-based controls network, a bulk data network, and a synchronized data acquisition (DAQ) system. Common power supply controllers are used to control multiple power supplies in one power supply cabinet. Besides providing monitoring and controls for the power converters themselves, the power supply controllers monitor thermal conditions of the cabinets and conditions of the DC busses.

Requirements for power supply stability and accuracy are more demanding than for those of the present APS. The main multipole and dipole magnets require 10-ppm-class unipolar power supplies, and calibration will be traceable to magnet measurement data.

Based on the power ratings, output polarities, and output bandwidths, four power supply types are

needed:

1. Unipolar DC power supplies with output powers of several hundred kilowatts and output currents of several hundred amperes for the series-connected M1 and M2 dipole families;
2. Unipolar DC power supplies with output currents up to 280 A and a power rating in kilowatt ranges to power quadrupole, sextupole, and M3 and M4 dipole magnets;
3. Slow bipolar DC power supplies with output currents up to +/-15A and power ratings of several hundreds of watts for slow correctors, skew quadrupoles, and dipole trim coils;
4. Fast corrector power supplies that can make fast changes in its output voltage and current to meet the requirement from the fast beam correction magnets. The power rating of the fast corrector power supplies is similar to that of the slow DC power supplies. These will be four-quadrant power supplies.

2-3.5.2 Stand-alone Unipolar Power Supplies for M1 and M2 Dipole Strings

Stand-alone commercial power supplies will power the 80-magnet strings of the M1 and M2 dipole families. Although the two strings have different ratings, the same power supply model is assumed for each string in order to simplify power supply support and maintenance. Commercial power supplies that will meet the stability requirement will be used.

2-3.5.3 Unipolar DC-DC Power Converter System

The design for the unipolar DC power supply system is based on a commercial DC-DC power converter unit specified at 10 parts-per-million stability, and customized to meet APS-U needs. The modifications are mostly in the input and output stages of the commercial power supply in order to utilize the existing APS DC distribution system. Three models (100 Amp., 200 Amp., and 300 Amp) will be used to cover the range of operating currents.

2-3.5.4 Bipolar DC-DC Converter System for Trims, Slow Correctors, and Skew Quads

The total number of slow bipolar DC power supplies is 921, which includes 760 power supplies for trims coils in the main magnets and 161 power supplies for skew quadrupole magnet coils.

The design of the slow bipolar DC power supplies is very similar to the design for the bipolar DC power supply system for the fast correctors, described below. The major difference is in the size of the output filter. Being a power supply without need of changing the output quickly, a much larger filter can be used in the output stage of the circuit to significantly reduce the ripple in the output voltage and hence the ripple current in the magnet.

2-3.5.5 Bipolar Power Supply System for Fast Correctors

There are four fast-corrector magnets in each sector, driven by eight power supplies: four in the vertical plane and four in the horizontal plane for use in orbit correction.

The power supply requirements for the fast correctors are similar to those for the slow bipolar power

Figure 2.44. Prototype fast corrector power supply.

supplies with the addition that the output current needs to have a small-signal -3dB bandwidth of 10 kHz in order to minimize the power supply impact on the closed-loop performance of the fast-orbit-feedback (FOFB) system.

The design of the fast corrector power supplies is based on the prototype power supply developed through the R&D activities (Figure 2.44). The power supply is a switching-mode DC-DC converter utilizing a standard H-bridge topology with four MOSFETs as the switching devices.

The power supply receives an analog signal from the power supply controller as the reference for the output current. The output current is sensed with a DCCT for its superior performance in the stability and the gain accuracy. The current feedback loop uses a phase-lead compensator in addition to a standard proportional-and-integral compensator to minimize the phase delay at high frequencies.

The input of the power supply uses the APS' existing 40-volt DC distribution system, which is fed from four three-phase diode-rectified DC raw power supplies with little filtering at the outputs. To reduce the ripple components in the DC bus voltage, an L-C low-pass filter is used at the input circuit of the power supply. A soft-start circuit will be used to reduce the inrush current so that the power supply may be swapped without turning off the DC distribution system.

The output stage of the power supply contains a critically damped L-C filter. The filter is necessary to reduce the high frequency components in the output voltage to reduce the electromagnetic interferences. The cut-off frequency of the filter is designed at 159 kHz (determined by available commercial L and C components) and it does not significantly affect the dynamical performance of the power supply.

The MOSFET devices are mounted on a common heatsink that is forced-air cooled. Two 40-mm fans are used to provide the require cooling with redundancy to improve the reliability. The fan speed is PWM-controlled proportional to the output current with a minimum speed of 50%.

2-3.5.6 Power Supply Controllers

There are two types of power supply controllers, one for the unipolar power supplies and one for the bipolar power supplies, including both slow and fast corrector power supplies. There are a total of

200 unipolar power supply controllers and 200 bipolar power supply controllers. Each controller is installed in a cabinet that houses the type of the power supplies to be controlled by the controller. The controller design shares many functions that are common to both the unipolar power supplies and the bipolar power supplies. The main differences are in the digital and analog input and output where the two types of power supplies have different requirements.

For the bipolar power supplies, each controller sends analog references for the output current to up to eight bipolar power supplies. The analog input module (18-bit AIN) reads analog signals from each power supply. The digital input/output monitors the power supply status and performs the reset and on or off functions. Every bipolar power supply has an embedded unique serial number and the serial number is read by the controller through digital I/O.

For the unipolar power supplies, a serial peripheral interface (SPI) will be used to communicate with the vendor-designed power supplies for all necessary control and monitoring purposes. The SPI can accommodate a change rate of the setpoints up to 10 Hz with a latency much less than 10 msec.

Precision 32-bit ADCs (20 bit ENOB) for digitizing the independent DCCT readbacks are housed in a separate temperature-controlled chassis together with the DCCT electronics and burden resistors.

A high-speed communication interface common to both types of the power supplies is based on a Gigabit Ethernet designed by LBNL. The communications with this interface include EPICS, FOFB/DAQ, and bulk data communication. The EPICS communication provides general power supply supervisory functions. FOFB/DAQ link to the FOFB system receives the set points for the fast corrector power supplies at 22.6 kHz with a latency less than 10 microseconds.

External measurements of output current and other important parameters from both unipolar and bipolar power supplies can be streamed back and synchronized with the global RTFB clock at 22.6 kHz through this interface to the DAQ system for global time-correlation with other accelerator events. A memory buffer stores the current waveforms for at least one second. Waveforms can be read back with time-stamps through a dedicated bulk data network for postmortem analysis when triggered by an internal event such as a glitch in the output current or an external event such as a beam motion or a beam loss.

Each power supply controller will have a temperature input to monitor the ambient temperatures in the power supply cabinet or relay racks to correlate the power supply performance with the environmental conditions.

2-3.5.7 External Current Measurement and Calibration System

The output currents of both the bipolar and unipolar power supplies require independent measurement for verification. The precision of the measurement needs to be 18 bits or better for the unipolar power supplies but may in principle be an order of magnitude more relaxed for the bipolar power supplies. A common precision ADC circuit will be used for both types of power supplies, although the bipolar power supplies may not need such a high precision.

In order to maintain the accuracy of the current measurement system, particularly for the unipolar

power supplies, a calibration system will be installed to allow automated, in situ calibration of all 1000 channels. This system will provide precise, NIST-traceable calibration current to a multi-turn calibration winding inside each DCCT. The calibration winding multiplies the calibration current by a factor of 1000, allowing the full range up to 300 A to be calibrated using a 300 mA precision current source. The known calibration current will allow an end-to-end calibration of each channel, including the DCCT, the burden resistor, and the precision ADC circuit.

Three calibration schemes have been tested in the R&D program. Scheme 1 calibrates multiple DCCTs with one common calibration current. The issue with this scheme is the number of DCCTs that can be connected in series and driven by one calibration current source is small due to the winding resistance and the available voltage from the current source. Scheme 2 uses an additional DCCT with a calibration winding of 100 turns and a null circuit with a power supply to produce a large calibration current, 10 A for example, from a small precision current reference. Scheme 3 uses an incremental calibration method that relies on a stable power supply to produce the main current through the DCCT at large incremental steps, 10A steps for example, and uses a small calibration current to calibrate DCCTs between steps. All three schemes proved to be able to achieve the goal of the calibration, but each if used alone has limitations in the engineering implementation.

With regard to the calibration scheme, the design proposes to use a scheme that uses a small current standard to produce the required calibration current through a null circuit for the DCCTs in one power supply cabinet. Since the required current standard is small, a few milliamperes, one current standard is capable of delivering the current to many cabinets connected in series. Figure 2.45 illustrates how the proposed scheme works.

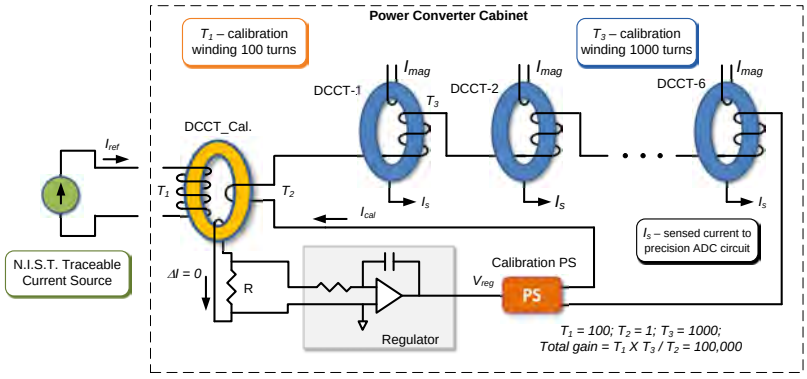

Figure 2.45. Precision current measurement system in-situ calibration diagram.

In this scheme, DCCT-1 through DCCT-6 are the external DCCTs in one power supply cabinet. Each DCCT has a built-in calibration winding with 1000 turns. DCCT-cal is a calibration DCCT with a 100-turn calibration winding. A null circuit and small power supply can produce a calibration current 100 times the current from an NIST traceable standard. The total current gain in the circuit is 100,000, which means a reference current of three milliamperes can perform a 300 A full range calibration.

The resistance of the 100-turn calibration winding is typically less than 1Ω. With a few milliamperes in the winding, the voltage drop will be only a few millivolts. Therefore, one precision current source can drive many 100-turn calibration windings in series, making the total number of the precision

current sources small and maintainable.

2-3.5.8 Power Supply Communication Structure

Figure 2.46 shows the design of the power supply communication structure in a double sector. It has three communication links for different controls and communication purposes. Links 1 and 2 are used for the power supply operations and slow monitoring, while Links 3 and 4 are used for fast monitoring and diagnostics.

Link 1 interfaces with the EPICS-based controls network. It delivers the DC set points to the unipolar power supplies. It handles the power supply logistics such as ON and OFF commands and interlock or fault resets. It reads back the monitored stationary signals such as the interlock conditions, the magnet temperatures, and other power supply status. The set points for the slow bipolar power supplies and the fast corrector power supplies may also be sent through this link under certain operation or power supply maintenance modes.

Link 2 is for delivering the bipolar power supply set points, including the set points for both slow and fast bipolar power supplies. It connects the bipolar power supply controller to the power supply interface hardware in the double-sector-controller chassis of the orbit feedback system. Link 2 also provides an interface for the synchronized data read back from both bipolar and unipolar power supplies. Through this link, the power supply output current and other important data can be streamed back synchronously with the global orbit feedback clock at a frequency of 22.6 kHz.

Link 3 interfaces with the bulk data network. The captured power supply waveforms will be sent through this link.

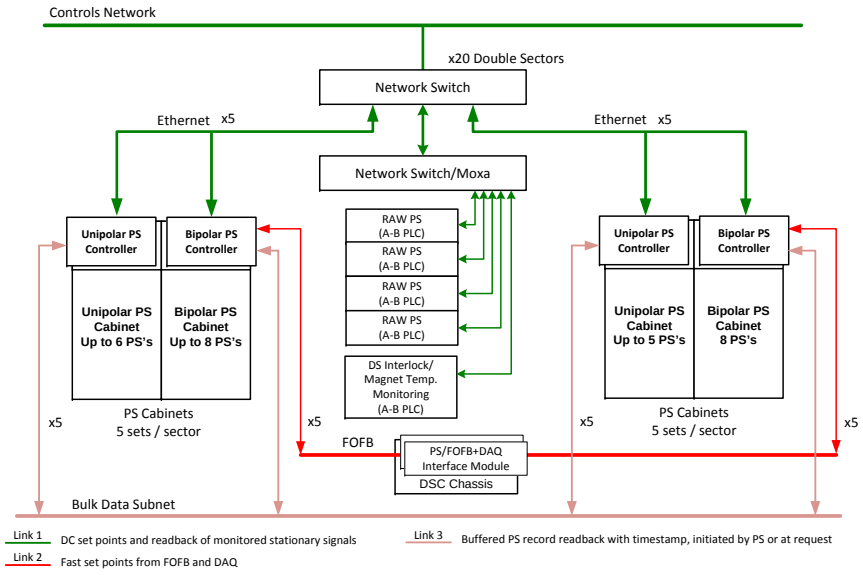

Figure 2.46. Double sector power supply communication structure.

2-3.5.9 Double Sector Configuration and Layout

In the existing APS Storage Ring, the power supply layout is partitioned into 20 identical double sectors. In each double sector, there are four AC-to-DC raw power supplies, named T1 through T4, with associated DC distribution system to deliver DC power to 10 power supply cabinets. The voltage level of the raw DC power supplies is configurable from 40 V to 72 V. The total power capacity of the DC distribution system is 496 kW per double sector, more than the power requirement by the APS-U power supplies. Each double sector has an interlock relay rack that houses the cooling water interlocks, the dipole magnet thermal interlocks, and a control unit to control the raw DC power supplies in the double sector. The design will move the temperature readbacks of the thermocouples on the magnet windings from each power supply, which is the monitoring scheme in the present machine, to the central location in the double-sector interlock relay rack. Commercial PLC-based thermalcouple modules will be used to read the magnet temperatures.

The existing converter cabinets for the unipolar power supplies are designed with safety interlocks on the rear doors. If the door is open, the interlock circuit will trip off the raw DC power supplies and remove the DC power to the cabinets. The front doors of the cabinets are not interlocked since there is no access to live electric circuits from the front. For the new 19-inch relay racks for the bipolar power supplies, there will not be exposed electrical circuit and, therefore, there will not be a requirement for door interlocks.

Because of the existing design of the connections between the DC bus and the unipolar power supplies, the DC bus has to be de-energized and LOTO'd before replacing a power supply. However, in the case of the bipolar power supplies, the DC bus may be left 'on' during a power supply replacement since the connectors with recessed contacts are used at the DC power input, which means a hot swap is possible.

The APS-U power supplies will have a very similar double sector layout: retaining the raw DC power supplies, the DC distribution system, the power supply cabinets, and the double sector interlocks. The output voltages of the raw DC power supplies will be reconfigured to have a uniform 40 V. Since the APS-U will have more power supplies, the existing power supply cabinets do not have sufficient space to house all the power supplies, particularly the bipolar power supplies, without limiting it to a modular design. To avoid this constraint, ten 19-inch relay racks will be added in each double sector to house the bipolar power supplies and the bipolar power supply controllers. Each 19-inch relay rack may contain up to eight bipolar power supplies.

The new double sector layout is illustrated in Figure 2.47, where DCU-PS represents the unipolar DC power supplies, FCB-PS represents the fast corrector bipolar power supplies, and DCB-PS represents the slow DC bipolar power supplies.

2-3.5.10 Power Supply System Documentation

The ICMS document numbers for engineering specifications, interface control documents, and final design review reports are shown in Figure 2.48.

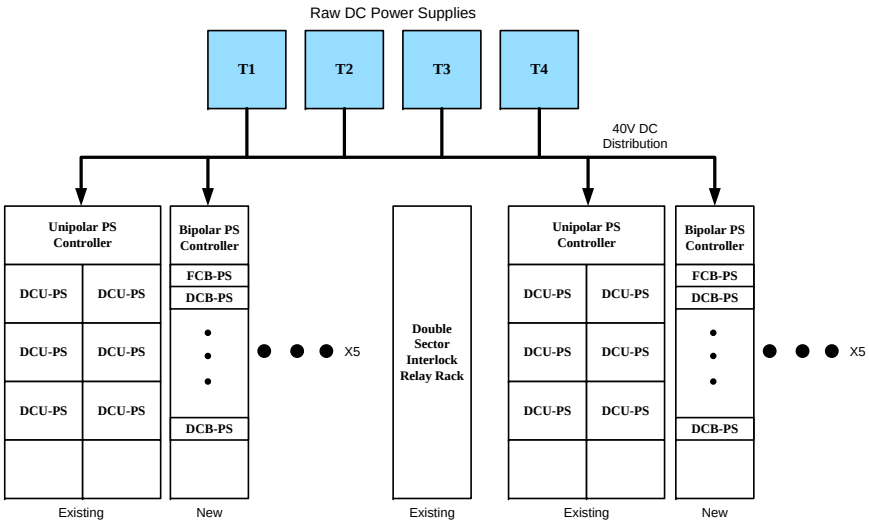

Figure 2.47. Double sector power supply layout.

Power Supply Type	Engineering Specification Document (ESD)	Interface Control Document (ICD)	Final Design Review (FDR) and Review Report
M1 L-Bend Dipole Power Supply	apsu_2031418		
M2 L-Bend Dipole Power Supply	apsu_2032069		
Unipolar Power Supplies	apsu_2012252	apsu_2016863	apsu_2015691
Unipolar Power Supply Controllers			
Trim and Slow Corrector Power Supplies	apsu_2012253	apsu_2030480	apsu_2030679
Fast Corrector Power Supplies	apsu_2012254	apsu_2030481	apsu_2030679
Bipolar Power Supply Controllers			
Unipolar PS External Current Monitoring System	apsu_2012256		
Bipolar PS External Current Monitoring System	apsu_2012258		

Figure 2.48. Power Supply Documentation.

2-3.6 Beam Injection and Extraction Systems

2-3.6.1 Overview

Injection into the MBA storage ring will employ vertical on-axis injection with bunch swap-out, as described in Section 2-2.8. This is a two-step process, where the bunch circulating in the target rf bucket is first kicked out of the machine and the incoming full-charge bunch is then kicked on-axis into the same rf bucket.

As shown in Figure 2.17 (in Sec. 2-2.8), the design concept uses two groups of three fast pulsed kickers located in two separate sectors of the storage ring: the extraction group kicks out the bunch that occupies the target bucket of interest; and the injection group kicks the incoming bunch on-axis and into the now-empty rf bucket. Both sets of kicker pulses must be short enough that bunches upstream and downstream of the target bunch are not unduly disturbed.

A low-amplitude "decoherence-kick" is applied to the bem using a short kicker in the extraction straight in order to decohere the bunch and reduce the power density of the beam. Some 200-300 turns later, the remaining three extraction kickers are pulsed, sending the bunch to the swap-out dump.

Each kicker is a stripline rf structure pulsed by fast high-voltage pulsers. In addition, a Lambertson DC septum deflects the incoming beam both horizontally and vertically upstream of the four kickers. Key requirements are given in Table 2.29. Trajectory diagrams are shown in Fig. 2.18 of Section 2-2.8.

Table 2.29. Fast kicker parameters

Parameter	Units	Value
Kick direction		y-plane
Total kick Angle	mrad	2.592
Number of kickers		3
Kicker strength	mrad/m	1.2
Total Length of each kicker	m	0.75
Peak-to-peak blade voltage (nominal)	kV	± 18
Good-field region	mm × mm	±2.3 × ± 1
Field uniformity	% of center field	2
Minimum bunch spacing (324-bunch mode)	ns	11.4
Maximum residual kick to stored beam	% amplitude	3
Blade length	mm	720
Gap between blades	mm	9
Blade shape		"D"

2-3.6.2 Lambertson DC Septum

Key parameters for the Lambertson septum are given in Table 2.30.

The coil has 14 layers with 4 turns per layer, wound around the top pole. The gap between the top and bottom poles, which provides space for the injected beam, is 10 mm.

The stored-beam chamber is located in the bottom pole. The upstream and downstream X centers

Table 2.30. Lambertson septum parameters. The field uniformity specifications are preliminary, subject to further beam dynamics studies.

Parameter	Value	Unit
Length	1.78	m
Thickness DS end	2	mm
Thickness US end	4.56	mm
Beam separation at DS septum	5.5	mm
Septum thickness tolerance	50	μm
Field Strength	1	T
Bend Angle	84.55	mrad
Tilt Angle	93	mrad
Stored beam deflection angle	$<$50	μrad
Aperture of stored beam chamber ($8 \times v$)	8 x6	mm
Field uniformity (ΔB/B), $\pm$2mm beam vicinity	$\leq$0.001	

of the stored beam chamber are separated by 7.887 cm, resulting in a 47.5 mrad rotation of the stored beam chamber in the XZ-plane against the magnet axis. The material of the stored beam chamber is Vanadium Permendur to effectively shield the stored beam from the field.

Figure 2.49 (a) and (b) show the trajectories of the injected and stored beams with a peak field of 1.06 T at the gap center. The trajectories in Figure 2.49 (a) are referenced to the storage ring coordinate system which was set at the US end, while (b) is referenced to the magnet coordinate system for which the origin is the center of the gap. The outgoing angle, α_2, in Figure 2.49(b), was to the mechanical tilt angle of the stored beam chamber in XZ-plane, which is 47.5 mrad from the magnet axis.

The X position of the injected beam at the DS exit of the septum magnet was set to match the center of the stored beam chamber, resulting in the trajectory of the injected beam matching the stored beam trajectory at the DS end as in Figure 2.49 (a) and (b). The total deflecting angle of the injected beam, $\alpha = \alpha_2 - \alpha_1$, was confirmed as -89 mrad from the trajectory in Figure 2.49 (b), matching the required angle in the specifications. Futher details of the beam trajectories and constraints can be found in the Beam Physics section [2-2.8].

The septum is in mechanical design. Figure 2.50 shows a view of the design model.

2-3.6.3 Stripline rf Design

The vertical kicker stripline geometry matches the differential impedance to 50 Ω while allowing some mismatch in the common mode impedance, the mode which will be excited by the beam. A 'vaned' outer body geometry provides better common-mode impedance matching, while 'D' shaped blades improve field uniformity within the good field region. Tapered end-sections match the impedance of the kicker deflecting cavity to the APS-U beam pipe and impedances of the high-voltage feedthroughs to the striplines. The optimized geometry and parameters are shown in the APS-U PDR[1].

Table 2.31 lists electrical parameters from 3-D simulation.

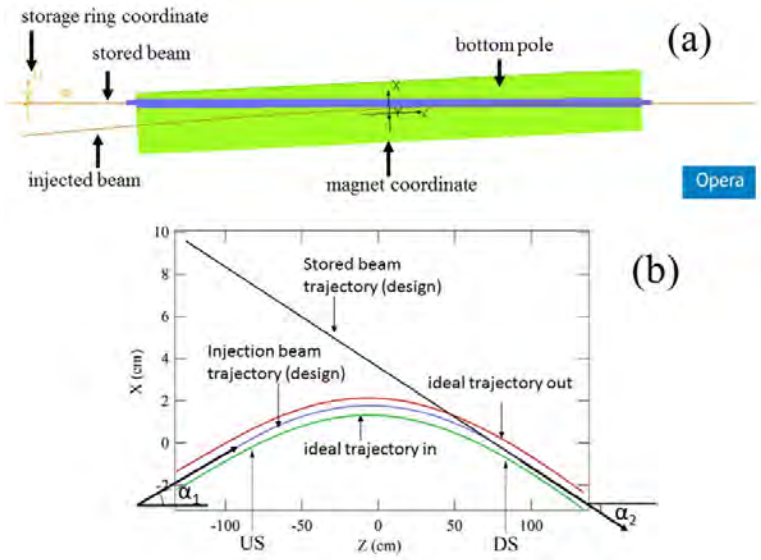

Figure 2.49. Septum magnet top view (a) of the injected and stored electron beam trajectories in the storage ring coordinate system (all other parts except the bottom pole are hidden); (b) Plots of injected and stored electron beam trajectories in the magnet coordinate system. The ideal trajectory (in)board and (out)board show the allowed range of the injected beam in the XZ-plane using an ideal field.

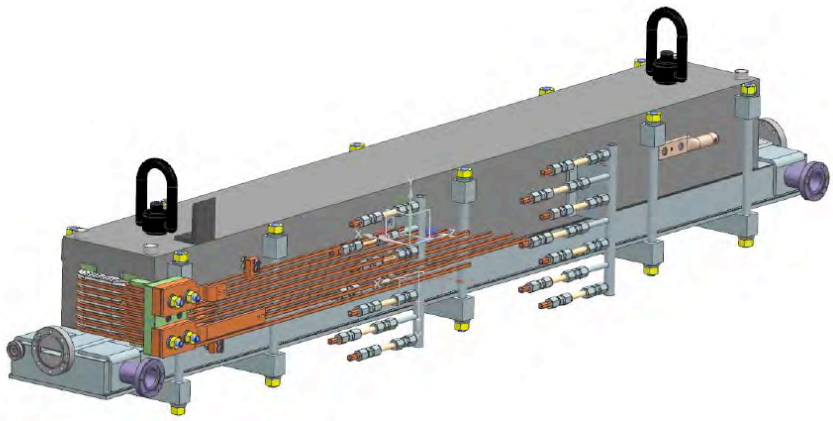

Figure 2.50. CAD model of the Lambertson septum magnet including the vacuum enclosure of the beam lines.

2-3.6.4 High-Voltage Feedthrough

Key specifications are an impedance of 50 $\pm$ 5 Ω and bandwidth $>$ 1 GHz, bakeable up to 150 °C, and compatibility with ultra-high vacuum and high levels of radiation. A photograph of the feedthrough prototype is shown in Figure 2.51. The feedthrough was tested before assembly with the prototype kicker.[2]

Table 2.31. Kicker simulation results with applied ±15 kV pulse

Parameter	Value	Units
Z_{diff}	49.6	Ω
Z_{comm}	63.1	Ω
Ave. E_x	3.015	MV/m
E_{max}	6.77	MV/m
Variation in field	1.4	%

Figure 2.51. Finished prototype feedthrough.

2-3.6.5 Stripline Mechanical Design

Considering the electromagnetic design and current machining practices, the following fabrication constraints were developed for the vertical kickers:

- The blades must be fully-supported by the feedthroughs.
- The stripline kickers are of a 2-blade type design with a main body, taper transitions, feedthroughs, and end-cap flanges.
- The gaps between blades and body must be greater than or equal to 2 mm in order to keep local high-voltage concentration below 13 MV/m (the breakdown field-strength at ± 15 kV in 1 nano-torr vacuum).
- The gaps between blade ends of adjacent kickers must be at least 100 mm to provide space for a flanged bellows section and to avoid mechanical interference between feedthroughs.

The kicker body is 61.8 cm long and is machined from a solid 316-L stainless steel bar using wire EDM (Electrical Discharge Machining). Further machining to improve the inside surface finish will be done through electropolishing. Geometries of the main body and tapered transitions are shown in Figure **??**

The tapered end-sections are high-vacuum furnace brazed to the kicker body using CuSil braze alloy (72% Ag, 28% Cu).

The blades are made from CDA101 high purity copper and are 720 mm long, and are attached to the feedthrough inner conductor with internal brass studs. For the production units, the blades will be blackened to increase the radiation coefficient ϵ to > 0.5 as will be the inside of the kicker body, for radiative cooling efficiency.

Electrical and mechanical tuning techniques have been developed and tested on a prototype unit. In the final assembly, the measured stripline blade separation was 8.75 mm and the center of the blade gap aligned with the center of the kicker body better to a level than the resolution of our coordinate measuring machine (CMM). The measured angular offset of the blades were all less than 0.3 degrees. With these measurements the protoype unit was successfully tested with a 7 GeV electron beam and achieved all required operating parameters: 1 mrad/m deflection, 30 kV peak voltage, and 1 nano-torr vacuum.

Figure 2.52 shows the finished kicker assembly prior to being installed in the APS injector test beamline. During this assembly, coordinates on the parts were measured and compared to the desired geometric shape. For the blade the maximum deviation from the ideal blade thickness was measured to be +75 microns, while for the body the maximum deviation in the middle of the large elliptic arc was measured to +200 microns. These measured deviations are all within the acceptable tolerance.

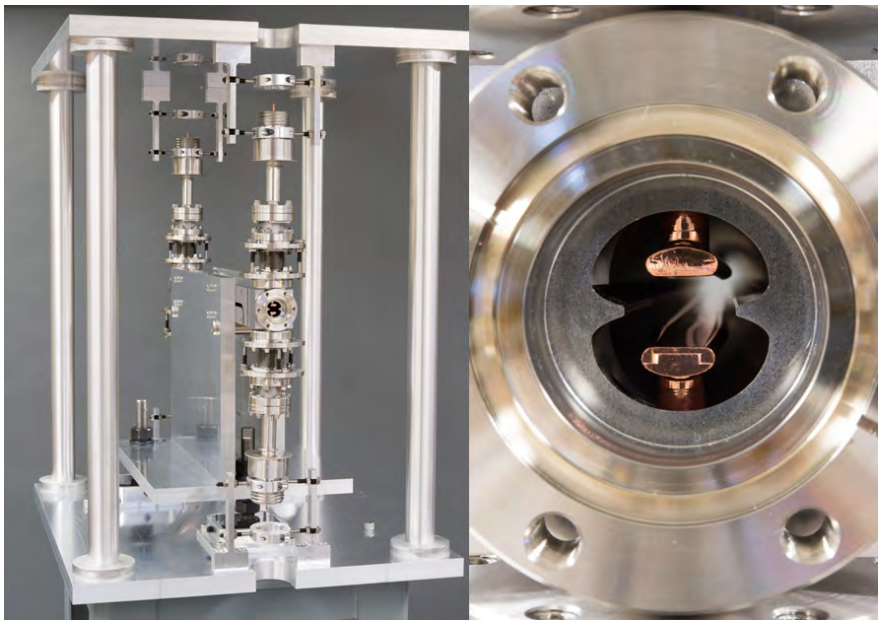

Figure 2.52. Prototype kicker assembly prior to beam testing (Left). The kicker copper stripline blades and a view down the bore of the kicker beam aperture (Right).

2-3.6.6 End-to-end Simulations

Both 2D and 3D simulations have been performed on the optimized geometry with CST studio[3] in order to further validate the design-parameter optimization from the 2-D simulation and to evaluate the end-point geometries [4]. A 3D kicker model is developed based on 2D simulation results, as shown in Figure 1, and CST Microwave Studio (MWS) is applied.

Differential-mode and common-mode TDR simulations were compared with actual TDR measurements from the prototype kicker prior to installation. Figure 2.53 shows good agreement of the differential-mode and common-mode TDR simulations with actual measurements. The simulation correctly shows all the features, and except for the finest structure, the magnitudes of impedance

changes are consistent with the measurements. Impedance-changes for the finer structures are likely a result of under-estimating the rise-time for the injected pulse in the simulation.

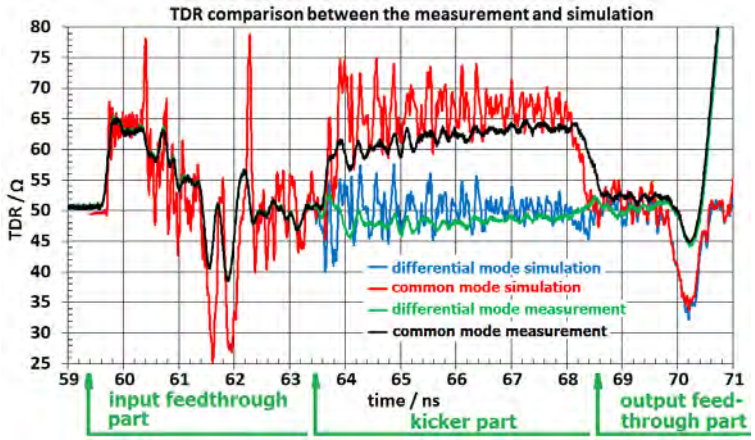

Figure 2.53. Comparison of differential-mode and common-mode TDR measurements with simulations.

Power extraction from the beam and dissipation on the electrodes and kicker housing was modeled using CST and COMSOL. Power dissipation reaches about 7.5 W per electrode at 200 mA in 48-bunch mode, almost twice that should the bunch-lengthening system not perform. Without radiative cooling, the temperature of the electrodes may rise by more than 100°, a value deemed too high. Metal-oxide blackening will be applied to the electrodes and the kicker housing of the production units to increase radiative cooling, this is expected to reduce the temperature rise by a factor of 2.

2-3.6.7 Fast High-Voltage Pulser

Overall specifications for the high-voltage pulsers that drive the stripline kickers are listed in Table 2.32. The specifications are based on a 324-bunch fill pattern.

Table 2.32. Fast pulser specifications.

Parameter	Value	Unit
Maximum effective output voltage per channel	20	kV
Dual outputs	± polarity	
Maximum pulse width (2.5%–97.5%)	16.9	ns
Maximum pulse tail amplitude	2.5	%
Amplitude stability	1	%
Maximum output time jitter to external trigger (rms)	0.05	ns

The pulse shape can be trapezoidal or quasi-Gaussian. Pulsers of either type have been prototyped and tested at APS. The waveforms in both cases fulfilled the specifications given above. In each case the key timing criterion is that start-to-end, the total pulse length should be short enough to not unduly disturb the upstream and downstream bunches. Reference pulse shapes will be given to

the vendors.

Reliability and post-purchase support is a significant concern and subject to ongoing evaluation.

2-3.6.8 Pulser Timing

Figure 2.54 shows a block diagram of timing for extraction/injection. The kicker triggers will be generated by precision delay generators, such as the Stanford Research DG645. This particular device provides four pulsed outputs suitable for driving four dual-channel pulsers. The four dual-channel extraction- and injection-kicker pulsers will each be driven by a single four-channel delay generator. A timing reference from the APS injection timing system provides the trigger for the two delay generators.

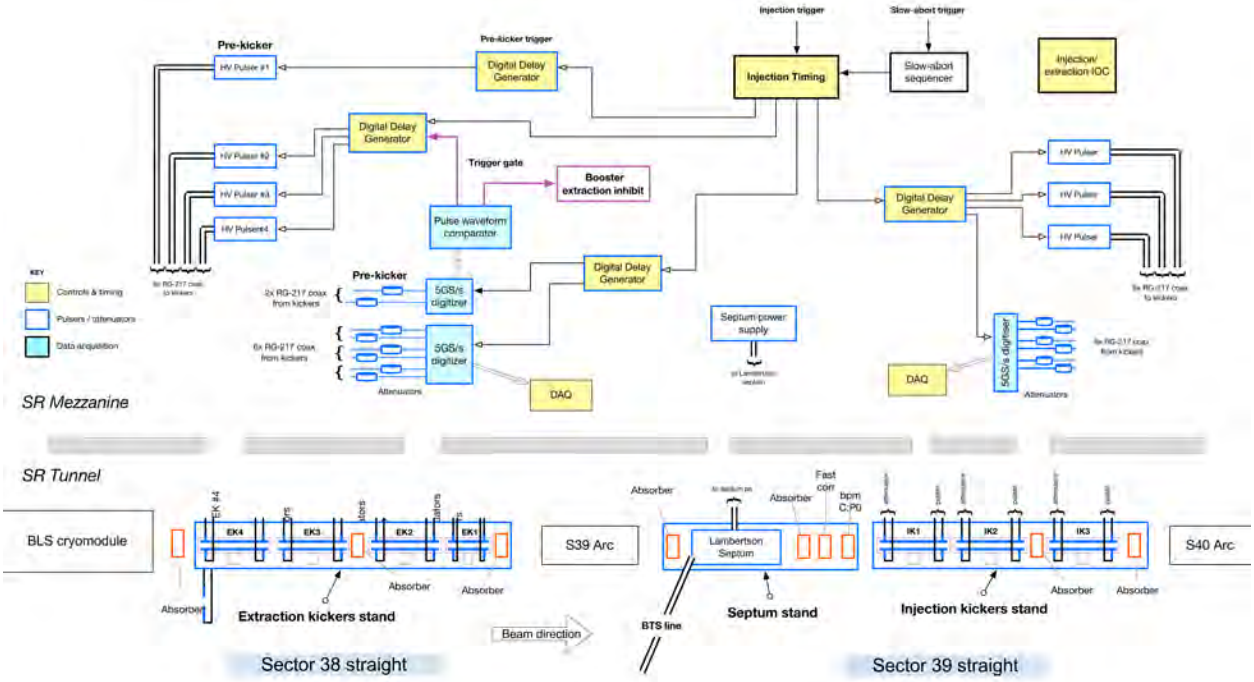

Figure 2.54. Extraction/Injection block diagram, showing timing.

2-3.6.9 Prototype Kicker Tests

Beam tests have been performed with the prototype kicker installed in the booster extraction test line (BTX) line using two different FID pulsers. Preliminary results up to the nominal working voltage of ±15 kV were previously reported[5].

Beam deflection in microns as a function of kicker amplitude met expectations. The measured kick angle at ±15 kV was 0.66 mrad for 7 GeV beam (0.77 mrad scaled to 6 GeV).

2-3.6.10 Injection / Extraction Systems Documents

The ICMS document numbers for engineering specifications, interface control documents, and final design review reports are shown in Figure 2.55.

Item Type	Engineering Specification Document (ESD)	Interface Control Document (ICD)	Final Design Review (FDR) and Review Report
Pulsed Injector Kicker Systems	apsu_2032667	*apsu_2012670*	apsu_2032308
Kicker Mechanical Systems	*apsu_2012669*	*apsu_2012668*	
Lambertson Septum	apsu_2011045	apsu_2011044	apsu_2028846
Injection/Extraction Systems	*apsu_2012672*	*apsu_2012670*	apsu_2032308
Injection / Extraction Controls	apsu_2012214	apsu_2012215	

Figure 2.55. Document set for Injection / Extraction systems.

References

[1] Thomas E. Fornek et al. *Preliminary Design Report for the APS Upgrade Project*. Tech. rep. APSU-2.01-RPT-002. APS, 2017 (cit. on p. 77).

[2] C.Y. Yao et al., Argonne National Laboratory, unpublished information, 2016 (cit. on p. 78).

[3] www.cst.com. *CST Microwave Studio Suite*. 2013 (cit. on p. 80).

[4] C. Yao X. Sun. "Simulation Studies of a Prototype Stripline Kicker for the Aps-Mba Upgrade." In: *NAPAC16*. WEPOB14. 2016 (cit. on p. 80).

[5] C. Yao et al. "Preliminary Test Results of a Prototype Fast Kicker for Aps Mba Upgrade." In: *NAPAC16*. WEPOB24. 2016 (cit. on p. 82).

2-3.7 Orbit Positioning and Stabililization

2-3.7.1 Introduction

An ultra-stable orbit will be essential for taking advantage of the MBA beam properties, and with extremely small transverse beam dimensions (Table **??**), tolerances for orbit stability and drift are very challenging. Relative to what is achieved at the APS today, improvements are necessary in the measurement of the beam trajectories (especially long-term drift) and the effectiveness of the orbit feedback system.

General considerations for orbit positioning and stabilization are:

- During initial commissioning, obtain trajectory for the first several turns in order to close the orbit, store beam, and allow correction of the optics.
- Stabilize the particle beam at x-ray source points within a fraction of the beam size, both AC and long-term (days / weeks).
- Recover the orbit through the ID straight sections after machine maintenance / studies periods in order to restore x-ray source positions within a fraction of the beam size.
- Center the particle beam in the lattice multipole magnets at the level of a few tens of microns.

2-3.7.2 Beam Stability Tolerances

Shown in Table 2.33 are the beam stability requirements for the APS-U storage ring. These are stated in terms of AC rms orbit motion from 0.01-1000 Hz and long-term drift (anything slower than 100-second period). It is anticipated that most user applications would be insensitive to orbit motion at higher frequencies.

Table 2.33. Beam stability tolerances at insertion device source points

Plane	**AC rms Motion (0.01-1000 Hz)**		**Long Term Drift (7 Days)**	
Horizontal	1.3 μm	0.25 μrad	1.0 μm	0.6 μrad
Vertical	0.4 μm	0.17 μrad	1.0 μm	0.5 μrad

A more detailed discussion on beam stability tolerances can be found in the Physics section of this report in section 2-2.2.

2-3.7.3 Orbit Feedback System

The design for the APS-U fast orbit feedback system (FOFB) uses the same architecture as the present APS RTFB. A feedback controller (FPBC) is located in every odd-numbered sector (20 FBCs total). The feedback controllers receive bpm values from local bpm processors turn by turn, and pushes them to the fast data network for distribution to the 19 other feedback controllers. There are 560 bpms in total. Every 44.1 μsec, the feedback controllers read the latest orbit vector from the fast data network and computes and distributes new setpoints to both fast and slow correctors in its double-sector. In total, there are 160 fast (wide-bandwidth) correctors and 320 slow correctors

per plane. A block diagram of the feedback controllers is shown in Figure 2.56.

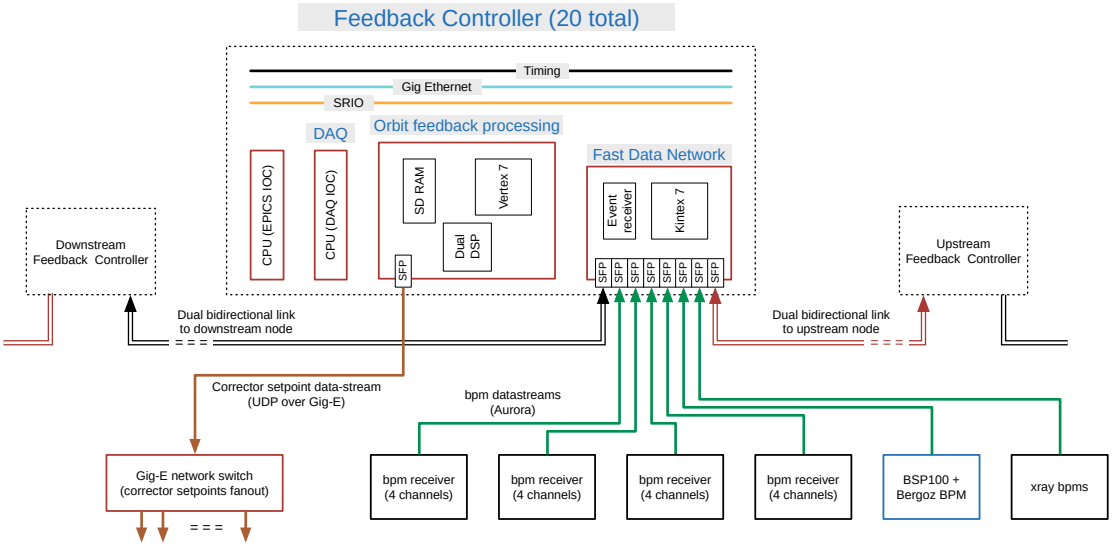

Figure 2.56. Fast orbit feedback controller.

The most-recent BPM values are streamed turn-by-turn over serial fiber links. There is one link per bpm processor (corresponding to four bpms in both planes).

The fast data network links the feedback controller with its upstream and downstream neighbors over dual bidirectional synchronous high-speed serial data links. Together, the interconnection of twenty feedback controllers forms a redundant birectional ring with a maximum of nine 'hops' between any one FBC and all others. BPM data is distributed and pushed to DSP local memory every 7.36μsec.

The DAQ gives access to timestamped synchronous data from all feedback controllers. BPM data is collected turn-by-turn, while other channels are collected once per 44.1μsec tick.

The goal for APS-U is to achieve a closed–loop bandwidth of ∼1 kHz with sufficient spatial resolution to independently control each x-ray source-point. Key differences between the APS-U FOFB and the present RTFB include:

1. Four fast correctors per sector instead of one, which allows independent control of position and angle at every source-point (see Figure 2.57).
2. A single unified orbit feedback system using all fast and slow correctors.
3. An orbit correction sampling rate of 22.6 kHz instead of the present 1.6 kHz.
4. New corrector magnets and power supplies with fast response and wide bandwidth.

Table 2.34 compares the APS-U parameters with the present RTFB/Datapool system.

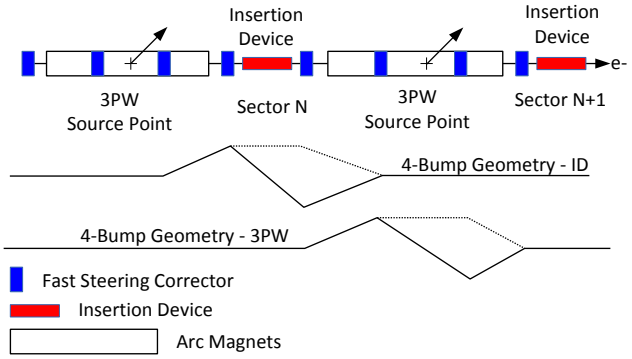

Figure 2.57. Orbit feedback spatial requirements - two correctors between adjacent x-ray source-point are needed to control position and angle independently.

Table 2.34. Comparison of orbit feedback system parameters

Parameter	**APS-U** Unified-RTFB	**Present APS** RTFB	Datapool
Revolution frequency	271 kHz	271 kHz	271 kHz
BPM sample rate	Turn-by-turn	1.6 kHz	10 Hz
BPM orbit vector distribution rate	Turn-by-turn (goal)	1.6 kHz	10 Hz
Fast corrector setpoint update rate	22.6 kHz	1.6 kHz	10 Hz
Rf bpms (per plane)	570	160	360
ID X-ray bpms (per plane)	90	-	50
Fast correctors (per plane)	160	38	-
Slow correctors (per plane)	320	-	300
Closed-loop bandwidth	DC – 1 kHz (goal)	1 Hz – 80 Hz	DC – 1 Hz

2-3.8 Diagnostics

2-3.8.1 Diagnostic Systems Overview

Diagnostics for the MBA lattice will feature major upgrades to rf and x-ray bpm systems, a new beam size monitoring system, and updates to many existing legacy systems already installed in the storage-ring, as summarized in Table 2.35. The largest systems are the rf and x-ray bpms, with the significant addition of a mechanical motion sensing system to correct for long-term drift and low frequency chamber vibration. The bpm and mechanical motion systems will be used together with a new realtime orbit-feedback system with a factor of 10 higher closed loop bandwidth and integration of both slow and fast correctors into the feedback algorithm. Legacy systems, such as current monitors and the multi-bunch feedback system, will be updated to meet requirements.

Steering through the centers of the quads will be critical, and requires 12 rf BPMs in the arcs sector. There will be an additional two high-quality rf bpms at the ends of the insertion device (ID) straight sections, and three for canted undulator straights, and two additional hard-x-ray bpms and associated x-ray intensity monitors in each high-heat-load front-end. The first optic enclosure exit mask outside the shield wall will be similarly instrumented for flux and white beam position monitoring. Canted undulator beamlines will have four x-ray bpms in their front-ends.

Table 2.35. MBA diagnostic systems

Diagnostic System	Quantity/Sector	Total
Arc rf bpms	12	480
ID rf bpms ([A,B]:P0)	2	80
ID x-ray bpm electronics (non-canted)	2	50
ID x-ray bpm electronics (canted)	4	40
ID x-ray-intensity monitor	2	70
BM x-ray bpm electronics	2	52
Mechanical-motion systems	1	35
Beam-size monitors		3
Fast orbit-feedback system		1
Transverse multi-bunch feedback system		1
Current monitors		2
Bunch-current monitor		1

The in-tunnel x-ray diagnostics components and their electronics are considered part of the front-end. One RF cavity section (A:M1 source) will be used for a high-resolution absolute beam-size diagnostics to measure the achieved emittance in both x- and y-planes. One additional RF cavity section and one BM front end will be used for relative beam-size monitors to provide fast beamsize data for automated feedback control of beam sizes in x- and y-planes. A mechanical motion sensing system comprising hydrostatic-level sensors to assure long-term beam alignment of the accelerator in relation to the beamline axis. The mechanical motion system will monitor the position of rf bpm straddling the ID vacuum chambers and x-ray bpms in the associated front-ends.

The following existing storage ring systems will be upgraded to satisfy MBA requirements:

- A fast multi-bunch transverse feedback system will be required in order to increase beam

lifetime and monitor betatron tunes.
- Two current-monitors will be required: an average-current monitor and a bunch-current monitor for monitoring the current in individual bunches during swap-out injection.
- A beam-loss monitoring system, adapted from an existing system, will be installed in the storage-ring enclosure for monitoring losses in the high-charge (up to 20 nC/pulse) bunches coming from the injector.

2-3.8.2 RF Beam Position Monitors

RF bpms provide the primary measurement of the electron beam trajectory through the insertion device (ID) straight sections and in the storage ring arcs. Each sector will contain 12 bpms in the arcs and 2 additional rf BPMs at the ends of the ID straight section. The baseline design utilizes 400 high-resolution BPMs with commercial electronics. The less critical locations will re-use 160 existing BPM processors from the present APS storage-ring. The plan also includes the installation of 40 new shielded EMI cabinets for BPMs, and feedback electronics, and new heliax cables.

The new BPM assembly has been designed in coordination with the vacuum design group[1]. The BPM assembly features integrated shielded bellows on both flanges and pick-up electrodes that are welded to the stainless steel body. The button electrodes are 8 mm in diameter and the vacuum chamber is 22 mm in diameter.

In order to achieve the beam stability goals, low noise BPM electronics are essential. APS-U has opted to use commercial BPM electronics for preliminary design that meet the demanding beam stability requirements shown in Table 2.33. Each BPM processor, as shown in Figure2.58, consists of four channels of BPM button electrode inputs, a timing module, Software/EPICS IOC, Fast data stream (FDS) packet structure, and a Gigabit Data Exchange (GDX) module for interfaces to the feedback controller (FBC) and machine protection interlock [2].

Figure 2.58. Commercial BPM processing electronics.

The commercial BPM processors show excellent noise performance, approaching 2 nm/$\sqrt{\text{Hz}}$, and long-term stability at the level of 200 nm peak-to-peak over a 24-hour period[3]. The commercial BPM processors satisfy the APS-U's long-term and AC beam-stability requirements [4] as measured in the APS storage ring and extrapolated to APS-U BPM design.

2-3.8.3 Beam Size Monitor (BSM)

We plan to build one absolute beam size monitor for reliable emittance measurements and one or two relative beam size monitors for automatic feedback control of beam emittance and for measurements of beam energy spread. Table 2.36 summarizes the available sources for the APS-U beam size monitors. The tabulated data shows: (1) The most suitable source for the emittance measurements is the A:M1 source, accessible from all ID ports. Its horizontal size is determined by the beam emittance with negligible contribution from the energy spread, and the A:M1 source sizes are proportional to the ID source sizes used by most APS users. (2) The bend magnet source B:M3 is not optimized for either emittance nor beam energy spread measurements, but is sufficient for relative beam size measurements. Its advantage is the ease of access from many unused BM front ends.

Table 2.36. Electron Beam Sizes in APS-U Storage Ring Sources

Source	B:M3	A:M1.1	ID (ref)
Access port	BM	ID	ID
Observation angle in beamline (mrad)	-2.2	-1.5	0.0
Horizontal beta functions (m)	0.70	1.63	4.94
Vertical beta functions (m)	4.85	19.85	1.89
Horizontal dispersion (mm)	3.1	0.26	0.57
Energy spread in Timing Mode (%)	0.156	0.156	0.156
Horizontal emittance in Timing Mode (pm)	31.9	31.9	31.9
Horizontal beam size from emittance (μm)	4.7	7.2	12.5
Horizontal beam size from energy spread (μm)	4.9	0.4	0.9
Total horizontal beam size (μm)	6.8	7.2	12.6
Vertical emittance in Timing Mode (pm)	31.7	31.7	31.7
Vertical beam size for Timing Mode (μm)	12.4	25.1	7.7
Vertical emittance in Brightness Mode (pm)	4.2	4.2	4.2
Vertical beam size for Brightness Mode (μm)	4.5	9.1	2.8

To avoid competing for precious insertion device real estate, we will use one or two ID ports in the RF sectors (No. 36 - 40), or more precisely AM ports, one for absolute beam size monitor (ABSM) and the other for relative beam size monitor (RBSM). The large vertical beam size is highly beneficial for relative BSM to provide stable coupling information. We will also use one BM port to take light from the B:M3 source and measure the beam energy spread (absolute horizontal beam size), and relative changes of horizontal and vertical beam sizes. While the relative BSM beamlines will be entirely contained in the tunnel, the absolute BSM beamline will be extended into the experimental floor by drilling through the tunnel wall, and building a shielded station on the experimental floor. The extension is necessary for suitable optical magnification and adequate space for monochromators and high-resolution imaging detectors.

Table 2.37 lists the lattice functions and expected e-beam sizes at the A:M1 source points. During

normal operations, the beam sizes are between 7 μm and 25 μm. We need to develop absolute beam size monitors with 3.2 μm rms resolution with a possible future upgrade to support low-coupling studies and operations. The required resolution for the absolute beam size monitor is defined by the criterion that the increase of measured beam sizes due to finite imaging resolution should not exceed 10% of the actual beam sizes: $\sqrt{\sigma_e^2 + \sigma_r^2} < 1.1\sigma_e$, where σ_e and σ_r are the rms e-beam size and monitor resolution, respectively. To support an automatic feedback system for stabilizing beam sizes, we also plan to develop relative beam size monitors with 7 μm rms resolution, which provide stable, adequate signals for feedback system with the bandwidth of 1 Hz or better. Table 2.38 summarizes the beam size monitor resolution requirements. In the following subsections, we will describe the designs of the beamline on the ID ports. The design of the BM relative BSM beamline will differ only slightly.

Table 2.37. Electron Beam Sizes and Monitor Resolution Requirements for A:M1 Source

	Horizontal		**Vertical**	
Beta functions at A:M1 source (m)	1.63		19.85	
APS-U operating mode	Timing	Brightness	Timing	Brightness
Emittance (pm)	31.9	44	31.7	4.2
Beam size (μm)	7.2	8.5	25.1	9.1
Resolution for 10% error (μm)	**3.2**	3.7	10.9	4.0

Table 2.38. Beam-size-monitor resolution requirements

Monitors	**Absolute beam-size monitor**	**Relative beam-size monitor**
Quantity	One	Two
Port (tentative)	37-ID	40-ID and 32-BM
Resolution	3.2 μm	7 μm
Bandwidth	$>$ 0.01 Hz	$>$ 1 Hz
Notes	Beam-size uncertainty $<$ 10%	Feedback-control of beam sizes

2-3.8.4 Mechanical Motion Monitoring

A Hydrostatic Leveling System (HLS) measures the relative ground motion between the two insertion device (ID) rf BPMs and the GRID X-ray BPM location in the APS accelerator tunnel. The fundamental principle of the HLS [5] is that any fluid seeks its own level. Given a set of reservoirs connected by a half full pipe or tube, the fluid level in each reservoir will be at the same absolute elevation, determined by the balance between gravity and air pressure. For small systems, the absolute elevation can be relative to some reference such as mean sea level. For larger systems, the curvature of the earth and other gravitational effects need to be considered. Given a reference point, such as the bottom or top of the housing, the relative level of the fluid will vary as the sensor is moved up or down with respect to all the other sensors.

Included in the design are 105 in-tunnel hydrostatic detectors located at the ID P0 rf BPMs and GRID BPM locations. These detectors will measure ground motion and be used to compensate for localized ground motion in each of the 35 locations in sets of three.

2-3.8.5 Current and Loss Monitoring

Two diagnostic systems that are currently deployed at the APS will be reused or upgraded for the MBA ring. These systems include current monitors and beamloss monitors. Both systems must be able to operate with 200 mA, which is double the present SR average current. Due to the new vacuum chamber dimensions, new current monitor DCCTs will need to be purchased from a commercial vendor.

We plan on reusing the existing beamloss monitors which will save significant engineering time and costs. We will need new hardware to mount the detectors to the storage ring chambers and new high-voltage and signal cables.

2-3.8.6 Diagnostics Documentation

The ICMS document numbers for engineering specifications, interface control documents, and final design review reports are shown in Figure 2.59.

References

[1] Robert Lill Xiang Sun and Benjamin Stillwell. *Simulation Comparison between the Baseline and the Vendor Designs of the MBA BPM Button*. Tech. rep. AOP-TN-2016-006. APS, Sept. 2016 (cit. on p. 88).

[2] Instrumentation Technologies. *Libera Brilliance+*. http://www.i-tech.si/accelerators-instrumentation/libera-brilliance-plus/ (cit. on p. 88).

[3] G. Rehm. "Recent Development of Diagnostics on 3rd Generation Light Sources." In: *Proc.of EPAC 1908*. 2008, pp. 1016–1020 (cit. on p. 89).

[4] R. Lill A. Brill H. Bui and N. Sereno, Argonne National Laboratory, unpublished information, 2015 (cit. on p. 89).

[5] J Volk et al. "Hydrostatic level sensors as high precision ground motion instrumentation for Tevatron and other energy frontier accelerators." In: *Journal of Instrumentation* 7 (2012) (cit. on p. 90).

Item Type	Engineering Specification Document (ESD)	Interface Control Document (ICD)	Final Design Review (FDR) and Review Report
BSM	apsu_2012449	apsu_2012283	
Shielded EMI Cabinets	apsu_2014543	apsu_2012719	apsu_2032035
BPLD	apsu_2012451	apsu_2012175	
DCCT	apsu_2012448	apsu_2012186	
RF BPM	apsu_2012445	apsu_2012170	apsu_2031694
Transverse feedback system	*apsu_2032665*	apsu_2032666	
Mechanical Motion System	apsu_2012447	apsu_2012212	
FOFB (RTFB)	apsu_2012446	apsu_2012226	
Stored Beam Monitor (Top-Up Monitor)	apsu_2012450	apsu_2012275	

Figure 2.59. Diagnostics Documentation.

2-3.9 Accelerator Control System

2-3.9.1 Overview

The APS-U design retains a large fraction of the present controls core infrastructure and high-level applications. This includes EPICS core software and extensions, physical infrastructure of network switches and VME crates distributed around the ring, Main Control Room (MCR) scripts, GUI screens, and high-level applications; largely built using SDDS and tcl/tk toolkits.

Specific enhancements are necessary, however, to meet the requirements of the state-of-the-art technical systems which are a part of the APS-U accelerator. Several of these challenges and the design approach to address them are listed in Table 2.39. Significant consideration must be given to the short amount of time allocated to system integration and machine commissioning. This places additional demands on the control system tools to facilitate efficient testing, troubleshooting, ad-hoc generation of scripts, and deployment of modified software in an effective manner. Such capabilities must be part of the control system design from the beginning.

Table 2.39. MBA Control System Challenges and Associated Design Goals

Control System Challenge	Design Goal
Ubiquitous embedded IOCs, FPGA-based controller, network appliances	Network infrastructure design which separates classes of traffic
Substantial increase in number of network ports	Accommodate in network infrastructure design
Substantial increase in network traffic and throughput requirements	Separate Data Acquisition (DAQ) System specifically for fast time-correlated data
All accelerator components on-site before installation begins	Deploy Component Database early
Short commissioning time	Early deployment of "virtual subsystems" for test script development
Expectation of high availability soon after commissioning	Built-in diagnostics and exhaustive first fault identification

Components of the control system can be largely grouped into three initiatives:

- Control System Infrastructure (including Timing)
- Control System Applications and Services
- Interfaces to Technical System

2-3.9.2 Control System Infrastructure

The control system infrastructure provides the primary communication and synchronization betweenthe software tools and the technical system components. It is comprised of the network switches, timing and event hardware, distributed VME and microTCA crates, and several linux clusters supporting softIOCs and other services. It is this infrastructure that allows the diverse technical systems to be integratedand controlled as a single MBA accelerator.

2-3.9.2.1 Timing and Event System The existing APS Event System is capable of generating events with 0.1 microsecond resolution andEPICS timestamps with a resolution of 1 microsecond. There are over 160 installed components that utilize this event system across the APS complex. For many applications, this system still provides sufficient capability and it will continue to be used as long as the custom hardware can be supported. A more modern event system from MicroResearch Finland (MRF) will be deployed in parallel to the original APS Event System to support requirements of more precise event timing and higher-resolution timestamps (e.g. timestamping of turn-by-turn data). Deploying this "de facto standard"MRF event system allows us to take advantage of work at other labs (e.g. event receiver FPGA IP) and capabilities within commercial equipment (e.g. the I-Tech Libera Brilliance+ BPM processor has a built-in MRF receiver that can be used for synchronization across many units).

2-3.9.2.2 Double-sector Configuration. As a base controls infrastructure for the MBA storage ring, the following hardware will be installed at each double-sector to provide distribution and interface points for controls provided functions:

- Two Tier 3 network switches, each providing 48 ports
- A VME-based IOC to support the plethora of legacy custom VME modules developed for APS; delay modules, fiber fanouts, fiber-to-electrical converters, etc.
- MPS Input Modules (provides interface points for technical systems that must trip the MPS)
- An MRF Event Receiver and/or an MRF Event Fanout module
- A bank of Ethernet-to-serial devices for interfacing to technical system hardware
- A Diagnostics-owned μTCA chassis in every double-sector will house the fast orbit feedback processors and other diagnostic equipment, and will also house modules for the DAQ front-ends.

2-3.9.2.3 EPICS IOC Software & Development Environment. EPICS IOCs and services developed for the APS-U will use the standard EPICS build environment to build the IOC and related software programs, based on the IT Group's standard Red Hat Enterprise Linux platform wherever possible. In addition to the familiar EPICS V3 (currently EPICS 3.15) capabilities, some IOCs will utilize EPICS V4 features to provide the necessary functionality. The combination of EPICS V3 and V4 is often referred to as EPICS V7.

2-3.9.2.4 Data Acquisition (DAQ) System. Subsystems that can influence the beam (e.g. RF, feedback, magnet power supplies, kickers) will have a DAQ IOC to aide fast determination of beam anomalies. Each DAQ IOC must obtain fast sampled data from the technical system along with an accurate timestamp of when each sample was taken. The DAQ IOCs can take short snapshots of this data or it can be streamed continuously to a service that will either process the data or save it to disk (or both).

DAQ IOCs will be attached to a separate VLAN to ensure the high data demand does not impact routine machine control. Table 2.40 shows the technical systems currently identified as requiring this DAQ capability.

Table 2.40. Technical Systems with DAQ Interfaces

Technical System	# of Nodes	Signals per Node	Sample Rate	Data Rate per Node
RF BPMs (Turn-by-turn)	20	30 BPMs x 2 planes	271KHz	65MB/s
X-Ray BPMs	20	5 BPMs x 2 planes	10KHz	0.4MB/s
Fast Orbit Feedback	20	100 signals	22.6KHz	9MB/s
Power Supplies (all types)	20	140 supplies x 3 values	22.6KHz	38MB/s
Injection/Extraction Systems	1	8 waveforms	4GHz	3.2KB/s
SR/Booster RF	3	12 cavities x 3 values	271KHz	39MB/s
Bunch Lengthening System	1	5 values	271KHz	5.4MB/s

2-3.9.2.5 Network. A significant requirement for the MBA control system is the need to accommodate ubiquitousIOCs and numerous FPGA-based controllers embedded within the technical systems. This puts a demand on the network infrastructure in terms of number of ports and the increased bandwidth for high data rates and large volumes of data.Figure 2.60 illustrates a network topology that will provide for these demands as well as allowing scaling of the network should requirements grow.

The key aspects of the illustrated network infrastructure are:

- Redundant connections from the Tier-1 switches to Tier 2
- Redundant connections from the Tier-2 switches to Tier 3
- 1/10Gbps ports at all Tier-3 switches (a Tier-3 switch every double sector)
- Each Tier-3 switch provides 48 ports. These switches can be "stacked" to provide additional ports when required.

The use of VLANs (Virtual LANs) will assist in separating network traffic for consistent and reliable operation. Routine control and monitoring will be isolated from the fast DAQ data and bulk data transfers. Other VLANs will be used for maintenance activities, untrusted network devices, and I/O subnet devices. APS-U is responsible for part of the scope shown in Figure 2.60, with the remainder being part of the facility infrastructure. Responsibilities are described in a high-level MOU between APS-U and the APS facility.

2-3.9.3 Database Applications - Component Database (CDB)

A Components Database and electronic traveler system will track all components during procurement, fabrication, inspection/test, and installation. The component database (CDB) contains an 'MBA Component Catalog' where each component type will be identified and linked to drawings, documentation, vendors, and the component's unique properties. Each fabricated or procured component will have a unique identification number encoded on a QR code attached to the component.

Based on experience with the existing APS, the number of process variables for the MBA will likely exceed 500,000. An application that automatically defines EPICS records from data in the Component Database (and other sources) will greatly minimize the number of errors compared to a manual database definition process and will be pursued. Additional capability to request or discover

the appropriate PVs associated with certain machine components by technical system, component families, or by using wildcards will allow efficient development of other applications

2-3.9.4 Control System Engineering Applications

Due to the short installation, integration, testing, and commissioning time of the MBA, the technical system engineers require mature and flexible tools to quickly bring up their systems to full capability and reliable operation. Necessary tools include the Data AcquisitionSystem (DAQ) services, management of calibration/characterization data, PV finder, high performance archiver, interactive debugging tools (strip chart, arbitrary PVtable, camonitor, etc.), and an infrastructure monitoring system (for an early indication of a potentially hidden problem). Additionally, tools for subsystem integration testing, non-beam system checkout, and integration with AOP commissioning tools will be required.

A vast library of custom high-level applications, controls GUIs, and scripts have been developed over the past 20 years and are in routine use in the Main ControlRoom (MCR). These tools will continue to be used as they are very familiar to the operations group. In addition, the suite of high-level tools will be expanded to include utilities and libraries that are more familiar and more accessible to the engineering groups for rapid development of ad-hoc engineering applications. Octave (an open-source equivalent to Matlab), python and ipython/Jupyterare favored candidates (EPICS V4 has a mature API for python). Availability of hooks into SDDStools and use of SDDS data formats are an explicit requirement.

2-3.9.5 Technical Systems Interfaces

A substantial fraction of the APS-U controls work will be reconfiguring the control system and controls applications to switch from the existing to the new technical equipment. Associated IOC databases, controls applications, and accelerator/operations high-level applications must point to the new equipment.This effort involves changing physical interfaces to several thousand technical components and several hundred-thousand EPICS process variables (PVs). A listing of the technical systems to be addressed is in Table 2.41. All the work to integrate the new systems and maintain the functionality of the existing systems through the installation year is part of the APS-U effort.

To the extent possible, EPICS databases, control screens, and physical/functional interfaces to new storage-ring technical equipment will be debugged offline during the pre-installation phase. Where it is not possible to use the actual equipment,'virtual' accelerator systems will be built to expedite testing and debugging of the more important systems. The 40-fold symmetry of the storage-ring means that much of the process of instantiation can be automated once databases for a single sector have been configured and debugged.

An important scheduling issue is that a large fraction of the control-system activities need to occur earlier than the corresponding activities for other technical systems. In particular, every technical group relies on the control system for testing and operating their equipment.

Table 2.41. Technical Systems with predominantly new hardware

Technical System	Primary Interface	Timing Req'd	DAQ Interface
Fast Orbit Feedback	Ethernet	Yes	Yes
Machine Protection System	Backplane	TBD	No
Libera BPMs	Ethernet	Yes	Yes
X-Ray BPMs	Ethernet	Yes	Yes
Beam Position Limit Detectors	Backplane	No	No
Beam Size Monitors	TBD	No	TBD
Mechanical Motion Systems	Ethernet	No	No
Current Monitors	Backplane	Yes	TBD
Transverse Feedback System	Ethernet	Yes	TBD
Injection/Extraction Systems	Ethernet	Yes	Yes
Booster/SR Synchronization	TBD	Yes	No
Longitudinal Feedback System	Ethernet	Yes	TBD
SR RF Upgrade	Backplane	Yes	Yes
RF Bunch Lengthening System	Ethernet	TBD	TBD
Bipolar Power Supplies	Ethernet	No	Yes
Unipolar Power Supplies	Ethernet	No	Yes
Vacuum Valves and Monitoring	Ethernet	No	No
Water Systems	Ethernet	No	No
Cryo Plant	Ethernet	No	No
Beamline Timing and RT Data Distribution	Ethernet	Yes	No

2-3.9.6 Controls Support for Machine Testing and Commissioning

In typical accelerator construction projects, tools to support high-availabilityoperation, such as exhaustive diagnostic information and post-mortem analysis, evolve during the operational period of the facility. Due to the short turn-on time of the MBA after installation, such tools must be available at the initial testingphase to provide quick determination of failures or performance problems.The virtual accelerator systems mentioned earlier will be used to develop and debug these tools prior to the installation of the machine.

2-3.9.7 Control System Documentation

The ICMS document numbers for engineering specifications, interface control documents, and final design review reports are shown in Figure 2.61.

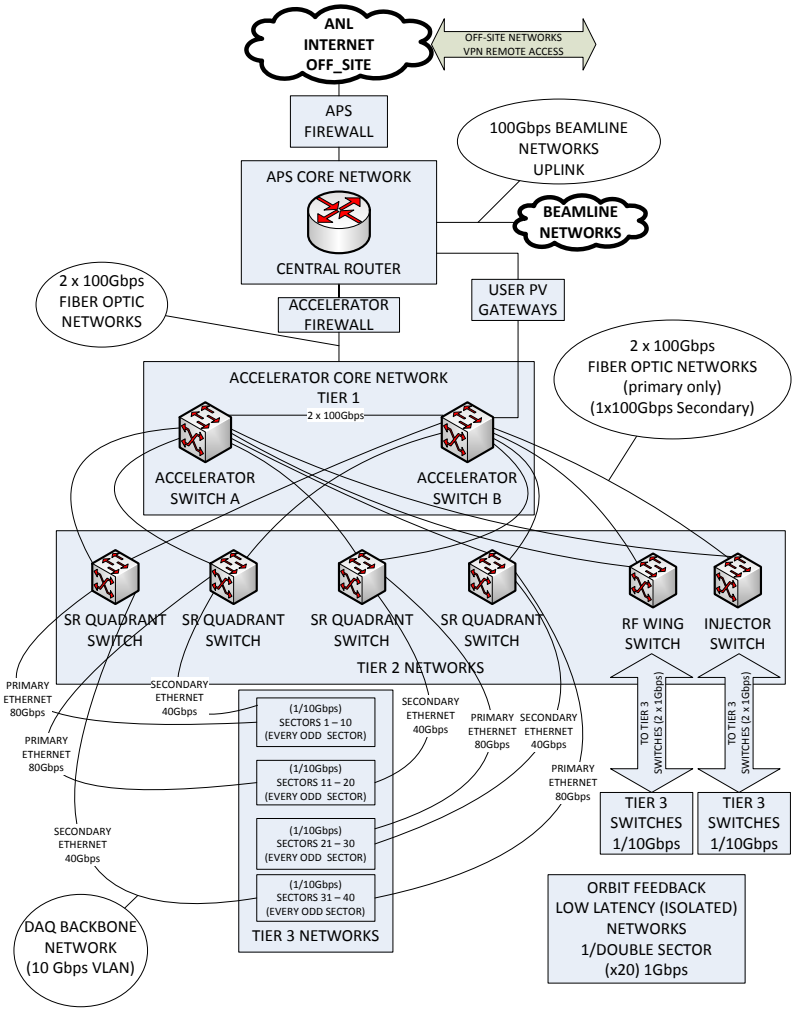

Figure 2.60. Controls networks topology.

Item Type	Engineering Specification Document (ESD)	Interface Control Document (ICD)	Final Design Review (FDR) and Review Report
Machine Protection System (MPS)	apsu_2012217	apsu_2012218	
DAQ	apsu_2012209		
IOC Development deployment infrastructure	apsu_2012213		
Controls Hardware Infrastructure	Planned future	apsu_2012456	
Hi-level Engineering Tools	apsu_2012210	NA	
CDB	apsu_2012208	NA	
eTraveler		NA	
Injection / Extraction Controls	apsu_2012214	apsu_2012215	

Figure 2.61. Control System Documentation.

2-3.10 Main Ring Rf System

The 41 pm lattice of the MBA ring has an energy loss per turn of 2.74 MeV at 6 GeV beam energy. Adding 1.6 MeV for a maximum of IDs closed and 50 keV energy lost to the vacuum system results in a total energy loss of up to 4.45 MeV. At 200 mA beam current, 830 kW need to be delivered to the beam.

Four 1-MW continuous wave (CW) rf stations (RF1-RF4) power 12 single-cell copper cavities installed in groups of four in Sectors 36, 37 and 40. A fifth 1-MW rf system (RF5) is dedicated to supplying rf power to the booster rf cavities. Four rf cavities will be removed from the sector 38 straight section in order to make space available for the extraction kicker and the harmonic rf cavity of the bunch-lengthening system.

2-3.10.1 High-Level Rf System

Due to the lower electron-beam energy of APS-U, power and voltage requirements are less than at the present APS, and the MBA ring can be operated with 12 rf cavities and sufficient overhead to allow for full beam parameters even if one or two cavities have to be taken off-line for any reason. Table **??** shows the parameters for the system, with 12 cavities. These parameters are maximum values assuming a large number of IDs are closed, and provide 4.5% momentum acceptance to maximize beam lifetime. Operationally the system will often run at lower power.

Table 2.42. Requirements for main RF systems

Quantity	Symbol	Present	MBA	Unit
Rf frequency (harmonic)	h	1296	1296	
Rf frequency (main RF)	f_{rf}	351.935	352.055	MHz
Energy loss per turn w/o IDs	U_0	5.4	2.87	MeV
Energy loss per turn w/ IDs	U_1	<6	<4.47	MeV
Power loss to SR	P_b	<900	<894	kW
Bucket half-height	ϵ_{rf}	2.2	4.5	%
Rf voltage	V_{rf}	9	6.43	MV
Number of cavities	N_c	16	12	
Max. power per cavity	P	100	104	kW
Number of klystrons	N_k	2	2	
Amplitude noise	δV_{rf}	1.5	<1.5[a]	% pk-pk
Phase noise	$\Delta\phi_{rf}$	1	<0.25[a]	° pk-pk

[a] Note: Amplitude and phase jitter were measured without AM/PM suppression of AC line harmonics. Tracking simulations of rf phase and amplitude stability indicate that noise levels must be approximately a factor of ten better than at present.

A single-line block diagram of the rf power system is shown in Figure 2.62. A system of motorized WR2300 waveguide components, including four waveguide switches, four 45° phase shifters, and two waveguide shutters are utilized to quickly select one of six modes of operation. This system provides operational redundancy for both the booster and the storage ring to minimize downtime in the event of an rf station failure. The high-power configuration provide the ability to drive the sector 36 and 37 rf cavities with either RF2 or RF3 or both at an output power of up to 1.4 MW combined, thus meeting the requirement for full beam current and full rf voltage with 8 cavities

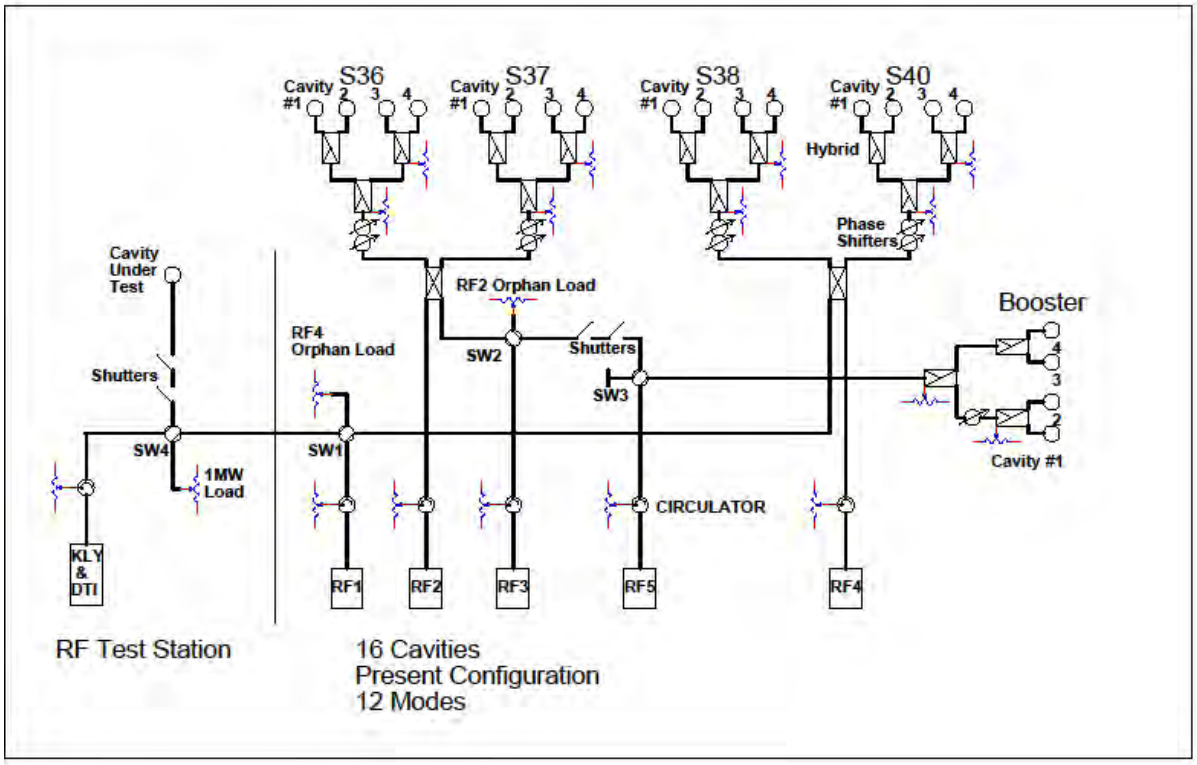

Figure 2.62. 352-MHz HLRF system configuration for MBA upgrade.

in the event that Sector 40 becomes inoperable for any reason. The Sector-40 rf cavities may be powered by either RF1 or RF4 at an output power of up to 800 kW in case of reduced power or voltage from Sectors 36 and 37 and assuming each cavity can operationally handle up to 200 kW (see section below). The ability of RF1 to provide rf power for the 350-MHz rf test stand and RF3 to substitute for RF5 in powering the booster rf cavities is preserved. Waveguide safety shutters are used in the path between RF3 and RF5 to isolate the two accelerators for personnel safety. The motorized waveguide components are directed and monitored by a central control system, which also reconfigures the LLRF system, interlock, and control signals to and from the appropriate hardware, depending on the specific operating mode selected.

2-3.10.1.1 High-Power Coupler In order to fully utilize the redundancy built into the rf system, it is required to be able to handle power in excess of the present 100 kW per cavity. A 300 kW power coupler has been developed previously in collaboration with CERN[1]; a new prototype addressing some issues uncovered at ANL is being built at CERN. The new coupler will be a 1-to-1 replacement of the existing one with minimal modifications necessary to the waveguide system. In addition, this coupler may provide a path towards improving the rf power handling in the Booster.

2-3.10.2 Low Level Rf System

A residual phase noise of 0.25° or less will be aimed for in order to prevent dipole oscillations of the bunches and to prevent excessive amplifier-power demands from the longitudinal feedback system which will detect such oscillation and try to reduce it. While some filtering is possible to reduce the signal at the low frequency (predominantly mode 0), tracking studies indicate a need for significant feedback gain even at very low frequency which would lead to amplification of the noise signals.

Mitigation of rf noise is done in a cost-effective way in the low-level rf system by a combination of feed-forward techniques—compensating, such as the ac ripple from the high-voltage power supplies that is very difficult to reduce at the source—and fast feedback techniques that suppress noise by the loop gain and reduce phase transients by stabilizing the rf voltage on a fast time scale.

2-3.11 Longitudinal Feedback System

The APS-U storage ring operates at twice the beam current of the present APS ring. At the same time, the synchrotron tune is reduced to about 620 Hz due to the lower momentum compaction and will be much lower again when the BLS is fully engaged. With these parameters, multi-bunch instability growth rates will be higher than in the present APS storage ring while at the same time the radiation damping rate will be lower due to the lower beam energy. For these reasons the need for a longitudinal bunch-by-bunch feedback system is foreseen. Detailed modelling studies of multibunch stability are described in sections 2-2.5 and **??** of this report. In studies carried out in collaboration with Dimtel, Inc.[2], the modal spectra in the present APS storage ring have been measured and their growth rates determined.

As explained in section 2-2.5, one method of reducing these growth rates is "HOM tuning" by means of changing the cavity temperature. This method is employed in the present APS storage ring, controlling the cavity temperature by sector to prevent instability due to the $m = 36$ mode

driven by the cavity HOM near 537 MHz. For APS-U, the fundamental rf frequency will be different by about 125 kHz. This changes the aliasing of the cavity HOMs to spatial beam modes as well as the frequency of the HOMs themselves but is not expected to significantly change the widths of the HOMs. The termperature coefficients of the modes will allow for accurate prediction of the spectra applicable to APS-U.

The primary parameters for the LFB system are the system bandwidth needed to damp all modes anticipated to grow, the gain necessary to reduce growth rates below the radiation damping with comfortable margin, and the maximum energy kick, which needs to be sufficient to avoid saturation due to transients and system noise at the highest gain desired. For APS-U, the system bandwidth shall be wide enough to facilitate operation at the highest number of bunches; it is chosen to cover a range from near 0 to 60 MHz which includes operation with 432 bunches—compared to the APS-U design specs of 324 bunches—to avoid limiting upgrade potential of APS-U. The maximum kick is 5.9 kV, to be achieved with two kickers, with an upgrade path to about 8.3 kV without changing the kicker structures should the need arise.

2-3.11.0.1 System Layout If it follows the now-conventional architecture, the feedback system will have a layout as shown in Figure 2.63. Signal shaping is performed in the front-end with two

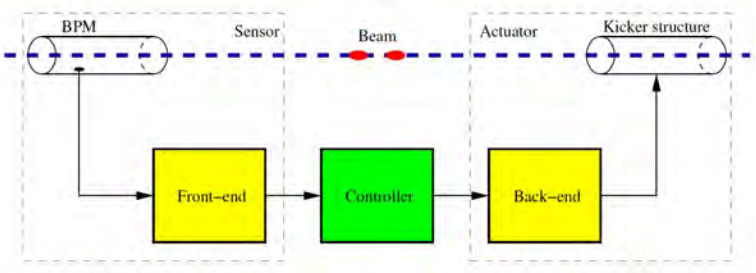

Figure 2.63. Block diagram of the longitudinal feedback system.

(competing) objectives: obtaining flat pulse top and minimizing bunch to bunch coupling. Flat pulse top is needed to reduce system sensitivity to sampling clock jitter and long term clock phase drifts. The beam signal is phase-compared with the RF master oscillator or its harmonic. Higher frequency detection provides more phase sensitivity but has lower bunch phase acceptance range. The system should operate below the TM beam-pipe cutoff frequency to avoid spurious signals due to propagating modes, which is fairly easily achieved at APS-U due to the small vacuum chamber aperture.

The baseband signal processor digitizes the processed beam phase, calculates a correction signal, and generates a baseband analog correction signal. One difficulty for such a system is that the synchrotron tune is not well defined when the BLS is tuned for optimum lifetime, which makes design of the FIR filter problematic. For this reason, tracking simulations used a different methodology, see sec. 2-2.5 for a description of the studies performed. A possible approach to this problem is described below.

The back end modulates the baseband correction signal to the operation frequency of the kicker. For APS-U, a frequency of 1.033 GHz is chosen which is suitable for all anticipated operating modes

(48 bunches, 324 bunches, and 432 bunches would be possible as well). Preliminary particle tracking studies indicated that form factor $(0.8-0.9)$ and variation in kick along the bunch for long bunches ($\Delta t \approx 250ps$) do not have a significant negative impact on system effectiveness. The signal is then fed to power amplifiers to drive the feedback kickers. For APS-U, two 500-W amplifiers per kicker are anticipated.

2-3.11.0.2 Longitudinal Feedback Kicker The feedback kicker imposes an energy kick on each bunch, thus counteracting the instability motion. Its bandwidth needs to cover the same 60 MHz range as the processing unit, but shifted up in frequency. Such kickers can be realized as a strongly damped cavity kicker[3]. For APS-U, two cavity kickers are chosen. Damped-cavity kickers have been in operation at several facilities (see e.g. [4, 5, 6]) in a frequency range similar to APS-U. A 4-port design has been carried out, with two ports being driven by the power amplifiers and two ports terminated by suitable high-power loads. Figure 2.64 shows a rendering of a design model for

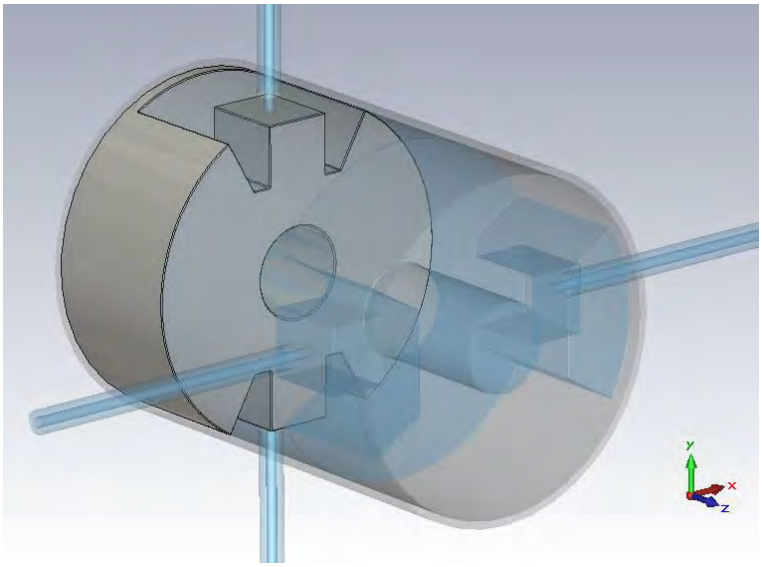

Figure 2.64. 3-d rendering of a conceptual design for the APS-U longitudinal-feedback kicker. Length of this model is 30 cm. Two of these kickers will be used in the APS-U storage ring.

the APS-U LFB kicker. Table 2.43 gives the parameters of the kicker design.

Table 2.43. APS-U storage ring longitudinal-feedback kicker parameters

Parameter	Value	Unit
Frequency	1027	GHz
R/Q	125	Ω
Q_{ext}	17.4	
Q_0	14000	
R_s	4.35	kΩ
peak Voltage	2.95	kV at 1kW power
Rf Power	2×500	W
Beam pipe diameter	22	mm
No. of ports	4	(2 driven, 2 terminated)

2-3.11.0.3 Advanced feedback topology The low synchrotron frequency of APS-U—especially with the bunch-lengthening system fully engaged—presents a challenge to the longitudinal feedback system as the 90° phase rotation in the filter takes 1/4 of a synchrotron period. A conceptually promising option to enable longitudinal feedback at very low synchrotron frequency and a wide synchrotron frequency spread is direct energy-oscillation sensing. Such a system is assumed in tracking studies of multibunch instabilities, as reported in section 2-2.5. For the horizontal difference signal of a pickup it can be shown that, for sinusoidal oscillations, the signal is given by[2]

$$x(t) = 2g(n)i_b \left(x_0 + \eta \frac{\epsilon_0}{E_0} \cos\left(\omega_s t\right) \right) \sin\left(n\omega_{rf} t + n\omega_{rf} \frac{\alpha \epsilon_0}{E_0 \omega_s} \sin\left(\omega_s t\right) \right), \tag{2.6}$$

where $g(n)$ is the pick-up gain as function of frequency, i_b, the bunch current, x_0, the orbit offset at the pickup; η is the dispersion, and ω_s and ω_{rf} are the synchrotron and the rf frequency, respectively. Detection should be performed at the lowest possible harmonic of the rf frequency; a stripline pickup of sufficient length might be needed to provide sufficient signal-to-noise ratio, especially as the maximum dispersion in the APS-U storage ring is only about 0.08 m. It is necessary to separate the amplitude modulation from the phase modulation which will also be present; this can be done with a modified front-end and by rotating the samples from Cartesian to polar coordinates in the processor. A design of a suitable front-end will be carried out in industry.

2-3.12 Bunch Lengthening System

2-3.12.1 High Harmonic Cavity and Cryomodule

A higher-harmonic cavity (HHC) system in an upgraded APS x-ray source will provide a practical benefit to the majority of APS users by increasing the beam lifetime and availability in the storage ring. As discussed in Section 2-2.7, the lifetime in the upgraded APS storage ring will be limited by the so–called Touschek effect, a result of Coulomb scattering between electrons within the beam bunch, leading to beam loss from the longitudinal bucket. From a practical standpoint, the beam lifetime after the upgrade will be signficantly shorter than the present 6-8 hours and may require injection into the storage ring more frequently than the present once per minute.

A single superconducting cavity can provide the necessary voltage in a compact footprint, $l \leq 2.5$ meters, needed to lengthen the beam bunch and increase the Touschek lifetime by 3-5 times. There are only two examples of bunch-lengthening superconducting rf (SRF) cavities used in storage rings [1] which achieve about a factor of two increase. Experimental data from these two facilities indicate that, with a well-designed system, additional lengthening may be possible. Furthermore, it is expected that the cavity and all of the subsystems will be designed and built based on technology that does not require major advances in the state-of-the-art and will not require years of development effort.

Regardless of the operating temperature, a superconducting harmonic cavity will have an intrinsic quality factor that is 3-5 orders of magnitude higher than the loaded Q required for the APS-U, which is of the order 10^5. The choice of operating temperature is therefore determined based on issues of cryogenic costs, efficiency, and margin for operations for the cavity and the helium refrigerator. Microphonics induced from helium boiling would not be expected to be an issue for any cavity operating temperature.

2-3.12.2 High-level System Parameters

The bunch lengthening system cavity is excited by the circulating electron beam in the APS-U storage ring. The beam loss power, 32 kW maximum, is extracted from the circulating 200 mA beam through a pair of fundamental power couplers located next to the harmonic cavity accelerating cell. This extracted power, together with the offset frequency of +10 kHz, as adjusted with a mechanical slow tuner, determines values for the cavity voltage and phase (detuning angle) listed in Table 2.44. We note that these are nominal values from simple analytical formulae, and that actual operating values for coupling strength and detuning frequency will likely differ somewhat from these nominal values. Intrinsic properties of the cavity geometry and peak surface and electric fields are those for a cavity with the so-called TESLA shape developed in the early 1990s for the International Linear Collider[2]. The harmonic cavity surface fields required here are modest by today's standards, so the incentive to improve performance (by perhaps 10%) through development of a more advanced shape is not strong. The TESLA shape also avoids severe multipacting, which was problematic for early cavity geometries.

Table 2.44. Nominal harmonic cavity parameters for I_{beam} = 200 mA with fundamental rf power couplers

Parameter	Value	Unit
Operating temperature	2.1	K
R_{SH}/Q	104	Ω
Cavity Q factor	6×10^9	
External Q factor	6×10^5	
Cavity resonant frequency	1408	MHz
Cavity loaded bandwidth	2.4	kHz
Detuning frequency	10	kHz
Beam-induced voltage	1.25	MV
Detuning angle	85	degrees
Beam loss power	25	kW
Cavity wall losses	1.5	W
Cavity peak surface electric field	24	MV/m
Cavity peak surface magnetic field	49	mT

2-3.12.3 Cavity Design, Fabrication, and Testing

Two Helium-jacketed Niobium cavities have been built and processed. One of these has been successfully tested at 4.5 K and 2 K temperature with rf up to 2 MV peak voltage, see Fig. 2.66. The other cavity will be tested in the APS-U cryo module.

2-3.12.4 Bunch Lengthening System Cryomodule

The harmonic cavity cryomodule shown in Figure 2.65 houses a single SRF accelerating cavity cooled by 2 K liquid helium inside an integral cavity helium vessel. The cryomodule outer vacuum vessel is fabricated from 304 series stainless steel. Inside of the lower vessel (A) is a room temperature magnetic shield (B), an 80 K aluminum heat shield (C), 80 K coolant distribution lines, thermal attachments to the heat shield, and multi-layer insulation (MLI) on both sides of the aluminum heat shield. The shields are shown at the left in Figure 2.65. Other components that are also attached to or suspended from the top lid, but are not shown in the figure include:

1. Helium feed and return
2. Helium storage vessel
3. Nitrogen feed and phase separator vessel
4. Heat exchanger and J-T valve for 2K operation
5. Upper rf power coupler
6. Cavity rf pickup
7. Slow tuner supply gas
8. Thermometers and heaters

The bunch lengthening cavity will require alignment (+/- 0.5 mm transverse) with respect to the APS-U vacuum chamber. For this purpose, the cavity will be equipped with 4 open wire targets all of which will be viewable through ports located on the end-walls of the cryomodule. The cryomodule will have all metal rf gate valves attached to the ends as shown in Figure 2.65. The design allows the complete hermetically sealed superconducting cavity assembly to drop into the cryomodule vacuum

vessel while the cavity remains under vacuum. The cryomodule, in turn, will be installed under vacuum into the APS- U storage ring.

The vacuum components of the cryo module have been delivered to ANL and are being assembled with the second cavity for a full system test and characterization well before installation in APS-U. Fig. 2.65 shows the delivered vacuum vessel at ANL.

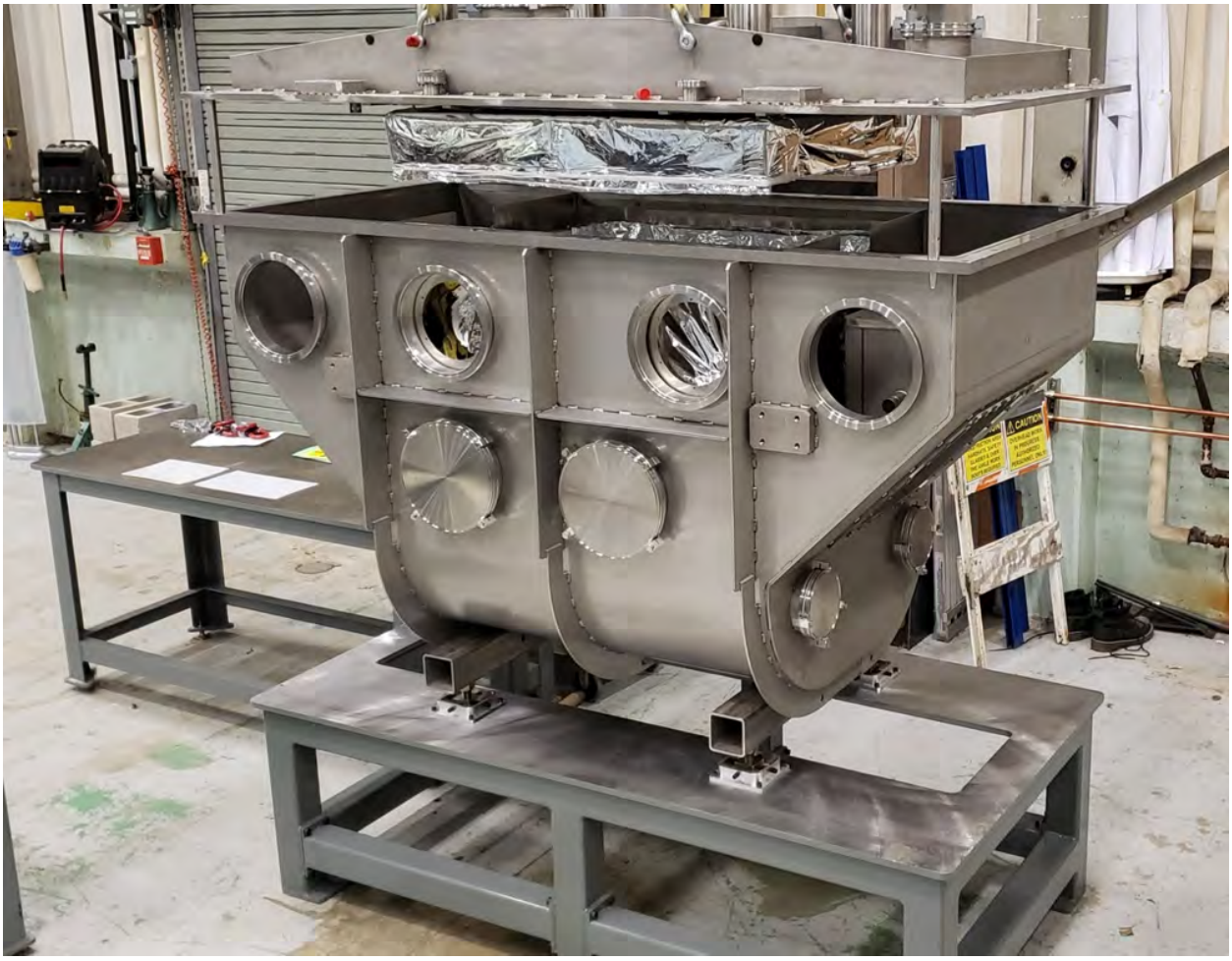

Figure 2.65. Vacuum vessel at ANL.

2-3.12.5 Cryogenic Plant

A new 4-K liquid helium refrigerator and distribution system will be purchased to provide saturated liquid helium via a low-heat-leak distribution system to the cavity and cryomodule. A schematic of the helium flow is shown in Figure 2.66. A JT-valve and heat exchanger inside the cryomodule will provide up to 50 Watts of 2.1 K helium to the cavity. For the 4 K refrigerator cold box, commercially available models near the rated capacity are available from major international manufacturers. The anticipated lead time should be less than two years for standard models. The capacity accommodates the static heat loads presented by the cryomodule anddistribution system, as well as the dynamic load imposed by cavity operation in order to maintain a stable temperature under all operating

conditions. A 400-W liquid nitrogen capacity is required for thermal intercepts and thermal shielding inside the cryomodule and distribution system. The liquid nitrogen will be supplied from the APS nitrogen distribution system, either directly or indirectly via a storage tank. Liquid nitrogen is chosen for cooling the shields for several reasons: it is readily available at the APS; ANL has mature designs using this approach; and the ODH issues from the 5.5 g/s flow rate do not appear to be severe. The preliminary design assumes that the cryoplant is located close to Zone-F, in the Early Assembly Area (EAA) space. Elements that inform the design of a cryogenic system for the SRF cavity include:

- System margin: Some amount of overcapacity will be designed into the system to mitigate the risks associated with uncertain cavity dynamic heat load and the possibility that the completed plant underperforms. The latter can also be mitigated with an incentive-based procurement contract tied to actual measured capacity during commissioning.
- Safety (pressure, cryogenics, oxygen deficiency hazard, system venting, etc.): Safety analyses are a fundamental aspect of cryoplant design. Vendors will be held to applicable codes and standards with regard to pressure system safety. Oxygen deficiency hazard analyses will be conducted for all cryoplant enclosures, as well as the regions of the APS tunnel containing cryomodules and distribution system components.
- System reliability: The cryoplant availability must meet overall APS requirements. This may be achieved via on-line spares, modular design, and system margin. A robust control system is an integral part of this aspect of performance.

2-3.12.6 Bunch-Lengthening RF System

A block diagram of the bunch-lengthening rf system is shown in Figure 2.67. The superconducting rf cavity is fitted with two output couplers utilizing 3 $\frac{1}{8}$-inch EIA coaxial flanges, each of which will be terminated with a dual coaxial directional coupler and a 50-kW broadband rf load to dissipate the rf power extracted from the beam. The directional couplers will be used to monitor the forward and reverse rf power at each load. The rf loads will be cooled with deionized water and will be monitored and protected by an interlock system to prevent over-dissipation, over-heating, or operation with insufficient water flow. Since the beam is the only source of power to the cavity, the primary mechanism for protecting the cavity will be to dump stored beam via the machine protection system (MPS).

The LLRF system will monitor and regulate the cavity field. Since the harmonic cavity is completely driven by the beam, the cavity field is determined by the beam current, the cavity detuning, and the loaded Q. As discussed in section 2-2.7, the loaded Q will be held fixed. Thus the cavity amplitude will be controlled via the cavity tuner.

An rf drive signal will be made available by the LLRF system to aid with initial system setup without beam. The drive signal can be switched into a directional coupler for one of the input couplers to excite the cavity. The resonant frequency can then be found and adjusted before the cavity sees beam. Initial balancing of the input couplers can also be determined during ring down after shutting the rf drive off. The rf drive can then be switched out of the system in preparation for beam.

The LLRF system will interface to EPICS, the interlock system, and the Timing/Event system

for time-stamping the data sent to the controls' fast data acquisition system (DAQ). A frequency generation unit will provide a phase reference signal as well as the local oscillator (LO) signal to translate the rf signals to an intermediate frequency for digital sampling. A channel will be reserved for a beam monitor which can be used to monitor the phase of the beam relative to the cavity field.

2-3.12.7 RF System and Related Documentation

The ICMS document numbers for engineering specifications, interface control documents, and final design review reports are shown in Figure 2.68.

References

[1] M. Pedrozzi et al. "First Operational Results of the 3rd Harmonic Superconducting Cavities in SLS and ELETTRA." In: *Proc. PAC 2003*. 2003, p. 878 (cit. on p. 106).

[2] E. Haebel et. al. "Cavity Shape Optimization for a Superconducting Linear Collider." In: *Proc. of High-eneergy Accelerator Conference, Hamburg, Germany*. 1992 (cit. on p. 106).

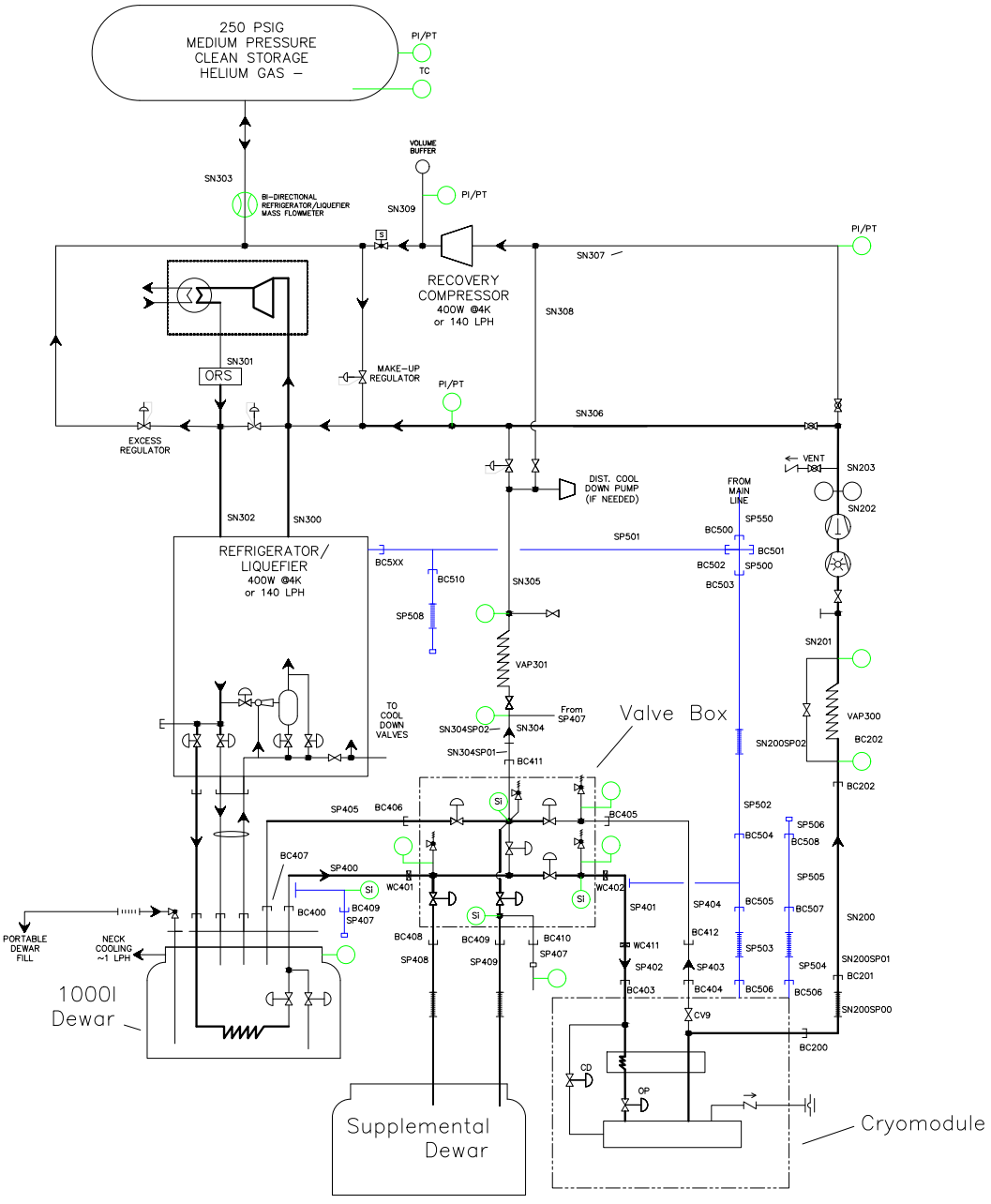

Figure 2.66. Schematic of the BLS cryogenic system.

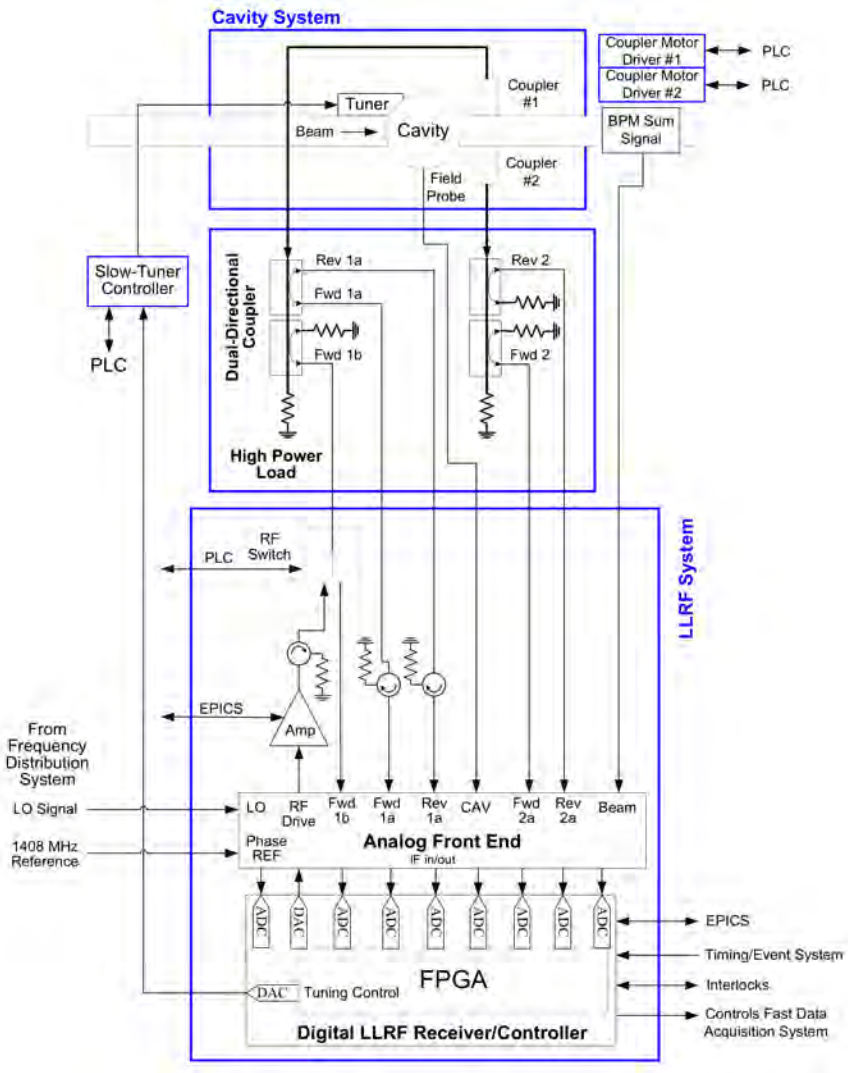

Figure 2.67. Block diagram for the bunch lengthening rf system.

Item Type	Engineering Specification Document (ESD)	Interface Control Document (ICD)	Final Design Review (FDR) and Review Report
352-MHz RF System Modifications	*apsu_2032668*	*apsu_2032669*	
Longitudinal Feedback System (LFS)	apsu_2031366	apsu_2012658	
Bunch Lengthening System (BLS)	apsu_1710774	apsu_1710775	apsu_1709598

Figure 2.68. RF, LFB, and BLS System Documentation.

2-3.13 Engineered Safety Systems

The "Advanced Photon Source Safety Assessment Document" [1] describes the engineered safety systems used by the present APS. These systems, with appropriate modifications, are expected to be sufficient for the upgraded APS facility described in this document. The storage ring accelerator safety envelope value of 9280 joules of stored-beam energy is not envisioned to need to change, nor will the safety envelope injected beam power of 308 W. The beam lifetime is expected to be significantly lower than the 10 hour value used for the present APS, which directly impacts ambient radiation levels seen outside of the accelerator enclosure.

The injector machines will operate with higher charge per pulse, but will remain within the existing 154 W operating envelope beam power. More frequent injection into the storage ring will be needed to compensate for reduced beam lifetime. Safety considerations regarding full bunch replacement swap-out operation are quite similar to those encountered when top-up operation was instituted at the APS. Permanent magnets will be added to the beamline front ends as an additional safety measure to assure that injected beams cannot be transported out to x-ray experimental hutches. This will be done in addition to present top-up safeguards, including top-up stored beam monitors that inhibit injection with x-ray shutters open unless a sufficient amount of stored beam is already circulating.

Extensive simulations have been conducted to quantify radiation levels associated with high injector charge, stored beam lifetime-related losses, bremsstrahlung, swap-out single-bunch loss, and total beam loss. Operation at lower beam energy (6 GeV vs. 7 GeV) is expected to offset, to some extent, the higher stored beam current (200 mA vs. 100 mA) and higher injected single-bunch charge ($\sim$16 nC vs. $\sim$2 nC).

A short summary of the APS Engineered Safety Systems is provided here, and the reader is referred to Ref. [1] for further details.

2-3.13.1 Access Control and Interlock System

The APS access control and interlock system (ACIS) is an engineered safety system for integrating access control and monitoring devices for the accelerator enclosures, including the linac, particle accumulator ring (PAR), booster synchrotron, linac extension area (LEA), and storage ring. The ACIS provides protection by ensuring that no one may occupy or enter an area where prompt radiation may be present. The system also inhibits beam generation when established radiation limits are exceeded, or when equipment failure is detected or improper access is gained. The plan is to use this system for the APS Upgrade.

The APS facility is designed to allow the major systems, i.e., linac/PAR, booster synchrotron, LEA, and storage ring, to run independently of one another under specific conditions. This is accomplished by the partitioning of areas with concrete shielding, beam stops, and other safeguards. Five complete and independent ACIS implementations are provided, one for the linac-PAR tunnel area, one for the synchrotron tunnel area, one for the LEA tunnel area, one for the rf area of the storage ring (zone F), and one for the remainder of the storage ring (zones A through E). Each system is designed using the applicable DOE orders and industrial safety standards. The APS/AES staff is responsible for the modification, verification, annual validation, and maintenance of the system. See Ref. [1]

for further details.

2-3.13.2 Personnel Safety System

The APS has the potential of operating with up to 70 beamlines. Each beamline includes multiple shielded enclosures containing optics and experimental equipment. Personnel access into these enclosures is controlled during beamline operation by the personnel safety system (PSS). The PSS is an engineered safety system for each beamline for controlling access into the enclosures. It ensures that access is allowed only under safe conditions (i.e., x-ray beam is off in the enclosure) and disables storage ring operation if improper access is gained or a PSS system fault is detected that could potentially endanger personnel.

The PSS for each beamline interfaces directly with the accelerator's ACIS for disabling storage ring operation. Each PSS is totally isolated from the PSS of any other beamline to prevent a fault from one beamline affecting the operation of other beamlines.

Each PSS is designed to meet the requirements of the beamline after review. Each system is designed using the applicable DOE orders and industrial safety standards. The APS staff is also responsible for the installation, verification, annual validation, and maintenance of the system. Although beamline designs require some flexibility in possible modes of operation, types of devices to be interlocked, and other operational requirements, the basic configuration and control aspects remain the same. The system documentation, test procedures, and training include all basic as well as specialized equipment and operating modes. The beamline efforts in the APS Upgrade will use these same systems and processes.

2-3.13.3 Machine Protection Systems

The machine protection system (MPS) protects the APS storage ring vacuum system from x-ray beam heating, loss of water cooling, and elevated vacuum levels. Many hundreds of sensors are monitored and networked through the MPS system. Insertion devices generate x-ray beams with power up to 21 kW and power density as high as 600 kW/mrad^2, posing a danger to downstream vacuum components if misdirected. Mis-steering is monitored with beam position monitors at the upstream and downstream ends of the insertion device (ID) straight sections, which are used as inputs to the MPS to trigger a fast beam abort. This is the beam position limit detector (BPLD) system, part of beam diagnostics scope. Flow rates for the vacuum system cooling water are monitored by the MPS for loss of flow, which trips the beam. Vacuum gate valves are closed in the event of a sigificant elevated vacuum event to isolate the leak from adjacent vacuum chambers. To prevent damage to a valve if closed on a hot x-ray beam, closure of an interlocked gate valve triggers a fast MPS beam abort. If a fast beam abort event trigger occurs, the beam is intentionally dumped by removing the low-level rf drive to the main rf systems. In the present APS, the beam then spirals inward and is lost in about 300 microseconds. This is expected to occur in less than 100 microseconds for APS-U. For the APS upgrade, fast beam dump events will be localized in a set of horizontal collimators located in Zone F of the storage ring. All fault conditions are latched and time stamped. The overall machine protection system is part of the control system scope.

The BPLD system will be generalized to allow interlocking on source angle vs. the present limit on individual BPM readbacks, for example. For the APS upgrade, the system will be configurable

to allow interlocking on any individual BPM readback, not just those near insertion device source points as is done presently. The BPLD system interlocking insertion device source points are enabled when insertion device gaps are closed below some level. In addition, there will be the capability to force the interlock to be activated independent of insertion device gap for testing and validation purposes; this is referred to as the bpld force-enable bit.

An injection/extraction pre-kicker will be used to inflate the transverse beam size of the bunch before it is dumped (Section 2-2.8.2). Because inflating the volume of the bunch before swapping out is essential to prevent damage to the swap-out dump, firing of the swap-out kickers will be gated on the waveform from the pre-kicker. In this way, if the pre-kicker does not fire, or does not fire with sufficient amplitude or correct timing, swap-out will not occur.

2-3.13.4 Radiation and Shielding Assessment

2-3.13.4.1 Introduction The primary purpose of the APS is to use electrons to produce high-quality synchrotron radiation for use in x-ray experiments. Personnel must be shielded against direct exposure to these x-rays. As the electron beam circulates in the storage ring, a small fraction of the beam is lost because of orbital excursions, interactions among beam particles, and collisions with gas molecules, which also produce radiation. Finally, as the storage ring is filled during injector operations, beam losses in collimators, beam stops, septum magnets, and other accelerator components lead to the production of prompt radiation fields. These radiation fields consist mainly of photons (bremsstrahlung x-rays and gamma rays) and neutrons. In addition to the prompt radiation exposure, interaction of these radiations leads to potential activation of accelerator components, which could create delayed radiation exposure hazards. The APS radiation safety policy protects workers, users, and the general public from hazards associated with these radiation fields. An extensive accelerator readiness review process is envisioned, which will take a comprehensive look at personnel safety, including all radiological aspects, and be completed prior to APS-U machine startup.

Table 2.45 summarizes some of the operating parameters for the present APS and the APS-Upgrade. The circulating current in the storage ring will be a factor of two higher in the Upgrade, at slightly lower electron energy, so that the energy stored in the storage ring will be nearly twice that at present. Two operating modes will be used, with the brightness mode being similar to present APS operations in terms of charge per bunch and beam lifetime in the storage ring. In the timing mode, however, the higher bunch charge means that the beam lifetime will be shorter, requiring more frequent injection and thus a higher average injected beam power.

Perhaps the most significant change is the use of swap-out injection, in which circulating bunches will be replaced after their charge falls to approximately 90% of the initial value. This mode of operation, combined with the increased electron loss rate from the storage ring and higher stored current, means that the Upgrade must inject about forty times more electrons into the storage ring than present operations at the APS, the majority of which ultimately end up at a dedicated, shielded swap-out beam dump.

These changes in operation may pose some challenges to the APS radiation safety program. A comprehensive analysis of radiation physics issues throughout the facility is underway to make sure the dose and dose rate goals stated below will be met. Because operation is similar in many ways to present APS operations, we do not anticipate any new radiation source terms. However, five areas

Table 2.45. Operating parameters for the present APS and the APS-Upgrade

Quantity	Present APS	APS-Upgrade Timing Mode	APS-Upgrade Brightness Mode
Electron energy (GeV)	7	6	6
Beam Current (mA)	100	200	200
Number of bunches	24	48	324
Charge per bunch (nC)	15.3	15.3	2.3
Beam lifetime (h)*	8	2.91	5.96
Injection mode	top-up	swap-out	swap-out
Stored energy (J)	2576	4420	4420
Average injection power (W)	0.089	4.0	1.95

* 10th percentile lifetime

have been identified for the APS-Upgrade that are undergoing detailed investigation to assess their potential for increases in radiation source terms and the need for supplemental shielding. These are (1) losses throughout the injector chain due to high-bunch-charge acceleration (2) increased losses of injected beam around the injection septum and other localized loss points due to the more-frequent injection (3) greater stored beam losses due to higher circulating current and shorter beam lifetime (4) increased gas bremsstrahlung production in the straight sections and directed down x-ray beamlines due to changes in pressure and composition of residual gas in the storage ring and (5) dose due to a dedicated beam dump that will receive the charge in the swapped-out beam bunches.

2-3.13.4.2 APS-U Limits for Annual Dose Limits for annual dose due to operation of the APS-Upgrade are based on applicable DOE and ANL regulations and experience at other US-based light sources. The primary document that governs radiation protection at DOE facilities is 10 CFR 835, Occupational Radiation Protection [2]. In addition, accelerator-specific standards are set forth in DOE Order 420.2c, Safety of Accelerator Facilities [3, 4]. Argonne's Radiological Safety Program Description [5] provides details on the local implementation of radiation protection standards. Finally, the APS has adopted its own dose guidelines. Table 2.46 shows the annual dose limits for APS-U, which are the same as for the present APS.

The maximum annual exposure to radiation workers is specified in 10 CFR 835.202 as 5000 mrem (50 mSv) effective dose.[2] The 10 CFR 835 design objective for external exposure is 1000 mrem (10 mSv) for new or modified facilities, in areas of continuous occupancy (2000 h/y) [see 10 CFR 835.1002(b)]. Argonne also has an Administrative Control Level of 1000 mrem/y (10 mSv/y) for individual occupational exposure, and a design objective for new or modified facilities of 500 mrem/y (5 mSv/y). The general shielding requirement for the APS is that the maximum individual (radiation) worker dose will be ALARA and less than 500 mrem/y (5 mSv/y). APS shielding policy also stipulates that the average rad worker dose will be below 200 mrem/y (2 mSv/y). Dosimeter readings acquired since commencement of APS operations have demonstrated that the actual average radiation worker dose for present APS operations is much less than 100 mrem/y (1 mSv/y).

[2]Note: 10 CFR 835 and Argonne's Radiological Safety Program Description use special units — Roentgen, rem, Curie, etc. — for designating radiological quantities, and that convention is followed here. SI units are indicated parenthetically.

The annual dose limit in 10 CFR 835 for non-radiation workers in a controlled area is 100 mrem (1 mSv), the same as for members of the general public. This category includes APS users. The Argonne and APS policies for on-site non-radiation workers in the vicinity of the APS facilities require that the average non-radiation worker dose be below 100 mrem/y (1 mSv/y). In addition, the dose at the site boundary from all pathways is required to be below 10 mrem/y (0.1 mSv/y). Present estimates of the annual doses for these two categories of exposure indicate that these requirements are being met.

Table 2.46. Proposed annual dose limits for the APS-Upgrade

Category	present APS	proposed for APS-U
Radiation workers	500 mrem	500 mrem
Non-radiation workers	100 mrem	100 mrem
General public (off-site)	10 mrem	10 mrem

Radiation monitors and accelerator diagnostics (e.g., for beam loss) will be used to limit the duration of off-normal and maximum credible incidents and thus limit the total dose delivered. Area radiation monitors will be installed in locations of expected beam loss in order to shut down the beam if high radiation levels are detected. Area radiation monitors have been in place around the storage ring since the early days of APS operations. These monitors shut down the beam in the event of excessive beam loss on insertion devices or other small apertures. Additional monitors are in place outside the bulk shielding of the PAR and the booster injection and extraction areas to detect high radiation levels that could lead to dose rates greater than 5 mrem in any one-hour period. Another protective measure is to monitor the beam loss in parts of the facility so that operators can take action in case the beam loss exceeds some set value (this can be done for reasons of both dose minimization to personnel and machine protection).

Since the upgrade will essentially be a new facility, dosimeters may initially be required for personnel working in some areas outside of the bulk shielding. Worker dose monitoring by dosimeters will still be required for unrestricted access to the accelerator system enclosures and for work with radioactive material. In addition, area dosimeters will continue to be used throughout the facility to integrate dose in selected areas. The results will be analyzed for higher-than-expected doses and trends of increased doses; in areas where such observations are made, shielding would be reevaluated and improved as appropriate.

The shielding requirements will be satisfied by using standard and high-density concrete for bulk shielding of the accelerator to ensure adequate attenuation of the photon and neutron components of the secondary radiation. This bulk shielding is already in place, and was designed for the present APS using conservative assumptions. In addition, steel, lead, dense polyethylene, and castable shielding materials will be used in the accelerator to supplement the bulk shielding at locations of high beam loss. Analysis to date indicates supplemental shielding will be needed only in the PAR enclosure, near the storage ring septum and swap-out beam dump locations, and near small horizontal apertures insertion device vacuum chambers in the storage ring. An example would be the SCAPE device proposed to be installed at beamline 4-ID after the ring commissioning.

Shielding of the experimental beamlines consists primarily of lead panels which are used to protect against the synchrotron radiation and bremsstrahlung produced in the storage ring and entering

the first-optics enclosures and experimental hutches. Beamline and experiment-station shielding was designed for the synchrotron radiation produced by either a bending magnet or an insertion device, and for bremsstrahlung radiation produced both by electron scattering from residual gas in the storage ring and by electron scattering from storage ring components. Typically one of the two sources dominates while the other is negligible, so that the shielding requirement is determined by the dominant source.

2-3.13.4.3 Tracking Simulations As input to the design and simulation of the radiation shielding, `elegant` tracking simulations are used to predict the loss distribution, i.e., the rate of particle loss around the circumference, for both injected and stored electron beams.

Studies of injected beam losses in section 2-2.8 indicate that losses should be low, with injection losses generally at or below 2% for nominal conditions. Injection losses have been found to occur predominantly at the small aperture insertion device chambers. For stored beam, losses occur because of lifetime-limiting phenomena such as Touschek and gas scattering, as described in section 2-2.9 These losses occur at the small aperture insertion device chambers, the injection septum, and collimator / beam dump apertures. Electrons hitting such features are lost, but not necessarily lost immediately. Instead, they are scattered and lost some distance away, which has been accounted for in the radiation physics analysis.

2-3.13.4.4 Radiation Physics Analysis New radiological consequence analyses calculate dose rates outside the shielding due to anticipated electron beam losses and ensure that the dose and dose rate goals are met. Calculations of radiation dose due to beam losses are performed with modern radiation transport computer codes such as MCNP [6]. A full set of normal and off-normal losses have been analyzed to determine the total dose due to all anticipated and potential losses around the facility.

Accelerator physics simulations are used to determine where electron losses can be expected to occur. For example, the vast majority of losses in the storage ring are expected to occur at collimators in sectors 37 through 01 and at the small-horizontal-aperture insertion devices (currently intended for the sector 04 SCAPE device, post project). Additional losses may occur at the other IDs and at the high-dispersion points in the storage ring, which will be in different locations for the new lattice than in the existing lattice. In general, the loss patterns for injected beam, stored beam, and dumped beam in the storage ring are different. Each of these have been modeled and the separate contributions are added together to determine the dose consequences of potential beam losses at any location. Dose due to losses in other parts of the facility (the injector chain) are also calculated to determine where supplemental shielding is needed. At this time the south wall of the PAR enclosure appears to be the only location in the injector chain requiring supplemental shielding.

Following installation of the APS-U storage ring and modification of other accelerator systems, there will be a period of accelerator systems commissioning. During this time, the beam current will be kept low to reduce losses around the facility. It may become necessary to exclude personnel from portions of the experiment hall floor during off-shift times to expedite the conditioning of the storage ring vacuum chambers. Confirmatory radiological surveys of specific loss points will be performed. If persistent excessive dose rates are found at any locations, these can be addressed by

changes to accelerator operations if possible or by the addition of local shielding.

2-3.13.4.5 Activated Materials Radiation interactions with accelerator and beamline components can potentially induce small amounts of radioactivity. When removed, the existing storage ring will include slightly activated components. Radiological surveys performed after accelerator systems are de-energized at the start of each scheduled maintenance period provide records of any above-background radiation fields and their locations. Prior to removal, every component in the storage ring enclosure will be surveyed by health physics personnel, who will identify and tag any radioactive components. Worker doses will be monitored via dosimeters as needed when activated components must be handled. All activated materials and equipment will be inventoried, segregated from non-activated components, and stored in designated and posted controlled radioactive material areas. Except for the various septum magnets in the injector system and a few known locations where electron beam scraping or losses have occurred, it is anticipated that most components will be essentially free of radioactivity. Material and components removed from the APS will be handled according to ANL-RS-TBD-003 [7], which is Argonne's implementation of the DOE standard DOE-STD-6004-2016 [8] for removal and disposal of activated components.

Since the operating parameters of the upgrade injector and storage ring will be much like those of the present APS, we expect that any activation induced in the Upgrade will be much like that in the present machine. The locations of some losses will change, for example due to the use of collimators to localize losses in the Upgrade. Due to the use of swap-out injection (as opposed to the top-up injection used in APS), significantly more electrons will be injected into the storage ring, but 90% of those will end up at a dedicated swap-out beam dump. Thus the total level of activation around the storage ring should be roughly similar to that in the present APS. The beam dump for swapped-out bunches will be well shielded and any activation products would be distributed throughout the volume of the material. The expected radionuclide inventories in the swap-out dump have been calculated as part of the design process. Beam losses may also be higher in the linac, PAR, and booster synchrotron than for the present APS since more charge will be accelerated through the injector system. Experience shows that most of the booster losses are at injection (at relatively low energy) which will reduce neutron production and hence material activation. Finally, there may be increased potential for activation of shielding materials, soil, groundwater, and air. Estimates of these quantities will also be made as part of the overall radiation physics analysis.

References

[1] *Advanced Photon Source Safety Assessment Document*. Tech. rep. APS-3.1.2.1.0 (cit. on p. 114).

[2] United States Nuclear Regulatory Commission. *Occupational Radiation Protection*. Jan. 2016. URL: https://energy.gov/ehss/occupational-radiation-protection-program-10-cfr-835 (cit. on p. 117).

[3] US Department of Energy. *Safety of Accelerator Facilities*. July 2011. URL: https://www.directives.doe.gov/directives-documents/400-series/0420.2-BOrder-c/ (cit. on p. 117).

[4] US Department of Energy. *Accelerator Facility Safety Implementation Guide for DOE O 420.4C, Safety of Accelerator Facilities*. Aug. 2014 (cit. on p. 117).

[5] D. Q. McCormick. *Argonne National Laboratory Radiological Safety Program Description*. Jan. 2017 (cit. on p. 117).

[6] D. Pelowitz et al. *MCNP6 User Manual, Version 1.0*. Tech. rep. LA-CP-13-00634. May 2013 (cit. on p. 119).

[7] H. Hall, Argonne National Laboratory, unpublished information, 2017 (cit. on p. 120).

[8] US Department of Energy. *Clearance and Release of Personal Property From Accelerator Facilities*. https://energy.gov/ehss/downloads/doe-std-6004-2016 (cit. on p. 120).

2-3.14 Injector Modifications

Swap-out injection places significant demands on the injector for the 48-bunch mode in particular. Table 2.47 gives the injector performance requirements. The calculation of the required charge

Table 2.47. Injector Performance Requirements

	Machine	Single bunch charge nC	ϵ_x nm-rad	Ratio ϵ_y/ϵ_x	Charge stability [a] rms
Required	Storage ring (inject)	16	–	–	1%
	Booster/BTS (extract)	17	60	16/60=0.27	5% [b]
	PAR (extract)	20			
Achieved	Booster	11	95 [b]	0.05−0.5	∼10%
	PAR	20			

[a] Total charge in storage ring.
[b] at 7 GeV. 60 nm when scaled to 6 GeV.

assumes that the Booster injection efficiency is 85% and the storage ring injection efficiency is 95% (see 2-2.8.3). The 16-nC storage ring bunch charge includes a deliberate 5% overfill. The target shot-to-shot injected bunch charge variation is 5%; if distributed uniformly over 48 bunches, this results in a 1% variation in the average stored charge in the storage ring [1]. In order to provide sufficient time for accumulating 20 nC in the PAR, the Booster repetition rate is lowered to 1 Hz. This modification has been implemented and is operational.

2-3.14.1 Injector Upgrades

The necessary upgrades to raise the injector intensity center about reducing the PAR bunch lengthening at high charge and upgrading the Booster rf system to cope with the increased beam loading to increase its acceptance at high charge. In addition, a new timing and synchronization system will allow ramping of the Booster rf frequency and thus its central energy to optimize acceptance at injection and emittance at extraction. The necessary Linac modifications to reach 450 MeV to 500 MeV will be carried out under the auspices of the ASD Operations department.

2-3.14.1.1 PAR Improvements The PAR 12. harmonic rf power amplifier will be upgraded with a solid-state 8 kW amplifier to allow rf voltage as high as 30 kV even at 20 nC stored intensity. Increasing the amplifier power requires upgrade of the circulator cooling, the rf loads and the power feed to the cavity and the input coupler. All these measures are being implemented well ahead of the dark period to be able to demonstrate the effectiveness of these measures and to aid further development of the Booster.

2-3.14.1.2 Booster Improvements The Booster rf frequency will no longer be identical to that of the storage ring. A new synchronization system has been designed described below. In addition, the Booster rf needs to cope with large beam-loading transients. This requires larger detuning than is possible at the present time. Together with the frequency ramp desired to optimize injection into Booster and storage ring this increaes the voltage at the cavity couplers beyond their present capability of 100 kW equivalent. A 300 kW coupler developed at CERN[2] can be adapted to the

Booster rf cavity. A 500 kW coupler design is being pursued with industry. Operating at 300 kW max. equivalent power, these couplers will allow a detuning of about 20 kHz. The coupling factor will be increased to $\beta = 3$ to better match the rf system to the increased beam loading. Extensive modeling indicates these measures together should give an injection efficiency of about 90% in the Booster at 20 nC.

2-3.14.1.3 Booster-Storage Ring Synchronization The APS-U storage ring will operate at somewhat higher rf frequency than the Booster. To facilitate bunch-to-bucket beam transfer a new timing and synchronization system has been designed and will be implemented, preserving some of the essential elements of the current system (e.g. the 60-Hz synchronization of the timing sequence). The system will allow ramping of the Booster rf frequency between injection and extraction, thus giving freedom in the choice of momentum offset and the extrated beam emittance.

Table 2.48. Specifications for Booster-storage-ring synchronization

Parameter	Machine	Value	Unit
Harmonic number	Booster	432	
	APS-U Ring	1296	
Rf frequency	Booster	351.9149761	MHz
	APS-U Ring	352.05598518	MHz
momentum compaction $(\alpha_c)^{(1)}$	Booster	0.0097	
Injection energy	Booster	325–500	MeV
	APS-U Ring	6000	MeV
Injection momentum offset	Booster	0 to –0.6	%
Extraction momentum offset	Booster	–0.6 to –2	%
Acceleration time (t_c)	Booster	variable to fit injection energy	
Frequency-ramp time (t_1)	Booster	variable to fit acceleration time	
Max. extraction timing jitter	Booster	50	ps

[1] On-momentum value.

The system, an earlier concept of which is described in [3] makes use of DDS technology to derive all frequencies from a common master clock. In this way overall coherence of the rf waveforms involved is maintained. A new, FPGA-based electronics module called Booster Timing Controller (BTC) will implement the central functions of the system: keeping track of the rf buckets of both Booster and storage-ring, calculating the parameters for the momentum ramp in the Booster (which can have an arbitrary waveform) as well as initiating the injection and extraction triggers needed for the rings, including the decoherence trigger for bunch-swap-out i the storage ring. The BTC will send the ramp table to the rf generator for the Booster and initiate the Booster rf program. The Booster magnet cycle remains unaffected by this.

The system will be implemented using μTCA packaging and boards commercially avaiable. In this way it integrates well with other systems planned for APS-U. High-level specifications are given in Table 2.48. The system will have the flexibility to support any combination of Booster injection and extraction momentum offset as well as injection energy.

Bunch-arrival diagnostics will be used to ensure the Booster bunch is injected centrally into the waiting storage-ring bucket. Technology similar to that used at the APS linac will be used, which detects the phase of the Booster bunch in the BTS at 2815 MHz and has demonstrated inherent jitter of about 1 ps. The BTC keeps track of the storage-ring bucket injected into, it is planned to

compare this to the actual bucket as determined by the bunch-current monitor of the storage-ring.

2-3.14.1.4 LLRF Improvements The increased demands on the injector rf systems require tighter control of the rf system and more flexible feedback and feed-forward systems. A state-of-the art LLRF architecture will provied the control and flexibility needed to implement these. The system will use FPGA technology and be implemented in μTCA to be compatible with the standard used at APS-U for other systems. The system will share similarities with the LLRF system for the bunch-lengthening system.

2-3.14.1.5 BTS Reconfiguration The BTS will be reconfigured to support the new bunch-swap-out injection into the storage ring. The geometry and focusing pattern in the section of the BTS in the storage-ring tunnel will change supporting the new match parameters and the new location of the injection. It is planned to measure at least some of the quadrupoles that will be temporarily removed from the tunnel to resolve differences between the optics model and the measured behaviour of the present BTS. One new dipole magnet has been designed magnetically. The optical axis of the new BTS will pass through three of the ring quadrupole magnets which have been designed to accomodate this. It then peels away far enough to clear the iron yoke of the 38B:BM1 dipole magnet and leave sufficient room for the new BTS:CB1 dipole magnet.

The optical design of the BTS is documented in Ref. [4]. The parameters for the BTS magnets are listed in Table 2.22 given in Sec. 2-2.8.

2-3.14.2 Injector Documentation

The ICMS document numbers for engineering specifications, interface control documents, and final design review reports are shown in Figure 2.69.

References

[1] M. Borland. “Simulations of swap-out for the APS MBA lattice.” private communication. Oct. 2013 (cit. on p. 122).

[2] Eric Montesinos. *Challenges in Rf Fundamental Power Coupler Technology*. Presentation at Workshop on Superconducting Technologies for Next Generation of Accelerators, CERN. Dec. 2012. (Visited on) (cit. on p. 122).

[3] U. Wienands, Argonne National Laboratory, unpublished information, 2017 (cit. on p. 123).

[4] A. Xiao, Argonne National Laboratory, unpublished information, 2018 (cit. on p. 124).

Item Type	Engineering Specification Document (ESD)	Interface Control Document (ICD)	Final Design Review (FDR) and Review Report
PAR 8kW Amplifier	apsu_2023829	apsu_2023828	apsu_2028615
Injector		*apsu_2012659*	apsu_2030047 Future
PAR LLRF System	*apsu_2032673*	*apsu_2032674*	
Booster LLRF System	*apsu_2032675*	*apsu_2032676*	
Booster High-Power Coupler			
Timing & Synch. Booster to Storage Ring	*apsu_2032670*	*apsu_2032671*	

Figure 2.69. Injector Upgrade Documentation Matrix.